ON LOCAL MECHANICAL PROPERTIES OF THIN PRESSURIZED SHELLS WITH COMBINED GEOMETRIC AND MATERIAL ANISOTROPIES

by

WENQIAN SUN

A DISSERTATION

Presented to the Department of Physics
and the Division of Graduate Studies of the University of Oregon
in partial fulfillment of the requirements
for the degree of
Doctor of Philosophy

September 2023

DISSERTATION APPROVAL PAGE

Student: Wenqian Sun

Title: On Local Mechanical Properties of Thin Pressurized Shells with Combined Geometric and Material Anisotropies

This dissertation has been accepted and approved in partial fulfillment of the requirements for the Doctor of Philosophy degree in the Department of Physics by:

Daniel Steck	Chairperson
Jayson Paulose	Advisor
Dietrich Belitz	Core Member
Peng Lu	Institutional Representative

and

Krista Chronister	Vice Provost for Graduate Studies

Original approval signatures are on file with the University of Oregon Division of Graduate Studies.

Degree awarded September 2023

DISSERTATION ABSTRACT

Wenqian Sun

Doctor of Philosophy

Department of Physics

September 2023

Title: On Local Mechanical Properties of Thin Pressurized Shells with Combined Geometric and Material Anisotropies

Thin elastic shells are ubiquitous in nature. Indentation measurements (i.e., poking) provide a useful way for probing mechanical properties of these shell structures. While spherical and cylindrical shells made of isotropic materials are well studied, many shells in nature have geometric anisotropy (e.g., ellipsoidal pollen grains) and/or material anisotropy (e.g., cells that have special growth directions), and mechanics of these shells are relatively less understood. I will present some new insights on indentation responses and buckling pressure of shells with geometric and material anisotropy using the shallow-shell theory. First, I will describe the indentation stiffness of pressurized ellipsoidal and cylindrical elastic shells that are made of isotropic materials. We are able to derive a closed form for the indentation stiffness of shells with arbitrary asphericity and internal pressure. Our results provide theoretical support for previous scaling and numerical results on the stiffness of ellipsoids and allow us to isolate the distinct contributions of geometry and

pressure-induced stresses on shell elasticity. I will then add the effects of material orthotropy, which assigns different elastic properties along orthogonal directions. For a commonly used model of orthotropy, we find a simple rescaling transformation that can effectively map a rectilinearly orthotropic shallow shell to an isotropic one with a different local geometry. With the rescaling transformation, we obtain new analytical insights for indentation responses and buckling of orthotropic shells. Our results provide a new perspective on how isotropic and orthotropic materials are related, isolate the effect of material orthotropy on shell elasticity, and can provide experimentalists with a means to analyze the internal pressure of biological structures that are made of orthotropic materials using atomic force microscopes.

This dissertation contains previously published as well as unpublished co-authored materials.

CURRICULUM VITAE

NAME OF AUTHOR: Wenqian Sun

GRADUATE AND UNDERGRADUATE SCHOOLS ATTENDED:

University of Oregon, Eugene, OR, USA
University of Minnesota Twin Cities, Minneapolis, MN, USA

DEGREES AWARDED:

Doctor of Philosophy, Physics, 2023, University of Oregon
Master of Science, Physics, 2022, University of Oregon
Bachelor of Science, Physics and Mathematics, 2018, University of Minnesota Twin Cities

AREAS OF SPECIAL INTEREST:

Mechanics and statistical physics of thin shells and plates
Elasticity and fluid mechanics
Applied differential geometry and topology
Non-equilibrium physics and stochastic differential equations
Mathematical physics

PROFESSIONAL EXPERIENCE:

Research Assistant, University of Oregon, 2019 – 2023

Graduate Teaching Assistant, University of Oregon, 2018 – 2022

GRANTS, AWARDS AND HONORS:

Lokey Doctoral Science Fellowship, University of Oregon, 2022 – 2023

PUBLICATIONS:

Sun, W., Paulose, J. Indentation responses of pressurized ellipsoidal and cylindrical elastic shells: Insights from shallow-shell theory. *Physical Review E* **104**, 025004 (2021)

ACKNOWLEDGEMENTS

"When we survey our lives and endeavors, we soon observe that almost the whole of our actions and desires is bound up with the existence of other human beings."

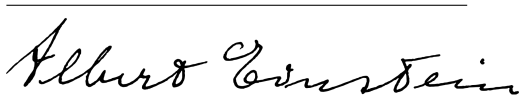

I am not good at expressing my gratitude. And I do not plan to express my gratitude here on paper, for I believe that *true* gratitude can never be expressed verbally. To my true friends and mentors, I want to sincerely say this: Wenqian will always keep in mind those good memories that we forged together and valuable lessons given to me. I do hope that our lives may cross again, so that I can treat you sincerely and honestly and also have some opportunities to repay your kindness. If not, I will try to keep improving myself to become a better person, being able to pass the kindness, warmth and wisdom that you have given to me to people who I will encounter in my future life.

To every reader of this dissertation.

I hope that it is helpful.

TABLE OF CONTENTS

LIST OF FIGURES

Figure Page

LIST OF TABLES

Table Page

CHAPTER I

INTRODUCTION

1.1 Shells and where to find them

Shell structures are ubiquitous in our daily life, e.g., baseball hats, spoons, tents and cars. Basically, any thin curved object can be categorized as a shell.[1] Mathematically, shells are two-dimensional curved surfaces with a finite thickness which is much smaller than the surface length scale.

Shells have many useful properties. When properly designed, even very thin shells can bear large loads [8]. This high efficiency of load-carrying behavior is one of the key factors why shells are widely used in aeronautical and marine engineering, such as aircraft, ships and submarines, where light weight is essential [8, 9]. In another aspect, because of their high strength and ability to enclose volume, shell structures are also commonly used in civil and architectural engineering; familiar examples are pressure vessels, water tanks and church domes [8, 9, 10].

One can also find shells in nature. As a macroscopic example, crustaceans have the instinctive wisdom of accumulating calcium carbonate over their lifetimes to build up and strengthen their shells, protecting themselves against their natural enemies. In the microscopic level, most of biological cells can be regarded as living shells; their shell structures isolate their cell contents and enable biochemical substance exchanges with the outside environment. It is known that mechanical properties of such microscopic shell structures play a crucial role in processes such as intracellular transport and cell division [3].

[1] I used the word "shell" here in a general sense which includes as a special case membranes (easily bendable shells [7]).

(a) Spoon. (b) Church dome. (c) Crab.

FIGURE 1.1. Some shells in daily life, engineering and nature.

1.2 Cells

In fact, cell mechanics by itself is a fascinating subject. In some sense, a cell wall is the most delicate shell structure in nature as its design involves both geometric and material anisotropies. As a first example, after being released from the anther of a flower, a pollen grain is able to fold onto itself to prevent dehydration; it has been shown that this ability is closely related to the ellipsoidal structure of the pollen grain [11]. As a second example, plant cell walls can be thought of as made of composite materials that in general are not isotropic [12]. A composite material consists of a base material in which high-strength filaments or fibers are embedded; as a consequence, the composite material is often stronger than the base material [10]. This material anisotropy helps a plant cell to withstand the large force generated by the turgor pressure (a high internal hydrostatic pressure due to cell contents) and contributes to the anisotropic expansion of a plant cell [13]. While the elasticity of thin isotropic spherical and cylindrical shells is well understood, there is less known about the mechanical properties of shells with geometric and material anisotropies. This thesis will advance our understanding of thin shells with anisotropies.

1.3 Indentation Response

Just as a curious child might poke an unfamiliar object to feel how soft it is, scientists often perform indentation tests to make quantitative measurements of an object's material properties [14]. For instance, biologists commonly use atomic force microscopes in indentation tests that aim to determine the material properties of some microscopic shell structures, like animal and plant cells [14]. The figure below depicts a bacteria cell indented by the tip of an atomic force microscope. Indentation measurements can also provide a means for scientists to probe and understand phenomena like mechanical failure and buckling.

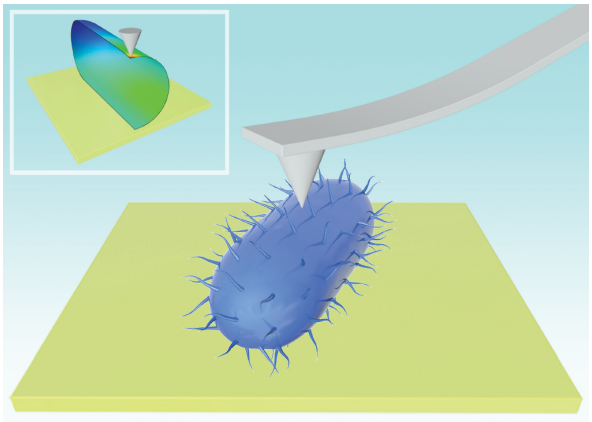

FIGURE 1.2. An atomic force microscope indenting a bacteria cell. The inset shows that a thin cylindrical shell can be a suitable model for the bacteria cell.
Image credit: Reference [1].

1.4 Previous Studies on Indentation Response

1.4.1 Spheres.

Around 1946, Reissner [15] first considered the problem for spherical shells when working on a project on the subject of load concentrations on shallow spherical domes. He derived analytical expressions for the indentation stiffness in the absence

of pressure by exactly solving the governing equilibrium equations. Two groups of researchers, Pogorelov [16] and Landau and Lifshitz [7], later separately came up with simple qualitative arguments for the same problem. Their approaches were able to give the correct dependence on shell radius and thickness and illuminated the origin of shells' geometric rigidity: Because of curvature, doubly-curved shells cannot stretch without bending.[2]

The indentation stiffness of pressurized spherical shells remains unknown until recent years. In the year of 2012, Vella and collaborators [14] first derived an analytical expression for the indentation stiffness of internally-pressurized spherical shells; the result was subsequently generalized to external pressures in Ref. [17].

1.4.2 Cylinders.

Cylinders has zero Gaussian curvature everywhere and are hence flat. Like thin flat sheets, they can bend without stretching. This leads to qualitatively different mechanical behavior which requires its own approach to study. Indentation stiffness of cylinders at zero pressure was first studied by Yuan [18] in 1946 and got revisited recently by de Pablo et al. in the study of microtubules [3]. The pressurized case in general has not been explored.

1.4.3 Ellipsoids.

Despite the fact that people have realized that the origin of shell's geometric rigidity is strongly related to the Gauss' Theorema Egregium and hence depends on the Gaussian curvature, the Gaussian-curvature-dependence has never been explicitly

[2]This is an implication of the Gauss' Theorema Egregium which in the simplest sense states that the Gaussian curvature of a surface depends on its metric.

derived. In 2012, Vella and collaborators [2] made an effort to study the indentation stiffness of spheroids, which are ellipsoids of revolution, using perturbation theory and scaling arguments combined with knowledge about spherical shells. However, because there is not an essential difference between a sphere's mean and Gaussian curvature, their conclusion on which geometric quantity dominates the indentation stiffness of a spheroid was not completely accurate.

Indentation stiffness of shells made of an orthotropic material so far has not drawn much attention, even though people have realized that biological structures, such as bacterial [19] and plant [13] cell wall, are made of an orthotropic material.

1.5 Thesis Outline

The rest of this thesis is structured as follows. In **Chapter II**, we study effects of geometry and pressure-induced stresses on indentation stiffness of ellipsoidal and cylindrical elastic shells that are made of an isotropic material. We show that the linear indentation response of these shells reduces to a single integral with two dimensionless parameters that encode asphericity and pressure. We are able to characterize contributions of geometry and pressure separately by analytically evaluating the integral in different limits and identifying the relevant length scale parameter. We find that at low pressures, the indentation stiffness is positively related to a shell's local Gaussian curvature, while in the high-pressure limit, the relevant scale is a geometric quantity that arises from the second stress invariant (i.e., determinant of the stress tensor). In **Chapter III**, we move one step further toward realistic cells by considering material orthotropy. We mainly study shell sections for which the material orthotropy directions match the principal curvature directions. We find a coordinate transformation, which is termed the rescaling

transformation, under which such an orthotropic shell section becomes effectively isotropic with a different local geometry. Applying the rescaling transformation on known isotropic results, we derive exact expressions for the buckling pressure as well as the linear indentation response of orthotropic cylinders and general ellipsoids of revolution, which we verify against numerical simulations. Our analysis disentangles the separate contributions of geometric and material anisotropies to shell rigidity. In particular, we identify the geometric mean of orthotropic elastic constants as the key quantifier of shell stiffness, playing a role akin to the Gaussian curvature which captures the geometric stiffness contribution. In the final chapter, **Chapter IV**, we briefly summarize our main results and suggest future research directions.

The content of **Chapter II** and **Chapter III** has been published in *Physical Review E* and posted on `arxiV`, respectively.

CHAPTER II

INDENTATION STIFFNESS OF ISOTROPIC SPHEROIDAL AND CYLINDRICAL SHELLS

This work was published in volume 104 of the journal *Physical Review E* in August 2021. I performed the analytical calculations and theoretical analysis and wrote the manuscript. My advisor, Jayson Paulose, supervised the research, performed theoretical analysis and wrote the manuscript.

2.1 Introduction

Thin curved shells are ubiquitous structures in nature and technology. Their curvature inextricably links bending and stretching deformations, making them stiffer than flat plates of the same thickness and material—a phenomenon termed geometric rigidity [20]. The ability of closed shells to maintain a pressure difference between their interior and the environment also impacts their load-bearing properties, as is apparent from our everyday experience with balloons. The interplay of elasticity, geometry, and pressure is crucial to our understanding of mechanical structures across a wide range of length scales, from viral capsids [21] to reactor pressure vessels [22].

Indentation—gauging the deformation of a structure in response to a localized force—is a simple yet powerful tool for evaluating the mechanical properties of myriad structures [23], including shells. Connecting shell indentation response to material properties and shape provides fundamental insight into geometric rigidity [2, 14, 24, 25], and is also of practical importance in evaluating the material properties of artificial [26, 27] and biological [4, 21, 28, 29] shell-like structures. Although the general relation between indentation force and deflection is nonlinear and depends

strongly on shell geometry, at small forces a linear regime can be identified in which the indentation force is proportional to the inward displacement. The constant of proportionality quantifies the *indentation stiffness* of the shell, a metric which can be compared across geometries and size scales. While theoretical analysis of the indentation stiffness of an unpressurized spherical shell dates back to the 1940s [15], few analytical results are available for other cases of interest. For cylinders, the indentation stiffness is known in the unpressurized case [3, 30], and in the high-pressure limit ignoring bending rigidity [4, 28]. An analytical expression for the indentation stiffness of internally-pressurized spherical shells was derived in Ref. [14], and was subsequently generalized to external pressures [17].

For ellipsoids, a major advance was achieved in back-to-back experimental [25] and theoretical [2] works reported in 2012. Reference [25] proposed a form for the indentation stiffness of pressurized ellipsoids by analogy with known results for spheres, which was tested against experiments. Reference [2] used a perturbative analysis to obtain analytical results for the stiffness of nearly-spherical ellipsoidal shells, and combined this analysis with simulation results and physical scaling arguments to propose analytical forms for general ellipsoidal shells in the unpressurized and high-pressure limits. However, the relative contributions of the two geometric invariants describing a curved surface—the mean and Gaussian curvatures—was not rigorously established in these results. In addition, the focus on the tractable zero- and high-pressure limits leaves a gap in our theoretical understanding of the indentation stiffness of ellipsoids and cylinders at intermediate internal pressures.

Here, we present a comprehensive theoretical analysis of the linear indentation stiffness of thin elastic ellipsoidal shells under both internal and external pressures.

Our main result is an expression for the indentation stiffness as an integral over a single variable, which includes the elastic moduli, curvature radii, and pressure as parameters. The integral provides closed analytical forms in several limits, which agree with known results. More generally, it can be numerically evaluated for arbitrary curvatures and pressures, providing a theoretical evaluation of the indentation stiffness in all regimes. Conceptually, we provide a unifying framework which encompasses the local geometric rigidity of ellipsoids of arbitrary curvature including the spherical and cylindrical limits (up to important corrections at zero pressure in the cylinder limit, which we describe). Besides providing analytical support to forms that were previously proposed using heuristic and scaling arguments [2, 25], we also find a new pressure scale which controls the response of thin shells under high internal pressure, and obtain new expressions for the indentation stiffness of pressurized cylinders.

Our approach uses shallow-shell theory, which expresses the stress and displacement fields of a shallow section of the shell using Cartesian coordinates in a plane tangent to the indenting point. Shallow-shell theory is widely used in elastic analyses of thin shells [9], and provides an accurate description when the characteristic length scale of the deflection is small compared to the curvature radii. As we will show, geometric rigidity ensures that point indentations induce such localized deflections at all pressures for non-cylindrical thin shells, and at non-zero internal pressures for cylindrical shells. For the zero-pressure limit of cylindrical shells, the contribution of long-wavelength deflections becomes important, and the shallow-shell theory breaks down; different techniques are needed to understand the indentation stiffness of unpressurized cylinders, as has been done in Ref. [3]. Nevertheless, we show that as internal pressure rises, shallow-shell theory becomes

valid again, and provides useful new results above a threshold pressure which we derive.

2.2 Shallow-Shell Equations and Indentation Stiffness

In this section, we will derive equations of equilibrium (EOEs) that characterize local deformations of a spheroidal shell using the shallow-shell theory. We follow the presentation by Koiter and van der Heijden [31]. Further analyses of the EOEs can be found in **Section 2.3**.

We start by mathematically describing a general *ellipsoidal* shell and characterizing a deformation imposed on it. We then address the special case of spheroids which are ellipsoids of revolution. The shells that we are interested in are thin: their thickness t is much less than the other shell dimensions, so that they can be effectively treated as two-dimensional surfaces. Besides encompassing a large class of artificial shells, thin-shell models have also been validated against experimental measurements for biological structures, such as bacterial cell walls [32, 33] and microtubules [30].

2.2.1 Description of Deformations of a Thin Shell

Let O be an arbitrary point on the equator of an ellipsoid where an external point load is exerted (see Fig. 2.1). We parametrize the ellipsoid using a right-handed Cartesian coordinate system whose xy-plane is the ellipsoid's tangent plane at O. The x-axis is chosen such that it coincides with the projection in the tangent plane of the curve which corresponds to one of the two principal curvatures at O. The y-axis will be accordingly in-line with the other principal curvature direction, and the z-axis points toward the center of the ellipsoid. Figure 2.1 illustrates such a

coordinate system. A local coordinate representation of the ellipsoid can be written as

$$Z(x,y) = c - c\sqrt{1 - \left(\frac{x}{a}\right)^2 - \left(\frac{y}{b}\right)^2}. \tag{2.1}$$

For a shallow region of the ellipsoidal surface close to the origin, such that $\left|\frac{\partial Z}{\partial x}(x,y)\right|, \left|\frac{\partial Z}{\partial y}(x,y)\right| \ll 1$, the expression above reduces to

$$Z(x,y) \approx \frac{x^2}{2R_x} + \frac{y^2}{2R_y}, \tag{2.2}$$

where $R_x \coloneqq \frac{a^2}{c}$ and $R_y \coloneqq \frac{b^2}{c}$ are the two principal radii of curvature at O. It should be noted that for the shallow-shell assumptions to hold, the approximated expression for Z is only valid in a sufficiently small neighborhood of O.

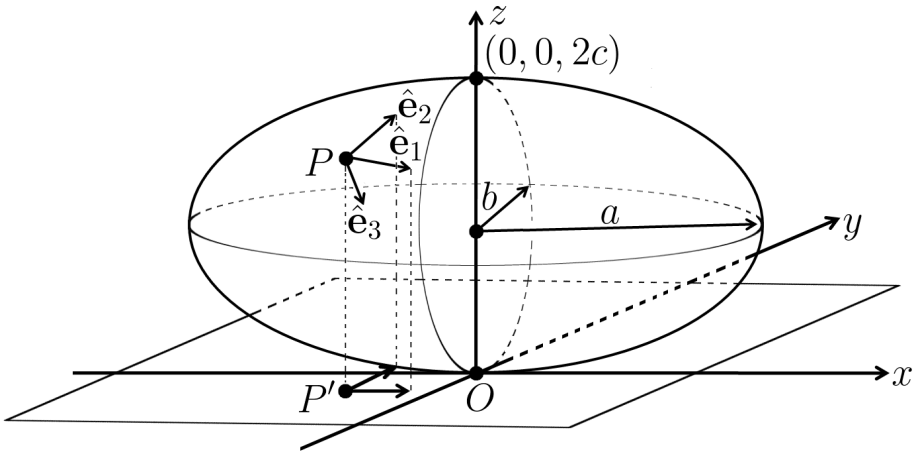

FIGURE 2.1. A local coordinate representation of an ellipsoid in the vicinity of O. The two local principal radii of curvature at O are $R_x = \frac{a^2}{c}$ and $R_y = \frac{b^2}{c}$. In the case of a spheroid (i.e., an ellipsoid of revolution), we let $b = c = R_y$ which is, under the circumstance, the radius of the circular cross-section at O. The illustration depicts a prolate spheroid for which $R_x > R_y$; an oblate spheroid would correspond to the case $R_x < R_y$. Deformation at an arbitrary point P is described by a displacement vector which is decomposed into a *non-orthonormal* basis $\{\hat{\mathbf{e}}_i\}_{i=1}^3$.

Points on the ellipsoid will get displaced under a deformation. The deformation can hence be described by a vector displacement field $\mathbf{u}(x,y)$ on the ellipsoid. Let

$P = (x_0, y_0, Z(x_0, y_0))$ be an arbitrary point. We decompose the displacement vector at P, $\mathbf{u}(x_0, y_0) \equiv \mathbf{u}_P$, as follows:

$$\mathbf{u}(x_0, y_0) = \sum_{i=1}^{3} u_i(x_0, y_0)\, \hat{\mathbf{e}}_i(x_0, y_0) \equiv u_i(x_0, y_0)\, \hat{\mathbf{e}}_i(x_0, y_0) \equiv u_{P,i}\, \hat{\mathbf{e}}_{P,i}, \tag{2.3}$$

where $\hat{\mathbf{e}}_{P,3}$ is the inward unit normal vector at P; $\hat{\mathbf{e}}_{P,1}$ and $\hat{\mathbf{e}}_{P,2}$ are unit vectors, which span the ellipsoid's tangent plane at P, chosen such that their projections in the plane Oxy coincide with $\hat{\mathbf{x}}$ and $\hat{\mathbf{y}}$, respectively (see Fig. 2.1). The Einstein summation convention was used. It should be pointed out that $\{\hat{\mathbf{e}}_{P,i}\}_{i=1}^{3}$ is generally not an orthonormal basis. The advantage of choosing such a basis is as follows. The prescribed deformation maps the point P to $\tilde{P} = \big(x_0 + \mathbf{u}_P \cdot \hat{\mathbf{x}}, y_0 + \mathbf{u}_P \cdot \hat{\mathbf{y}}, Z(x_0, y_0) + \mathbf{u}_P \cdot \hat{\mathbf{z}}\big) \equiv \big(x + \mathbf{u} \cdot \hat{\mathbf{x}}, y + \mathbf{u} \cdot \hat{\mathbf{y}}, Z + \mathbf{u} \cdot \hat{\mathbf{z}}\big)_P$, which can be further approximated as $\big(x + u_1 - u_3 \frac{\partial Z}{\partial x}, y + u_2 - u_3 \frac{\partial Z}{\partial y}, Z + u_3\big)_P$ under the assumptions that the region considered is shallow (or, equivalently, P is rather close to O), and $|u_1|, |u_2| \ll |u_3|$ for all points within the region.

Once the deformation is mathematically characterized, the strain tensor $u_{\alpha\beta}(x, y)$ ($\alpha, \beta \in \{1, 2\}$) can be obtained by computing the change of metric, as in Ref. [31]:

$$u_{\alpha\beta} = \frac{1}{2}\left(\partial_\alpha u_\beta + \partial_\beta u_\alpha - \frac{2u_3}{R_{\alpha\beta}} + \partial_\alpha u_3 \cdot \partial_\beta u_3\right), \tag{2.4}$$

where we have adopted the notations $\partial_1 \equiv \frac{\partial}{\partial x}$ and $\partial_2 \equiv \frac{\partial}{\partial y}$, and

$$\left(\frac{1}{R_{\alpha\beta}}\right) \coloneqq \operatorname{diag}\left\{\frac{1}{R_x}, \frac{1}{R_y}\right\}. \tag{2.5}$$

It should be pointed out that the form of the strain tensor assumes that the displacements are rapidly varying functions (on the scale of the shell's curvature

radii) in the two principal directions, which is another key assumption of the shallow-shell theory [9]. Mathematically, this means that $\left|\frac{1}{u_i}\partial_\alpha u_i\right| \gg \frac{1}{\min\{R_x,R_y\}}$; for example, for a wave-like deformation of the form $u_i = u_{i,0}e^{\mathbf{i}\mathbf{q}\cdot\mathbf{x}}$, this criterion becomes $\frac{2\pi}{\lambda_\alpha} =: q_\alpha \gg \frac{1}{\min\{R_x,R_y\}}$, i.e., the deformation wavelength λ_α is much smaller than the principal radii of curvature. As we will see in **Section 2.3.1**, this assumption is well justified in the study of thin curved shells for a wide range of geometric parameters.

For a two-dimensional isotropic elastic material, the stress tensor $\sigma_{\alpha\beta}(x,y)$ is related to the strain tensor through the strain-stress relation [7]

$$\sigma_{\alpha\beta} = \frac{Et}{1+\upsilon}\left(u_{\alpha\beta} + \frac{\upsilon}{1-2\upsilon}u_{\gamma\gamma}\,\delta_{\alpha\beta}\right), \tag{2.6}$$

where E and υ denote the material's Young's modulus and Poisson's ratio, respectively; $\delta_{\alpha\beta}$ is the Kronecker delta symbol, and, as aforementioned, t stands for the thickness of the material (recall that for thin shells, $t \ll \min\{R_x, R_y\}$). These two tensor fields incorporate all the information about the deformation and will be used below to write the elastic energy of the deformed ellipsoidal shell.

2.2.2 Elastic Energy of the Deformed Shell

It is known from differential geometry that a closed shell cannot bend without stretching. If we further consider the closed shell to be pressurized (i.e., the shell is subjected to a pressure p), then the total elastic energy associated with the deformation will have three components, namely, bending energy, stretching energy and pressure energy (i.e., the work done by the pressure on the shell).

The stretching energy can be generally written as

$$E_{\mathrm{s}}[u_{\alpha\beta}] = \frac{1}{2}\int_S \mathrm{d}A\, u_{\alpha\beta}\,\sigma_{\alpha\beta}. \tag{2.7}$$

The bending energy is related to changes in local curvatures and hence only depends on u_3 [9]:

$$E_{\mathrm{b}}[u_3] = \frac{1}{2}D\int_S \mathrm{d}A\,\left\{(\Delta\, u_3)^2 + 2(1-\upsilon)\left[(\partial_{12}u_3)^2 - \partial_{11}u_3\cdot\partial_{22}u_3\right]\right\}, \tag{2.8}$$

where $D = \frac{Et^3}{12(1-\upsilon^2)}$ is the bending stiffness, and $\Delta \equiv \partial_{11}+\partial_{22}$ is the two-dimensional Laplacian operator. The pressure energy is simply given by

$$W[u_3] = -\int_S \mathrm{d}A\, p\, u_3. \tag{2.9}$$

Our sign convention for pressure is that $p > 0$ ($p < 0$) corresponds to an internal (external) pressure. If there is an extra external point load with magnitude F acting at the point O, we can take into account the corresponding work done by simply replacing p with $p' \coloneqq p - F\delta^2(\mathbf{x})$ in the above expression.

The integration domain S is some region in the vicinity of O, outside of which the local deformation vanishes. Under the shallow-shell assumptions, the area element $\mathrm{d}A$ gets simplified: $\mathrm{d}A = \sqrt{1+\left(\frac{\partial Z}{\partial x}\right)^2+\left(\frac{\partial Z}{\partial y}\right)^2}\,\mathrm{d}x\,\mathrm{d}y \approx \mathrm{d}x\,\mathrm{d}y$. Adding up the bending, stretching and pressure energies, we obtain the total-energy functional

$$\begin{aligned} E_{\mathrm{tot}}[u_{\alpha\beta}, u_3] \approx \int_{S_\perp} \mathrm{d}x\,\mathrm{d}y\, \Bigg\{ &\frac{1}{2}u_{\alpha\beta}\,\sigma_{\alpha\beta} + \frac{1}{2}D\,(\Delta\, u_3)^2 + \\ &+ D(1-\upsilon)\left[(\partial_{12}u_3)^2 - \partial_{11}u_3\cdot\partial_{22}u_3\right] - p'\,u_3\Bigg\}, \end{aligned} \tag{2.10}$$

where $S_\perp$ is the projected region of S in the plane Oxy.

2.2.3 Equations of Equilibrium (EOEs)

According to the variational principle, minimizing the total-energy functional gives a system of EOEs

$$\begin{cases} D\,\Delta^2 u_3 + \Delta_{\mathrm{V}}\,\chi - [\chi, u_3] = p - F\delta^2(\mathbf{x}), \\ \\ \dfrac{1}{Y}\,\Delta^2\,\chi - \Delta_{\mathrm{V}}\,u_3 + \dfrac{1}{2}\,[u_3, u_3] = 0, \end{cases} \tag{2.11}$$

where the Vlasov operator in the shallow-shell coordinates is given by $\Delta_{\mathrm{V}} = \frac{1}{R_y}\partial_{11} + \frac{1}{R_x}\partial_{22}$; $\chi(x, y)$ is the Airy stress function that encodes stress information in the following way

$$\partial_{11}\chi = \sigma_{22}, \quad \partial_{22}\chi = \sigma_{11}, \quad \text{and} \quad \partial_{12}\chi = -\sigma_{12}; \tag{2.12}$$

$Y \coloneqq Et$, and $[\cdot, \cdot]$ denotes a second-order nonlinear operator known as the Monge-Ampère operator [20]: For any two smooth functions $f(x, y)$ and $g(x, y)$,

$$[f, g] \coloneqq \partial_{11} f \cdot \partial_{22} g + \partial_{22} f \cdot \partial_{11} g - 2\partial_{12} f \cdot \partial_{12} g. \tag{2.13}$$

The next step is to linearize the nonlinear EOEs around the relaxed state of the shell in response to the uniform pressure p. Like the total-energy functional, a general deformation of pressurized elastic shells is a combination of two deformation states: a membrane state and a bending state. The membrane state describes the in-plane stresses that arise when the shell expands or contracts in response to the uniform internal or external pressure with little change in local curvatures. The bending

state describes the indentation responses due to the external point load, which lead to localized transverse deformations with a significant bending energy component. To compute the linear indentation stiffness of the shell, we linearize the nonlinear EOEs around the membrane state and solve the resulting linearized equations for the bending state.

The membrane state of a general triaxial ellipsoid is unwieldy [34] and leads to distinct responses at all points on the ellipsoid. We therefore focus on the simpler case of spheroidal shells, which match most natural and artificial designs. A spheroid is an ellipsoid of revolution that has circular cross-sections along one of its principal axes. We take Ox to be that axis, and $b = c = R_y$ is thus the radius of the circular cross-section at O, which corresponds to the equator of the spheroid (see Fig. 2.1). The indentation stiffness that we will compute applies to all points on the equator, which are geometrically identical because of the axial symmetry.

The Airy stress function associated with the membrane state near a point on the spheroid's equator is known as [35]

$$\chi_0(x, y) = \frac{1}{4} p R_y \left[\left(2 - \frac{R_y}{R_x} \right) x^2 + y^2 \right]. \tag{2.14}$$

We can then write the following ansatz:

$$\begin{cases} u_3(x, y) = u_{3,0} + u_{3,1}(x, y), \\ \chi(x, y) = \chi_0(x, y) + \chi_1(x, y), \end{cases} \tag{2.15}$$

where the subscripts 0 and 1 denote the membrane state and the bending state, respectively. We took the normal displacement field in the membrane state (denoted by $u_{3,0}$) as a constant; this is an assumption commonly used in linear stability

analysis [9]. Substituting this ansatz into Eqs. (2.11) and discarding terms quadratic in $u_{3,1}$ and χ_1 that are assumed to be small, we finally obtain the linearized EOEs for spheroidal shells

$$\begin{cases} D\,\Delta^2\,u_{3,1} + \Delta_{\mathrm{V}}\,\chi_1 - \dfrac{1}{2}pR_y\,\Delta\,u_{3,1} - \dfrac{1}{2}pR_y\left(1 - \dfrac{R_y}{R_x}\right)\partial_{22}u_{3,1} = -F\delta^2(\mathbf{x}), \\ \dfrac{1}{Y}\,\Delta^2\,\chi_1 - \Delta_{\mathrm{V}}\,u_{3,1} = 0. \end{cases} \tag{2.16}$$

Although we have related the elastic moduli D and Y to microscopic constants of uniform materials, they may also be regarded as effective moduli that penalize changes in curvatures and metric of more complex quasi-two-dimensional structures, such as biological shells.

The physical quantity that we seek by solving this set of differential equations is the indentation stiffness. Recall that a point load with magnitude F is exerted at O, an arbitrary point on the spheroid's equator that serves as the origin in our parametrization, and $u_{3,1}(x, y)$ describes the transverse displacement due to the point load. The indentation stiffness is dictated by the Hooke's law:

$$k = -\frac{F}{u_{3,1}(\mathbf{x} = \mathbf{0})}. \tag{2.17}$$

This linear relationship between force and displacement is guaranteed when the shell deflection due to a point load is much less than shell thickness.

2.3 Results

2.3.1 The Stiffness Integral

We have derived the EOEs that characterize the local deformation at O due to the point load, Eqs. (2.16), which is a system of coupled linear partial differential equations (PDEs). Fourier transform can be applied to solve linear PDEs; the resulting solution always takes the form of an integral which often cannot be solved exactly [7]. However, in our case, the local nature of the indentation force (the point load) and measurement (localized transverse displacement) leads to a simplified Fourier integral. Recall again that the physical quantity that we are after is the local indentation stiffness which only requires the knowledge of the transverse displacement at the origin due to the point load, $u_{3,1}(\mathbf{x} = \mathbf{0})$. This local nature avoids the need to solve Eqs. (2.16) over the entire domain and enables analytical evaluation of the integral solution in our system.

Our convention for Fourier transform is the following: for any Fourier-transformable function of two variables $f(x, y) \equiv f(\mathbf{x})$,

$$f(\mathbf{x}) = \int \frac{\mathrm{d}^2 q}{(2\pi)^2}\, \hat{f}(\mathbf{q}) e^{\mathrm{i}\mathbf{q}\cdot\mathbf{x}}, \tag{2.18}$$

where

$$\hat{f}(\mathbf{q}) \equiv \mathscr{F}\{f(\mathbf{x})\}(\mathbf{q}) = \int \mathrm{d}^2 x\, f(\mathbf{x}) e^{-\mathrm{i}\mathbf{q}\cdot\mathbf{x}}. \tag{2.19}$$

Performing Fourier transform on Eqs. (2.16) and combining the resulting two algebraic equations gives

$$F = \mathscr{F}\{F\delta^2(\mathbf{x})\}(\mathbf{q}) = -\tilde{k}(\mathbf{q})\, \hat{u}_{3,1}(\mathbf{q}), \tag{2.20}$$

where

$$\tilde{k}(\mathbf{q}) \coloneqq Dq^4 + \frac{Y}{q^4}\left(\frac{q_x^2}{R_y} + \frac{q_y^2}{R_x}\right)^2 + \frac{1}{2}pR_y q^2 + \frac{1}{2}pR_y\left(1 - \frac{R_y}{R_x}\right)q_y^2. \tag{2.21}$$

The indentation stiffness can thus be written as

$$k = -\frac{F}{u_{3,1}(\mathbf{x} = \mathbf{0})} = \left[\int \frac{\mathrm{d}^2 q}{(2\pi)^2}\,\frac{1}{\tilde{k}(\mathbf{q})}\right]^{-1} =: I^{-1}. \tag{2.22}$$

Equations (2.21) and (2.22) underpin all our forthcoming results: the problem of computing the indentation stiffness has been reduced to evaluating a real-valued integral I, which we term the *stiffness integral*, over the two-dimensional wavevector space. However, we have yet to specify the integration limits in Eq. (2.22). As with any physical theory, the integration must strictly be carried out over some range of wavevectors $\mathbf{q}$ for which the Fourier-transformed stiffness [Eq. (2.21)] is valid. The large-wavevector (or UV) cutoff is dictated by the smallest wavelength for which the shallow-shell theory is valid, which is of the order of the shell thickness t. We will see that the integrand falls to zero for wavevectors whose magnitude is much smaller than $\frac{1}{t}$, so the upper limit of the stiffness integral can be safely taken to infinity (i.e., the theory is UV-convergent).

The treatment of the small-wavelength (or IR) cutoff requires more care. The strain-displacement relations used in the shallow-shell theory [Eq. (2.4)] are accurate only for displacements which vary over length scales that are small compared to the radii of curvature, i.e., Eq. (2.21) is strictly valid only for $|q_x| \gtrsim \frac{1}{R_x}$ and $|q_y| \gtrsim \frac{1}{R_y}$. Nonetheless, the physics of deflection of thin curved shells allows us to take the small-wavevector limit to $q \equiv \|\mathbf{q}\| = 0$ in the stiffness integral without sacrificing accuracy for a wide range of geometries, provided that the shells considered are thin.

To understand why this statement is true, let us consider the Fourier contributions to the stiffness integral in the absence of pressure. From Eq. (2.21), we find that $\frac{1}{\tilde{k}(\mathbf{q})}$ has a roughly even contribution over a region in Fourier space within the bounds $|q_x| \lesssim \frac{1}{\ell_{\mathrm{b},y}}$ and $|q_y| \lesssim \frac{1}{\ell_{\mathrm{b},x}}$, where $\ell_{\mathrm{b},x} \coloneqq \sqrt[4]{\frac{DR_x^2}{Y}}$ and $\ell_{\mathrm{b},y} \coloneqq \sqrt[4]{\frac{DR_y^2}{Y}}$ are two elastic length scales arising from the balance between bending and stretching. For thin shells, $\ell_{\mathrm{b},x} \sim \sqrt{R_x t}$ and $\ell_{\mathrm{b},y} \sim \sqrt{R_y t}$ scale with the geometric mean of the curvature radii and shell thickness; therefore, the two length scales are small compared to the curvature radii themselves yet still large compared to the shell thickness which serves as the UV-cutoff scale for the theory. This separation of length scales—a consequence of the interplay of geometry and elasticity—is responsible for the success of the shallow-shell theory in understanding indentation responses of thin shells, as has previously been recognized in the case of spherical shells [17, 36].

For a broad range of thin-shell spheroidal geometries satisfying $\sqrt{R_y t} \ll R_x \ll R_y^2/t$, the stiffness integral at zero pressure is dominated by modes with wavevectors in the range $1/R_x \lesssim |q_x| \lesssim 1/\ell_{\mathrm{b},y}$ and $1/R_y \lesssim |q_y| \lesssim 1/\ell_{\mathrm{b},x}$. As a result, including the erroneous but finite contributions to the integral for wavevectors near the origin ($|q_x| \lesssim 1/R_x$, $|q_y| \lesssim 1/R_y$) introduces an insignificant error to the indentation stiffness and the lower limit of integration can be taken to $q \to 0$ for these shells. However, the required separation of scales breaks down when $R_x \to 0$ (extremely narrow oblate shells) or $R_x \to \infty$ (cylinders) and the stiffness integral becomes invalid at zero pressure in these limits. At finite internal and external pressures, the convergence of the stiffness integral depends on additional physical considerations. We will address these considerations separately in the remainder of this subsection (where we impose the more stringent lower limit $R_x \geq R_y/2$ on the curvature along the x direction), as well as in **Section 2.3.4** (which discusses the behavior of the

stiffness integral under external pressure) and **Section 2.3.7** (which revisits the integral for internally-pressurized cylinders). In the latter subsection, we show that the indentation of cylindrical shells with a finite internal pressure is successfully captured by shallow-shell theory even though the criterion $R_x \ll R_y^2/t$ is violated. Through these investigations, we will identify ranges of pressure values for which the stiffness integral, Eq. (2.22) with lower and upper limits $q = 0$ and $q = \infty$ respectively, accurately captures the indentation stiffness for *all* spheroidal shell geometries with $R_x \geq R_y/2$ up to and including the cylinder limit of $R_x \to \infty$.

Next, we nondimensionalize the stiffness integral using appropriate physical scales. Of the two elastic length scales in the problem, we choose the scale $\ell_{\mathrm{b},y} = \sqrt[4]{\frac{D{R_y}^2}{Y}}$ associated with the equatorial radius to rescale lengths. For the pressure scale, we choose $p_{\mathrm{sc}} = \frac{4\sqrt{DY}}{{R_y}^2}$, the absolute value of the buckling pressure of a spherical shell with the same equatorial radius [37]. Also, observing that parts of $\tilde{k}$ depend on $q = \sqrt{{q_x}^2 + {q_y}^2}$, we rewrite the stiffness integral in polar coordinates. Accordingly, after some algebra, we obtain

$$I(\beta, \eta_{\mathrm{s},y}) = \frac{1}{8\pi^2}\frac{\ell_{\mathrm{b},y}^2}{\kappa}\int_0^{2\pi} \mathrm{d}\theta \times \\ \times \int_0^{+\infty} \frac{\mathrm{d}x}{\left[x + \eta_{\mathrm{s},y}\left(1 + \beta\sin^2\theta\right)\right]^2 + \left[\left(1 - \beta\sin^2\theta\right)^2 - \eta_{\mathrm{s},y}^2\left(1 + \beta\sin^2\theta\right)^2\right]}. \tag{2.23}$$

Thereinto, $\eta_{\mathrm{s},y} \coloneqq \frac{p}{p_{\mathrm{sc}}} = \frac{p{R_y}^2}{4\sqrt{DY}}$ is the scaled pressure, and our sign convention for the background pressure p carries over: a positive (negative) $\eta_{\mathrm{s},y}$ corresponds to an internal (external) pressure. The geometry of the spheroid is captured in the parameter $\beta \coloneqq 1 - R_y/R_x$ which characterizes the asphericity of a given spheroidal shell; specifically, spheroids with $\beta > 0$ are prolate whereas $\beta < 0$ corresponds

to oblate spheroids. (See Figure 2.1.) Moreover, for a prolate spheroid, $\sqrt{\beta} = \sqrt{1 - \frac{b^2}{a^2}} = \varepsilon$ is in fact the eccentricity of its elliptical cross sections.

A few geometries are of special interest. For spherical shells, $\beta = \varepsilon = 0$ ($R_x = R_y$), i.e., both cross sections at O are circular. At the other extreme, infinitely long, circular cylindrical shells have $\beta = \varepsilon = 1$ ($R_x \to \infty$), i.e., the elliptical cross section at O becomes an unbound rectangle with width R_y. The oblate spheroid $\beta = -1$ does not appear to have a special geometry, but is important for stability reasons due to the form of the membrane prestresses. When $\beta < -1$, $R_y < 2R_x$, and according to Eq. (2.14), the in-plane stress along y-direction in the membrane state, $\sigma^0_{22} = \partial_{11}\chi_0$ is *negative*, i.e., compressive, for *internally* pressurized shells. As a result, oblate shells with $\beta \leq -1$ may even buckle under an internal pressure [38]. Correspondingly, the positivity of the Fourier-transformed stiffness, Eq. (2.21), cannot be guaranteed at all wavevectors even for positive pressures, and the corresponding analysis of the stiffness integral will be hence somewhat different. In the rest of the paper, we will restrict our focus to shells with $-1 < \beta \leq 1$.

The indentation stiffness due to some general load function (that specifies the spatial distribution of external forces), instead of a point load, can be calculated as the spatial convolution of k and the load function since k can be thought of as a Green's function. Such a convolution integral might be carried out numerically, as long as the load function is itself confined to the shallow region of interest.

2.3.2 Zero-Pressure Stiffness

As a direct check, we can first calculate the indentation stiffness at zero pressure with the stiffness integral. Setting $\eta_{s,y} = 0$ reduces Eq. (2.23) to

$$I(\beta, \eta_{s,y} = 0) = \frac{1}{8\pi^2} \frac{\ell_{b,y}^2}{\kappa} \int_0^{2\pi} \mathrm{d}\theta \int_0^{+\infty} \frac{\mathrm{d}x}{x^2 + \left(1 - \beta \sin^2 \theta\right)^2}$$
$$= \frac{1}{8} \frac{\ell_{b,y}^2}{\kappa} \frac{1}{\sqrt{1-\beta}} = \frac{1}{8} \sqrt{\frac{R_x R_y}{DY}}.$$

Taking the inverse then gives the zero-pressure stiffness

$$k_{p=0} = 8\sqrt{DY}\sqrt{K}. \tag{2.24}$$

This agrees with the conjecture in Ref. [2], analytically showing that the zero-pressure stiffness is indeed governed by a shell's local Gaussian curvature $K \coloneqq \frac{1}{R_x R_y} = \frac{1-\beta}{{R_y}^2}$.

Equation (2.24) holds for almost all spheroidal shells, except close to the limit of infinitely long, circular cylindrical shells ($\beta \to 1$). For instance, unpressurized cylinders have a finite linear indentation stiffness [3] whereas our shallow-shell result predicts zero stiffness. The reason is that for such shells with low Gaussian curvature, the indentation responses at zero pressure are dominated by long-wavelength components much larger than the curvature radius R_y, and the shallow-shell approximations thus break down. Nevertheless, as we will see in **Section 2.3.7.1**, shallow-shell theory becomes valid as the internal pressure rises because of the appearance of a new deformation length scale, so our approach remains useful up to $\beta = 1$ for internally pressurized shells.

The fact that the zero-pressure stiffness of a double-curved shell depends on its local Gaussian curvature, in hindsight, is quite sensible; in fact, we might

have guessed this dependence in the first place, without explicitly carrying out the integration. The reason is as follows. The physics should not depend on the choice of coordinates. In light of this, the zero-pressure stiffness can only depend on those quantities, constructed from the curvature tensor, that are invariant under rotation. For a two-dimensional surface, there are two such candidates, namely: the Gaussian curvature and the mean curvature. From Eq. (2.21), we can infer that the stiffness simply cannot depend on the mean curvature: setting either R_x or R_y to infinity, the stiffness would vanish, while the mean curvature remains finite; in other words, it is, ironically, the inevitable failure of shallow-shell theory, when being applied to long cylindrical shells, that actually guarantees the Gaussian-curvature dependence.

2.3.3 Numerical Evaluation of the Stiffness Integral

Having preliminarily verified the validity of the stiffness integral, we evaluate the indentation stiffness for four shell geometries in the range of interest $-1 < \beta \leq 1$ via numerical evaluation of the stiffness integral, Eq. (2.23). Results are shown in Figure 2.2. As expected from Eq. (2.24), we observe that close to zero pressure, shells with lower values of β are stiffer since their local Gaussian curvature is higher at the indentation point. However, at higher pressures, the trend is reversed, and oblate shells become softer than prolate shells at the same pressure. At negative (i.e., external) pressures, the indentation response softens, and the stiffness vanishes at a critical pressure value which falls with increasing asphericity for $\beta > 0$, but is constant at $\eta_{s,y} = -1$ for $\beta < 0$ (inset to Figure 2.2). Below the critical pressure (i.e., at pressures more negative than the critical pressure), the indentation stiffness remains nil since the stiffness integral no longer converges. In fact, the indentation stiffness below the critical pressure, the concept itself becomes physically unmeaning

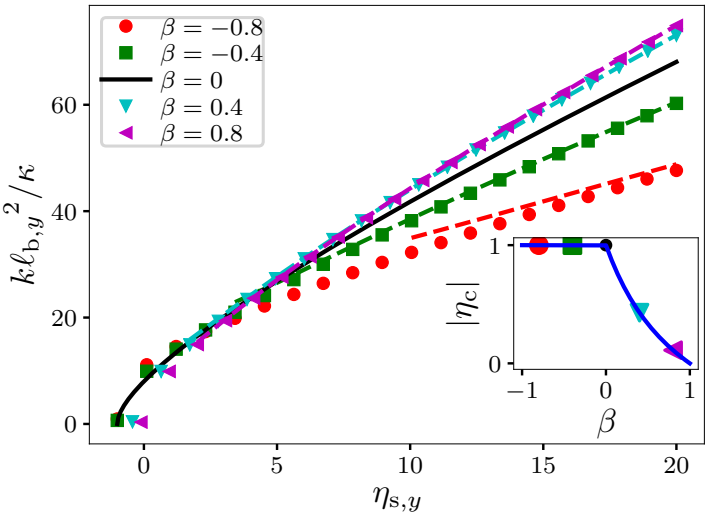

FIGURE 2.2. Indentation stiffness of five different shell geometries subject to both internal and external pressures. Symbols denote data obtained from numerically evaluating the stiffness integral [Eq. (2.23)], and the dashed curves represent values associated with the analytical expression for the asymptotic indentation stiffness [Eq. (2.30)]. Solid line shows the known analytical stiffness for spherical shells, Eq. (2.28). Inset shows the magnitude of external pressures at which the indentation stiffness vanishes for each shell (symbols), compared to the prediction from the local instability criterion, Eq. (2.25, a) (solid line).

because the shell is already buckled. In the remainder of this section, we reveal the physical mechanisms underlying these features through an analysis of the stiffness integral. We also take a detailed look at the behavior of the indentation stiffness at pressures close to the critical value, and at high pressures. We wrap up the section by studying the stiffness of pressurized cylinders ($\beta = 1$).

2.3.4 Loss of Stiffness and Buckling Instability

From Figure 2.2, we notice that for all the chosen asphericities, there exists a critical external (i.e., negative) pressure at which the indentation stiffness vanishes. This softening indicates a divergence of the stiffness integral, which occurs when $\tilde{k} \to 0$ for some value(s) of the wavevector $\mathbf{q}$ [Eq. (2.21)] heralding the existence of

an unstable mode at that wavevector. The instability in the shell shape due to the divergent mode is a local manifestation of the buckling instability exhibited by curved shells under a uniform external pressure [7]. In practice, a minuscule indentation force applied when the shell is close to the buckling instability would generate a large, sudden inversion in the shell near the indentation point. The description of this post-buckled shape with large deflections goes beyond the reach of shallow-shell theory, involving sudden, often catastrophic changes in the enclosed shell volume; however, the approach to the buckling threshold itself can be captured using linear stability analysis. The relation between indentation response and buckling has been employed experimentally as a non-destructive means to determine the buckling threshold of thin shells [39, 40, 41].

The *local* critical pressure at the equator of the spheroid is the threshold η_{c} at which the stiffness integral first becomes unbounded, i.e.,

$$\lim_{\eta_{\mathrm{s},y}\to\eta_{\mathrm{c}}^{+}} I(\beta,\eta_{\mathrm{s},y}) = +\infty.$$

This threshold is obtained by finding the global minima of $\tilde{k}(\mathbf{q})$ in wavevector space and identifying the pressure at which they hit zero, which gives:

$$\eta_{\mathrm{c}} = \begin{cases} -\dfrac{1-\beta}{1+\beta}, & \text{for } 0 \le \beta < 1, \\ \\ -1, & \text{for } -1 < \beta < 0, \end{cases} \qquad (2.25,\ \text{a})$$

or

$$p_{\mathrm{c}} \coloneqq \eta_{\mathrm{c}}\, p_{\mathrm{sc}} = \begin{cases} -\dfrac{4\sqrt{DY}}{2R_xR_y - {R_y}^2}, & \text{for } 0 \leq \beta < 1, \\ -\dfrac{4\sqrt{DY}}{{R_y}^2}, & \text{for } -1 < \beta < 0, \end{cases} \tag{2.25, b}$$

in real units. More compactly, we can write p_{c}, in terms of the equatorial Gaussian curvature K and the asphericity β, as

$$p_{\mathrm{c}} = -\frac{4\sqrt{DY}K}{1+|\beta|}, \tag{2.25, c}$$

for all $|\beta| < 1$.

We used the word "local" to emphasize the fact that the critical pressure we have identified only characterizes the loss of stability at the equator of the spheroidal shell. Other regions of the shell have different local curvatures, and might experience loss of stability at different values of the external pressure. The *global* buckling pressure of the spheroidal shell corresponds to the smallest magnitude of external pressure at which a local instability arises somewhere on the shell. Noting that regions of highest Gaussian curvature are locally the stiffest, and from symmetry considerations, we expect Eq. (2.25, c) to be the global buckling pressure for prolate shells ($\beta > 0$) for which the Gaussian curvature is lowest for points along the equator. For oblate shells, by contrast, the Gaussian curvature is lowest at the two poles ($(\pm a, c, c)$ in Figure 2.1), where the local geometry is spherical with radius $R_{\mathrm{p}} = \frac{b^2}{a} = \frac{1-\beta}{\sqrt{K}}$, and the corresponding buckling pressure is

$$p_{\mathrm{c,p}} = -\frac{4\sqrt{DY}}{R_{\mathrm{p}}^2} = -\frac{4\sqrt{DY}K}{(1-\beta)^2}. \tag{2.25, d}$$

As expected, $|p_{\mathrm{c,p}}| < |p_{\mathrm{c}}|$ for oblate shells with $\beta < 0$. The expressions (2.25, c) for $0 \leq \beta < 1$ and (2.25, d) for $-1 < \beta < 0$ reproduce known results for the global buckling pressures of ellipsoidal shells [42].

Moving forward, we only consider pressures above the local buckling pressure at the indentation point (i.e. $p > p_{\mathrm{c}}$) when evaluating the indentation stiffness. Note that for oblate shells, this range includes external pressures for which the poles of the spheroid are past their buckling threshold. However, our local-stiffness results are still useful for shells which match the elasticity and geometry of Figure 2.1 locally in the vicinity of the equator but deviate from it further away (e.g., an oblate spheroid reinforced at the poles to prevent buckling). When $\eta_{\mathrm{s},y} > \eta_{\mathrm{c}}$, the integrand in Eq. (2.23) is guaranteed to be positive definite, and the integration over the radial coordinate can be carried out to leave behind a single integral

$$I(\beta, \eta_{\mathrm{s},y}) = \frac{1}{8\pi^2} \frac{\ell_{\mathrm{b},y}^2}{\kappa} \int_0^{2\pi} \mathrm{d}\theta \, \frac{\mathrm{i}\frac{\pi}{2} + \tanh^{-1}\left[\frac{\eta_{\mathrm{s},y}\left(1+\beta\sin^2\theta\right)}{\sqrt{\eta_{\mathrm{s},y}^2\left(1+\beta\sin^2\theta\right)^2 - \left(1-\beta\sin^2\theta\right)^2}}\right]}{\sqrt{\eta_{\mathrm{s},y}^2\left(1+\beta\sin^2\theta\right)^2 - \left(1-\beta\sin^2\theta\right)^2}}. \tag{2.26}$$

2.3.5 Analytical Results for Spherical Shells

In this section, we will recover and review some results for the indentation stiffness of spherical shells in the literature.

Setting $\beta = 0$ (or, equivalently, $R_x = R_y$) in Eqs. (2.25), we first recover the critical pressure of spherical shells [37],

$$p_{\mathrm{c,\,sph}} \coloneqq p_{\mathrm{c}}(R_x = R_y) = -\frac{4\sqrt{DY}}{{R_y}^2}, \tag{2.27, a}$$

or, in the scaled units,

$$\eta_{\mathrm{c,\ sph}} \coloneqq \eta_{\mathrm{c}}(\beta = 0) = -1. \tag{2.27, b}$$

(Recall that in our convention, $\eta_{\mathrm{s},y} < 0$ corresponds to an external pressure.)

The stiffness integral [Eq. (2.26)] also gets greatly simplified because the angular dependence vanishes when $\beta = 0$:

$$I(\beta = 0, \eta_{\mathrm{s},y}) = \frac{1}{4\pi} \frac{\ell_{\mathrm{b},y}^2}{\kappa} \frac{\mathrm{i}\frac{\pi}{2} + \tanh^{-1}\left(\frac{\eta_{\mathrm{s},y}}{\sqrt{\eta_{\mathrm{s},y}^2 - 1}}\right)}{\sqrt{\eta_{\mathrm{s},y}^2 - 1}}.$$

Taking the inverse and rewriting the resulting expression in terms of real physical quantities, we obtain the established result of the indentation stiffness of pressurized spherical shells [14, 17],

$$k_{\mathrm{sph}}(p) = \frac{8\sqrt{DY}}{R_y} \begin{cases} \dfrac{\sqrt{1 - \eta_{\mathrm{s},y}^2}}{1 - \frac{2}{\pi} \arcsin \eta_{\mathrm{s},y}}, & \text{for } |\eta_{\mathrm{s},y}| < 1, \\ \pi \dfrac{\sqrt{\eta_{\mathrm{s},y}^2 - 1}}{\ln\left(\frac{\eta_{\mathrm{s},y} + \sqrt{\eta_{\mathrm{s},y}^2 - 1}}{\eta_{\mathrm{s},y} - \sqrt{\eta_{\mathrm{s},y}^2 - 1}}\right)}, & \text{for } \eta_{\mathrm{s},y} \geq 1. \end{cases} \tag{2.28}$$

In practice, two limits of the indentation stiffness are of particular interest: the asymptotic behavior in the large-pressure limit $\eta_{\mathrm{s},y} \gg 1$ and the critical behavior as the buckling pressure is approached (the limit $\eta_{\mathrm{s},y} \to \eta_{\mathrm{c,\ sph}}^{+}$). For the large-pressure limit, it can be shown that

$$k_{\mathrm{sph}} \sim \frac{4\pi\sqrt{DY}}{R_y} \frac{\eta_{\mathrm{s},y}}{\ln 2\eta_{\mathrm{s},y}}. \tag{2.29}$$

By expanding k_{sph} around $p_{\mathrm{c,\ sph}}$, one can demonstrate that the indentation stiffness of spherical shells near the critical pressure scales as $\sqrt{\frac{p_{\mathrm{c,\ sph}} - p}{p_{\mathrm{c,\ sph}}}} = \sqrt{1 - \frac{\eta_{\mathrm{s},y}}{\eta_{\mathrm{c}}}}$.

In the next section, after briefly explaining why the two limits are interesting, we will derive similar expressions for spheroidal shells.

2.3.6 Analytical Expressions for Indentation Stiffness of Spheroidal Shells at Low and High Pressures

While the stiffness integral can be numerically integrated to obtain the indentation stiffness at any pressure and geometry within our prescribed limits, the analytical behavior of the stiffness at large pressures ($\eta_{s,y} \gg 1$) and close to the buckling instability ($\eta_{s,y} \to \eta_c^+$) is of special interest. The large-pressure regime is relevant to the mechanics of biological cells, which are often investigated with indentation assays [4, 21, 28, 29], using shell elasticity as a minimal model of the expected response. The crowded internal environment of living cells leads to very high turgor pressures; some typical values that have been reported are 30 kPa for the bacterium *Escherichia coli* (which corresponds to $\eta_{s,y} \approx 15$) [4], 2 MPa ($\eta_{s,y} \sim 10^3$) for *Bacillus subtilis* [43] and 2 MPa ($\eta_{s,y} \approx 10$) for *Saccharomyces cerevisiae* yeast cells [29]. Analytical expressions for the asymptotic behavior of the indentation stiffness at large rescaled pressures will be useful to infer elastic properties, which themselves are sensitive to biological processes, by performing indentation measurements. Secondly, shell buckling can be interpreted as a first-order phase transition with pressure as the order parameter [44], which ought to leave a signature in the indentation response. Studying the limit $\eta_{s,y} \to \eta_c^+$ will provide us with insights regarding the essence of the non-analyticity of the indentation stiffness near the critical pressure.

2.3.6.1 The Large-Pressure Regime. We are interested in finding a parameter in the modified stiffness integral, Eq. (2.26), which becomes small at large pressures to enable an exact evaluation of the leading stiffness behavior. From the form of the integrand, the appropriate parameter is identified as

$$y(\beta, \eta_{\mathrm{s},y}, \theta) \coloneqq \frac{1}{\eta_{\mathrm{s},y}} \frac{1-\beta\sin^2\theta}{1+\beta\sin^2\theta}.$$

In the range of interest of the asphericity, $-1 < \beta \leq 1$, the parameter y is small for all $0 \leq \theta < 2\pi$ provided the pressure satisfies

$$\eta_{\mathrm{s},y} = \frac{p{R_y}^2}{4\sqrt{DY}} \gg \begin{cases} 1, & \text{for } 0 \leq \beta \leq 1, \\ \dfrac{1-\beta}{1+\beta}, & \text{for } -1 < \beta < 0. \end{cases} \tag{$*$}$$

We use the small parameter to rewrite and analytically evaluate the modified stiffness integral [Eq. (2.26)] in the large-pressure limit:

$$\begin{aligned} I &= \frac{1}{8\pi^2}\frac{\ell_{\mathrm{b},y}^2}{\kappa}\int_0^{2\pi}\frac{\mathrm{d}\theta}{\eta_{\mathrm{s},y}\left(1+\beta\sin^2\theta\right)}\frac{i\frac{\pi}{2}+\tanh^{-1}\left(\frac{1}{\sqrt{1-y^2}}\right)}{\sqrt{1-y^2}} \\ &\overset{y\ll 1}{\approx} \frac{1}{8\pi^2}\frac{\ell_{\mathrm{b},y}^2}{\kappa}\frac{1}{\eta_{\mathrm{s},y}}\left[\ln 2\eta_{\mathrm{s},y}\int_0^{2\pi}\frac{\mathrm{d}\theta}{1+\beta\sin^2\theta}+\int_0^{2\pi}\frac{\mathrm{d}\theta}{1+\beta\sin^2\theta}\ln\left(\frac{1+\beta\sin^2\theta}{1-\beta\sin^2\theta}\right)\right] \\ &\approx \frac{1}{4\pi}\frac{\ell_{\mathrm{b},y}^2}{\kappa}\frac{1}{\eta_{\mathrm{s},y}}\frac{1}{\sqrt{1+\beta}}\left[\ln 4\eta_{\mathrm{s},y}+\ln\left(1+\frac{1}{\beta}\right)-2\tanh^{-1}\left(\sqrt{\frac{1-\beta}{1+\beta}}\right)\right]. \end{aligned} \tag{2.30}$$

The inverse of Eq. (2.30) provides an analytical expression for the indentation stiffness of spheroidal shells at large pressures. We note that in our choice of length

and pressure units, Eq. (2.30) holds for both prolate and oblate spheroidal shells, but the criterion for "large pressure" differs in these two cases, as defined in Eq. (∗).

To simplify and shed light on the final expression, we introduce a novel radius parameter $\mathcal{R} \coloneqq R_y\sqrt{1+\beta}$ with which we can rewrite Eq. (2.30) as

$$I = \frac{1}{4\pi}\frac{\mathcal{R}}{\sqrt{\kappa Y}}\frac{1}{\eta_{\mathcal{R}}}\left[\ln 4\eta_{\mathcal{R}} - \ln\left(1+\sqrt{1-\beta^2}\right)\right] \tag{2.31, a}$$

$$= \frac{1}{4\pi}\frac{\mathcal{R}}{\sqrt{\kappa Y}}\frac{1}{\eta_{\mathcal{R}}}\left[\ln 4\eta_{\mathcal{R}} - \ln\left(1+\mathcal{R}\sqrt{K}\right)\right], \tag{2.31, b}$$

where $\eta_{\mathcal{R}} \coloneqq \frac{p\mathcal{R}^2}{4\sqrt{DY}} = \eta_{s,y}(1+\beta)$ is the corresponding scaled pressure, and K again denotes the local Gaussian curvature of the given shell. Besides its mathematical convenience, $\mathcal{R}$ can be related to the second stress invariant, i.e., the determinant of the prestress tensor $\sigma^0_{\alpha\beta}$, as follows:

$$\mathcal{R} = R_y\sqrt{1+\beta} = R_y\sqrt{2-\frac{R_y}{R_x}} = \frac{2}{p}\sqrt{\sigma^0_{11}\sigma^0_{22}}, \tag{2.32}$$

where $\sigma^0_{11} = \partial_{22}\chi_0$, and $\sigma^0_{22} = \partial_{11}\chi_0$ are the prestresses along the principal directions in the membrane state. Equation (2.32) shows that $\mathcal{R}$ is the radius of curvature for which the internal pressure p would balance a membrane tension of magnitude equal to the square root of the second stress invariant according to Laplace's law [45]. We term the associated curvature, $\mathcal{R}^{-1}$, the *distensile curvature*. Just as the local Gaussian curvature dictates the zero-pressure indentation stiffness of curved shells [Eq. (2.24)], the distensile curvature dominates the indentation response at large internal pressures although a residual dependence on the Gaussian curvature remains in the stiffness integral [Eq. (2.31, b)].

From Eq. (2.31, a) we can see that under the rescaling (with the novel radius parameter), spherical shells are the stiffest in the large-pressure regime since when $\beta = 0$, the geometric contribution, $\ln\left(1+\sqrt{1-\beta^2}\right)$, reaches its maximum $\ln 2$ and hence minimizes the stiffness integral. (This feature is depicted in the bottom inset of Figure 2.3.) At still higher pressures such that the geometric contribution becomes negligible, Eq. (2.31, a) reduces to

$$I \overset{\eta_{\mathcal{R}}\gg 1}{\approx} \frac{1}{4\pi}\frac{\mathcal{R}}{\sqrt{\kappa Y}}\frac{\ln 4\eta_{\mathcal{R}}}{\eta_{\mathcal{R}}}. \tag{2.33}$$

In practice, the expression

$$I \overset{\eta_{\mathcal{R}}\gg 1}{\approx} \frac{1}{4\pi}\frac{\mathcal{R}}{\sqrt{\kappa Y}}\frac{\ln 2\eta_{\mathcal{R}}}{\eta_{\mathcal{R}}} \tag{2.34}$$

is more accurate for most shell geometries, since $\ln\left(1+\sqrt{1-\beta^2}\right)$ is closer to $\ln 2$ than to zero for $|\beta| < 0.91$. By comparison to Eq. (2.29), we see that the corresponding stiffness is identical to the high-pressure response of a spherical shell with radius $\mathcal{R}$ and rescaled pressure $\eta_{\mathcal{R}}$.

Equations (2.31) and (2.34) provide a concise interpretation of the indentation stiffness of spheroidal shells at large pressures. When the material parameters D and Y are fixed, the stiffness in the large-pressure limit depends on three quantities: the pressure p, the determinant of the stress tensor at the point of indentation, and the local Gaussian curvature K. The first two quantities define a curvature radius $\mathcal{R}$ and a dimensionless pressure $\eta_{\mathcal{R}}$ which both originate from the membrane prestress; Eq. (2.31, b) explicitly separates the prestress and geometry contributions to the indentation stiffness. The large-pressure indentation of the shell approaches that of a sphere with the prestress-derived curvature and pressure scales [Eq. (2.34)]

when the weak dependence on K is ignored. Upon using these new scales, a duality connecting prolate to oblate shells at high pressures is revealed: Equation (2.31, a) is invariant under the replacement $\beta \to -\beta$, so a shell with geometric parameters $\{R_y = \rho,\ \beta = \beta_0\}$ and internal pressure p has the same high-pressure response as a shell with parameters $\left\{R_y = \rho\sqrt{(1+\beta_0)/(1-\beta_0)},\ \beta = -\beta_0\right\}$ and the same pressure, for which the parameters $\mathcal{R}$ and $\eta_{\mathcal{R}}$ are identical. The criterion for high pressure, Eq. $(*)$, also reduces to the symmetric form

$$\eta_{\mathcal{R}} \gg 1 + |\beta| \sim 1,$$

which holds for both prolate and oblate shells.

Comparison with established results. In previous works [2, 25], it was hypothesized that the high-pressure indentation response of ellipsoidal shells is dictated by the mean curvature radius $R_{\text{M}} = 2/(R_x^{-1} + R_y^{-1})$ and a dimensionless pressure scale τ set by the mean membrane prestress at the indentation point, $\sigma_{\text{M}} = (\sigma_{11}^0 + \sigma_{22}^0)/2$, via

$$\tau = \frac{\sigma_{\text{M}} R_{\text{M}}}{2\sqrt{DY}}.$$

Our asymptotic form for the inverse of the indentation stiffness, Eq. (2.34), parallels the high-pressure indentation stiffness proposed in Ref. [2] which used R_{M} and τ in place of $\mathcal{R}$ and $\eta_{\mathcal{R}}$ respectively. However, the origins of our radius and pressure scales are somewhat different as they utilize the determinant, rather than the trace, of the membrane stress [Eq. (2.32)].

Despite these differences, our proposed length and pressure scales are as successful as the previously-hypothesized scales in quantifying the high-pressure indentation

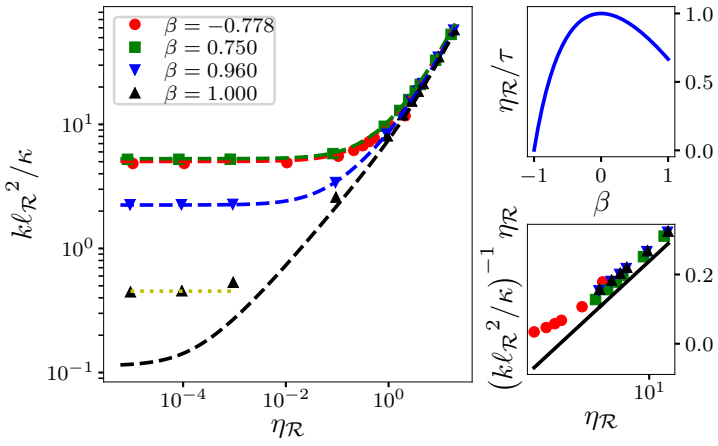

FIGURE 2.3. Comparison of predicted indentation stiffness (dashed lines) to finite-element simulation data from Ref. [2] (symbols). Data are scaled using the length scale $\ell_{\mathcal{R}} = \sqrt[4]{\frac{D\mathcal{R}^2}{Y}}$ and pressure scale $\frac{4\sqrt{DY}}{\mathcal{R}^2}$, for which we predict convergence of the stiffness curves at large rescaled pressures $\eta_{\mathcal{R}} = \frac{p\mathcal{R}^2}{4\sqrt{DY}}$. A similar convergence was depicted in FIG. 3 of Ref. [2] using different scales. Yellow solid line corresponds to the zero-pressure stiffness of long cylindrical shells, calculated with formulae in Ref. [3], since shallow-shell theory does not apply to cylinders below a threshold pressure (see **Section 2.3.7**). The top inset compares the rescaled pressure $\eta_{\mathcal{R}}$ to the alternative variable τ introduced in Ref. [2]. (See text for details.) The bottom inset is a linear-log plot which shows how the product of the inverse scaled stiffness and the scaled pressure varies as the pressure increases; thereinto, the black solid line shows the result for spherical shells.

response. In Figure 2.3, we compare our predictions for the indentation stiffness (curves) to the results of finite-element simulations (symbols) reported in FIG. 3 of Ref. [2]. Upon using the new length and pressure scales, the data for $\eta_{\mathcal{R}} \gg 1$ collapse onto the proposed asymptotic form, Eq. (2.34) (solid line). We also compare our numerically-evaluated indentation stiffness, Eq. (2.26) (dashed curves), to the finite-element data, and find quantitative agreement for almost all geometries and pressures. The disagreement between the stiffness integral and the measured indentation stiffness at low pressures for cylindrical shells ($\beta = 1$) is expected; see **Section 2.3.7** for an explanation and a more accurate prediction (dotted line). Our

prediction also deviates from the finite-element simulation results for the highest simulated pressure of the oblate spheroidal geometry $\beta = -0.778$; we hypothesize that second-order shape changes in response to the internal pressure might be responsible for this discrepancy. Apart from these data points, our theoretical predictions lie within 5% of the finite-element measurements, which validates our approach over a wide range of geometries and pressures. The duality connecting prolate to oblate shells upon using the scales $\mathcal{R}$ and $\eta_{\mathcal{R}}$ is also visible in Figure 2.3, since the data for $\beta = 0.75$ and $\beta = -0.778$ nearly overlap.

We were unable to neatly separate the contributions from the mean and the Gaussian curvatures in our evaluation of the high-pressure stiffness integral. Therefore, we cannot directly evaluate the relative merits of using our proposed scales $\mathcal{R}$ and $\eta_{\mathcal{R}}$ over the previously-proposed scales R_{M} and τ from Ref. [2]. However, some insight as to why both scales perform well in explaining the high-pressure indentation stiffness can be obtained by comparing them as a function of geometry. By expressing R_{M} and τ in terms of R_y and β, we find the ratio

$$\frac{\eta_{\mathcal{R}}}{\tau} = \frac{(1+\beta)(2-\beta)}{2+\beta}.$$

As the inset of Figure 2.3 illustrates, the ratio is of order one for most values of the asphericity. Similarly, the ratio $\mathcal{R}/R_{\text{M}}$ evaluates to a number of order one for $|\beta| < 1$. Therefore, using the two sets of physical scales is expected to provide similar results. The discrepancy between the two approaches becomes significant only for oblate shells with β approaching -1. In this limit, an advantage of the scales introduced here is that the instability expected for large internal pressures at $\beta = -1$ (see **Section 2.3.4**) is reflected in the pressure-induced curvature taking on imaginary values when σ_{22}^0 becomes negative in Eq. (2.32). By contrast, the mean

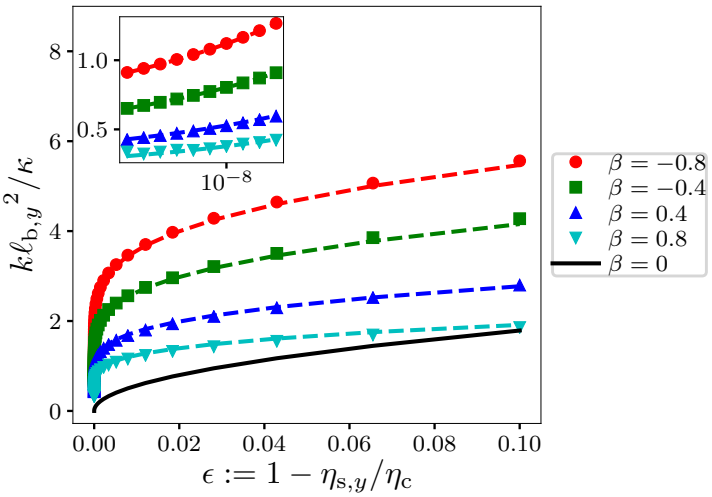

FIGURE 2.4. Critical behavior of the indentation stiffness as η_c is approached, for five spheroidal geometries. Symbols denote data obtained from numerical integration of the stiffness integral. Solid and dashed lines correspond to analytical expressions Eqs. (2.28) and (2.35), respectively. Inset shows the same data on linear-log scales to reveal the slow approach to zero stiffness as $\eta_{s,y} \to \eta_c^+$ for non-spherical shells.

curvature and mean prestress both remain positive and vary smoothly as β falls below -1, and the approximations using the mean scales incorrectly predict a finite indentation response at large pressures.

2.3.6.2 The Critical Behavior upon Approaching the Buckling Pressure.

We now analyze the functional approach of the indentation stiffness to zero as the critical pressure is approached from above ($\eta_{s,y} \to \eta_c^+$). (Recall that in our convention, external pressures correspond to $\eta_{s,y} < 0$, and the critical pressure η_c for the local instability is negative.) Defining the fractional distance from the critical pressure as

$$\epsilon := \frac{\eta_c - \eta_{s,y}}{\eta_c} = \begin{cases} 1 + \dfrac{1+\beta}{1-\beta}\eta_{s,y}, & \text{for } 0 \le \beta < 1, \\ 1 + \eta_{s,y}, & \text{for } -1 < \beta < 0, \end{cases}$$

we would like to study the limit $\epsilon \to 0^+$ of the stiffness integral. As before, we first rewrite the stiffness integral [Eq. (2.26)] in a simplified form

$$I = \frac{1}{2\pi^2}\frac{\ell_{\mathrm{b},y}^2}{\kappa}\int_0^{\frac{\pi}{2}} \mathrm{d}\theta \times \begin{cases} \dfrac{1}{1-\beta\cos^2\theta}\dfrac{\frac{\pi}{2}+\arcsin y}{\sqrt{1-y^2}}, & \text{for } 0 \le \beta < 1, \\ \dfrac{1}{1-\beta\sin^2\theta}\dfrac{\frac{\pi}{2}+\arcsin y'}{\sqrt{1-y'^2}}, & \text{for } -1 < \beta < 0, \end{cases}$$

where

$$y(\beta,\epsilon,\theta) \coloneqq \frac{1+\beta\cos^2\theta}{1+\beta}\frac{1-\beta}{1-\beta\cos^2\theta}(1-\epsilon),$$

and

$$y'(\beta,\epsilon,\theta) \coloneqq \frac{1+\beta\sin^2\theta}{1-\beta\sin^2\theta}(1-\epsilon).$$

Notice that the limits

$$\lim_{\substack{\epsilon\to 0^+\\ \theta\to 0^+}} y = 1 \quad \text{and} \quad \lim_{\substack{\epsilon\to 0^+\\ \theta\to 0^+}} y' = 1$$

give rise to divergence of the integrals. In other words, in the limit $\epsilon \to 0^+$, the definite integrals are dominated by their values in the vicinity of $\theta = 0$. Accordingly, we can approximate them by replacing the integrands with the corresponding second-order Taylor polynomials around $(\epsilon, \theta) = (0, 0)$:

$$I \approx \frac{1}{2\sqrt{2}\pi}\frac{\ell_{\mathrm{b},y}^2}{\kappa}\int_0^{\frac{\pi}{2}} \mathrm{d}\theta \times \begin{cases} \dfrac{1}{1-\beta(1-\theta^2)}\dfrac{1}{\sqrt{\epsilon+\frac{2\beta\theta^2}{1-\beta^2}}}, & \text{for } 0 \le \beta < 1, \\ \dfrac{1}{(1-\beta\theta^2)\sqrt{\epsilon-2\beta\theta^2}}, & \text{for } -1 < \beta < 0. \end{cases}$$

These integrals can be analytically evaluated:

$$\begin{aligned} I &\approx \frac{1}{4\pi}\frac{\ell_{\mathrm{b},y}^2}{\kappa}\frac{1}{\sqrt{|\beta\eta_{\mathrm{c}}|}}\sinh^{-1}\left(\sqrt{\frac{2}{\frac{4}{\pi^2}\frac{1}{|\beta|}+1+f(\beta)}}\frac{1}{\sqrt{\epsilon}}\right) \\ &\approx \frac{1}{4\pi}\frac{\ell_{\mathrm{b},y}^2}{\kappa}\frac{1}{\sqrt{|\beta\eta_{\mathrm{c}}|}}\ln\left(\sqrt{\frac{8}{\frac{4}{\pi^2}\frac{1}{|\beta|}+1+f(\beta)}}\frac{1}{\sqrt{\epsilon}}\right), \end{aligned} \tag{2.35}$$

where

$$f(\beta) \coloneqq \begin{cases} \left(1-\dfrac{4}{\pi^2}\right)\beta, & \text{for } 0 \le \beta < 1, \\ \\ 0, & \text{for } -1 < \beta < 0. \end{cases}$$

Figure 2.4 shows that the analytical result, Eq. (2.35) (dashed lines) successfully reproduces the results due to numerical integration of the stiffness integral (symbols) close to the critical pressure for four different shells.

Eq. (2.35), the main result in this section, implies that for general spheroidal shells, their indentation stiffness falls off as the inverse of the logarithm of the distance ϵ from the critical point, i.e., $k \propto -\frac{1}{\ln\sqrt{\epsilon}}$. This slow approach of the stiffness to zero, due to the logarithmic divergence of the stiffness integral for non-spherical shells, is evident in the inset to Figure 2.4. By contrast, the approach to zero is more drastic for spherical shells: upon taking the limit $|\beta| \to 0$ of Eq. (2.35), one obtains

$$\lim_{|\beta|\to 0}\frac{1}{\sqrt{|\beta\eta_{\mathrm{c}}|}}\sinh^{-1}\left(\sqrt{\frac{2}{\frac{4}{\pi^2}\frac{1}{|\beta|}+1}}\frac{1}{\sqrt{\epsilon}}\right) = \frac{\pi}{\sqrt{2\epsilon}},$$

which implies that near the critical pressure, the indentation stiffness of spherical shells $k_{\mathrm{sph}} \propto \sqrt{\epsilon}$, as was expected from the exact results reported in **Section 2.3.5**. Spherical shells are much softer at all pressures near the critical pressure compared to spheroidal shells, since $k_{\mathrm{sph}}/k \propto \sqrt{\epsilon}\ln\sqrt{\epsilon} \overset{\epsilon\to 0}{\to} 0$. The contrasting characters of

the softening as the critical pressure is approached reflects the fact that spherical shells harbor a massive degeneracy of divergent Fourier components of the stiffness integral as $\eta_{\mathrm{s},y} \to \eta_{\mathrm{c}}^{+}$ (a circle with radius $q = 1/\ell_{\mathrm{b},y}$ in the wavevector plane), whereas non-spherical shells exhibit divergent Fourier modes only at the two values, $\mathbf{q}_{\pm}^{\mathrm{pro}} = \left(0, \pm\sqrt{1-\beta}/\ell_{\mathrm{b},y}\right)$ and $\mathbf{q}_{\pm}^{\mathrm{ob}} = (\pm 1/\ell_{\mathrm{b},y}, 0)$ for prolate and oblate shells, respectively.

The results in this subsection do not apply to cylindrical shells because the limit $\beta \to 1^{-}$ fails to exist ($\lim_{\beta\to 1^{-}} \eta_{\mathrm{c}} = 0$). A different approach will be used to study cylindrical shells below.

2.3.7 Indentation Responses of Cylindrical Shells

The case of extremely long prolate ellipsoids, for which $R_x \to \infty$ or $\beta \to 1$, requires special treatment. As we argued in **Section 2.2.1**, shallow-shell theory accurately describes the strains associated with transverse deflections only if the deflections vary over length scales that are small compared to the local radii of curvature R_x and R_y. When $R_x \to \infty$, the characteristic wavelength of deflections along the y direction, which is controlled by $\ell_{\mathrm{b},x}$, eventually becomes larger than the cylinder circumference $2\pi R_y$. Shallow-shell theory builds the response to point indentation and to external pressure out of modes that do not change the metric or curvature of the shell, erroneously predicting zero indentation stiffness for unpressurized cylinders (**Section 2.3.2**) as well as buckling at an infinitesimal external pressure ($\eta_{\mathrm{c}} \to 0$, **Section 2.3.4**).

The true deformation mode responsible both for the indentation stiffness and the finite buckling pressure of an infinitely long cylindrical shell is the isometric change in shape of the circular cross section to an ellipse, which is also responsible for the buckling of inextensible rings [9]. This mode extends over the entire

shell circumference and cannot be captured by shallow-shell theory. Unlike the characteristic deflections of doubly-curved shell segments which involve both stretching and bending, the elliptical mode costs no stretching energy as it does not change the circumference; it only involves bending energy because of the change in curvature away from the initial circular shape. When the bending energy of the elliptical shape change is evaluated using basis functions that extend over the entire circumference, the mechanics of the cylindrical shell can be accurately described. For instance, the buckling pressure for long cylindrical shells evaluated using elliptical modes is $p_{\text{c, cyl}} = -\frac{3D}{{R_y}^3}$ [9]. Using similar methods, the indentation stiffness of zero-pressure cylindrical shells was derived in Ref. [3] to be

$$k_{\text{asy},0} \approx 1.37 \frac{Et^{\frac{5}{2}}}{R^{\frac{3}{2}}}. \tag{2.36}$$

In principle, the same non-shallow-shell techniques could be used to evaluate the indentation stiffness of cylinders at finite internal pressure. However, we find that the balance between pressure and elasticity gives rise to a characteristic deformation wavelength that quickly becomes small compared to the curvature radius as the internal pressure is increased, and the validity of shallow-shell results becomes re-established. To derive this new characteristic length, we notice that it is bending and not stretching which primarily dictates the deformation energy of cylinders because of the existence of the isometric deformation modes, as is evident from the expressions for the buckling pressure and the zero-pressure indentation stiffness. Accordingly, the characteristic extent of deformations of pressurized cylinders is obtained by balancing

the bending and tension terms in the total-energy functional, which leads to the result

$$\ell_p = \sqrt{\frac{D}{pR_y}}.$$

When the pressure becomes appreciable, this length scale falls far below the curvature radius R_y and our shallow-shell analysis, in particular the stiffness integral Eq. (2.26), can be used to derive the indentation of cylindrical shells. In Figure 2.3, the numerically-integrated indentation stiffness (black dashed line) is seen to agree with the results of finite-element simulations (from Ref. [2]) for pressures above $\eta_{\mathcal{R}} = 2\eta_{\mathrm{s},y} = 0.1$. At lower pressures, the stiffness crosses over to the zero-pressure result from Ref. [3] (yellow line).

In the remainder of this subsection, we develop analytical approximations for the indentation stiffness of cylinders which cover a wide range of pressures. To do so, we exploit the separation between the two pressure scales $\eta_{\mathrm{s},y}$ and $|p_{\mathrm{c,\ cyl}}|$ for thin shells, which allows us to evaluate the stiffness integral in "low-pressure" ($\eta_{\mathrm{s},y} \ll 1$) and "high-pressure" ($\eta_{\mathrm{s},y} \gg 1$) regimes while satisfying the condition $\ell_p \ll R_y$ for shallow-shell theory to be valid.

2.3.7.1 Validity of Shallow-Shell Theory in the Low-Pressure Limit $\eta_{\mathrm{s},y} \ll 1$. First, we will show that the shallow-shell theory is still valid for a range of pressures satisfying $\eta_{\mathrm{s},y} \ll 1$ for long cylindrical shells, provided that the shells are thin. The requirement $\ell_p \ll R_y$ amounts to $p \gg \frac{D}{{R_y}^3}$, a pressure scale related to the buckling pressure $p_{\mathrm{c,\ cyl}}$. To relate the two pressure scales p_{sc} (which underlies the dimensionless pressure $\eta_{\mathrm{s},y}$) and $\frac{D}{{R_y}^3}$, we write

$$\eta_{\mathrm{s},y} = \frac{p{R_y}^2}{4\sqrt{DY}} \equiv \frac{1}{4}\frac{p{R_y}^3}{D}\frac{1}{\sqrt{\gamma_y}}, \tag{2.37}$$

where the dimensionless Föppl-von Kármán number is

$$\gamma_y \equiv \frac{Y {R_y}^2}{D} \simeq 10 \left(\frac{R_y}{t}\right)^2.$$

For typical thin elastic shells, $0.001 \leq \frac{t}{R_y} \leq 0.05$ [9], so there exists a wide range of pressures which simultaneously satisfy $p \gg \frac{D}{{R_y}^3}$ (that is, $\ell_p \ll R_y$, and the shallow-shell theory holds) and $\eta_{\mathrm{s},y} \ll 1$ (the low-pressure limit for the stiffness integral). The wide range manifests the fact that due to a finite Gaussian curvature, a spherical shell is able to withstand more external forces than a long cylindrical shell of the same radius, i.e., the magnitude of the spherical shell's buckling pressure is larger.

2.3.7.2 Analytical Expressions for the Indentation Stiffness in the Limit $\eta_{\mathrm{s},y} \ll 1$.

We start our analysis of the stiffness integral [Eq. (2.26)] by setting $\beta = 1$:

$$I(\beta = 1, \eta_{\mathrm{s},y}) = \frac{1}{2\pi^2} \frac{\ell_{\mathrm{b},y}^2}{\kappa} \int_0^{\frac{\pi}{2}} \frac{\mathrm{d}\theta}{\sin^2\theta} \frac{\arccos\left(y(\eta_{\mathrm{s},y}, \theta)\right)}{\sqrt{1 - y^2(\eta_{\mathrm{s},y}, \theta)}},$$

where

$$y(\eta_{\mathrm{s},y}, \theta) \coloneqq \eta_{\mathrm{s},y} \frac{1 + \cos^2\theta}{\sin^2\theta} = \eta_{\mathrm{s},y} \left(2\cot^2\theta + 1\right).$$

Making the substitution $u = \cot\theta$, we can further reduce the stiffness integral:

$$I(\beta = 1, \eta_{\mathrm{s},y}) = \frac{1}{2\pi^2} \frac{\ell_{\mathrm{b},y}^2}{\kappa} \frac{1}{\sqrt{2\eta_{\mathrm{s},y}}} \int_0^{+\infty} \mathrm{d}u \, \frac{\arccos(u^2 + \eta_{\mathrm{s},y})}{\sqrt{1 - (u^2 + \eta_{\mathrm{s},y})^2}}.$$

Note that $\eta_{\mathrm{s},y}$ now couples with the integration variable u in an additive manner. Hence, for $\eta_{\mathrm{s},y} \ll 1$, we can write the stiffness integral as a power series of $\eta_{\mathrm{s},y}$

$$I = \frac{1}{8\pi^2} \frac{\ell_{\mathrm{b},y}^2}{\kappa} \times 2\sqrt{2} \sum_{n=0}^{\infty} \frac{1}{n!} \left[\int_0^{+\infty} \mathrm{d}u \, \left(D_{u^2}\right)^n \left(\frac{\arccos\left(u^2\right)}{\sqrt{1 - u^4}}\right)\right] \left(\eta_{\mathrm{s},y}\right)^{n - \frac{1}{2}}, \qquad (2.38)$$

where the differential operator $D_{u^2} \equiv \frac{\mathrm{d}}{\mathrm{d}(u^2)} = \frac{1}{2u}\frac{\mathrm{d}}{\mathrm{d}u}$. Truncating the series after the first four terms and numerically evaluating the coefficients gives the sought approximate expression for the indentation of cylindrical shells with pressures in the range $D/R_y^3 \ll p \ll 4\sqrt{DY}/R_y^2$:

$$I \approx \frac{1}{8\pi^2}\frac{\ell_{\mathrm{b},y}^2}{\kappa}\left(11.6\eta_{\mathrm{s},y}^{-1/2} - 2.66\eta_{\mathrm{s},y}^{1/2} + 1.83\eta_{\mathrm{s},y}^{3/2} - 0.998\eta_{\mathrm{s},y}^{5/2}\right). \tag{2.39}$$

The same series can be obtained by expanding the complete elliptic integral of the first kind in Eq. (3.36) for small $\eta_{\mathrm{s},y}$.

2.3.7.3 Analytical Expressions for the Indentation Stiffness of Cylindrical Shells that Are Highly Pressurized. At high pressures, the results of **Section 2.3.6.1** can be applied directly. For the cylindrical geometry ($\beta = 1$), the novel radius parameter becomes $\mathcal{R} = R_y\sqrt{1+\beta} = \sqrt{2}R_y$, and the Gaussian curvature is $K = 0$. Substituting these forms into Eq. (2.31, a) and then taking the inverse of the resulting expression, we obtain the indentation stiffness of long cylindrical shells in the large-pressure limit $\eta_{\mathrm{s},y} \gg 1$,

$$k_{\mathrm{cyl}} \approx \frac{4\pi\sqrt{DY}}{R_y}\sqrt{2}\frac{\eta_{\mathrm{s},y}}{\ln 8\eta_{\mathrm{s},y}}. \tag{2.40}$$

Figure 2.5 compares the numerically-evaluated stiffness for pressurized cylindrical shells {from inverting Eq. (2.26) to the low-pressure [Eq. (2.39)] and high-pressure [Eq. (2.40)] approximations}. We find that the analytical expressions recreate the indentation stiffness of long, thin cylindrical shells over almost all relevant pressures. To illustrate the separation of the scales p_{sc} and $|p_{\mathrm{c,\,cyl}}|$, we also show the pressure using the alternate scaling pR_y^3/D (upper horizontal axes), using the *E. coli* cell

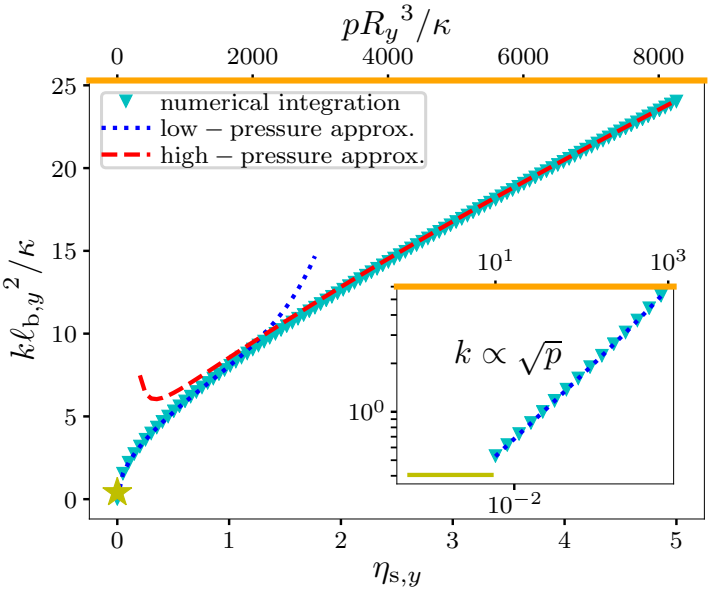

FIGURE 2.5. Scaled indentation stiffness as a function of pressure for an infinitely long, thin circular cylindrical shell. Results of numerical integration (symbols) are compared to the two approximate expressions derived for low pressures (dotted curve) and high pressures (dashed curve). The lower axis reports the rescaled pressure $\eta_{s,y} = p/p_{sc}$, whereas the upper axis (orange) uses the alternate pressure scale $D/R_y{}^3$ computed using the parameters $D = 1.76\times10^{-19}$ J and $R_y = 0.5$ μm representative of the *E. coli* cell wall [4]. The resulting Föppl-von Kármán number is $\gamma_y = 1.71 \times 10^5$. Shallow-shell theory is valid as long as $\frac{pR_y{}^3}{D} \gtrsim 10$. The zero-pressure stiffness $k_{asy,0}$ [Eq. (2.36)], calculated using different methods in Ref. [3], is marked by a star in the main panel and a solid line in the inset. Inset shows the low-pressure behavior on logarithmic scales, where the square-root dependence of indentation stiffness on pressure is apparent.

wall parameters to connect the two scales. Since the resulting Föppl-von Kármán number is very large, the criterion $\ell_p \ll R_y$ for the validity of our shallow-shell results is satisfied down to $\eta_{s,y} \sim 10^{-2}$. The inset verifies the predicted polynomial scaling of the indentation stiffness at low pressures from Eq. (2.39), and shows that the zero-pressure stiffness $k_{asy,0}$ from Ref. [3], Eq. (2.36), is approached at $\eta_{s,y} \approx 0.005$ ($pR_y^3/D \approx 10$). Although shallow-shell theory breaks down at this low pressure, we

expect that the true indentation behavior would cross over from our low-pressure expression to $k_{\mathrm{asy},0}$ around this pressure value.

2.3.7.4 Stiffness Switching. The high-pressure stiffness expression for cylinders, Eq. (2.40), is very similar to that of a sphere with the same elastic properties, radius, and internal pressure [Eq. (2.29)]. To compare the relative indentation stiffness of cylinders and spheres, we compute the ratio of the two expressions:

$$\frac{k_{\mathrm{cyl}}}{k_{\mathrm{sph}}} \approx \sqrt{2}\frac{\ln 2\eta_{\mathrm{s},y}}{\ln 8\eta_{\mathrm{s},y}}.$$

Notice that the ratio is equal to unity when $\eta_{\mathrm{s},y} = 2^{2\sqrt{2}+1} \approx 14.2$, beyond which long cylindrical shells become locally stiffer than spherical shells with the same scaled pressure. By contrast, the sphere was stiffer at zero pressure [Eq. (2.24)]. We term this phenomenon *stiffness switching* between long cylindrical and spherical shells. In general, stiffness switching tends to occur between any pair of spheroidal shells with different asphericities upon applying an internal pressure. The reason is as follows. Equation (2.24) implies that at low internal pressure, the indentation stiffness is dominated by the Gaussian curvature $K = \frac{1}{R_x R_y} = \frac{1-\beta}{{R_y}^2}$. On the other hand, $\mathcal{R}$ becomes the dominant radius parameter in the large-pressure limit, as one can rewrite the asymptotic indentation stiffness [the inverse of Eq. (2.33)] in a more illuminating form,

$$k \overset{\eta_{\mathcal{R}} \gg 1}{\approx} \frac{4\pi\sqrt{DY}}{\mathcal{R}}\frac{\eta_{\mathcal{R}}}{\ln 4\eta_{\mathcal{R}}} = \frac{\pi p \mathcal{R}}{\ln 4\eta_{\mathcal{R}}} = \frac{\pi p R_y \sqrt{1+\beta}}{\ln 4\eta_{\mathcal{R}}},$$

whence the dominance of $\mathcal{R}$ becomes more manifest. Stiffness switching is hence due to the fact that K and $\mathcal{R}$ have opposite β dependences: for a fixed R_y, $\sqrt{K}$ is proportional to $\sqrt{1-\beta}$, while $\mathcal{R}$ to $\sqrt{1+\beta}$. The phenomenon highlights

TABLE 2.1. Summary of analytical results for indentation stiffnesses.

Condition	Parameter ranges	Equation
Doubly-curved shells at zero pressure	$p = 0$, $\sqrt{R_y t} \ll R_x \ll R_y^2/t$	(2.24) or (B.1)
Spheroids at high internal pressure	$\eta_{\mathcal{R}} \gg 1 + \lvert\beta\rvert$, $-1 < \beta \leq 1$	(2.31) or (B.3)
Spheroids under external pressure close to local instability	$1 - \frac{p}{p_c} \ll 1$, $-1 < \beta < 1$	(2.35) or (B.6)
Cylinders at low internal pressure	$\frac{D}{R_y^3} \ll p \ll \frac{4\sqrt{DY}}{R_y^2}$, $\beta = 1$	(2.39) or (B.5)
Cylinders at high internal pressure	$p \gg \frac{4\sqrt{DY}}{R_y^2}$, $\beta = 1$	(2.40) or (B.4)

the contrasting contributions of geometry and internal pressure to the indentation stiffness of spheroidal shells.

2.4 Discussion

We have analyzed the linear indentation response of thin spheroidal and cylindrical shells under pressure, as a manifestation of geometric rigidity with practical applications. While our analysis is enabled by the simplifying assumptions of shallow-shell theory, we have identified parameter regimes for which these assumptions are valid, which turn out to encompass nearly all shell geometries and pressures which allow stable prestressed states. In addition to integral expressions for the inverse of the stiffness which can be numerically evaluated [Equations (2.23) and (2.26)], we have derived analytical expressions in various limits which rigorously validate prior results and provide easy-to-evaluate expressions for the indentation response as a function of geometric parameters, elastic properties, and pressure. Table 2.1 provides a summary of these results including references to the relevant expressions. For practical purposes, expressions written in terms of dimensionful, measurable quantities are more straightforward to utilize; in light of this, we

also provide the relevant dimensionful expressions in **Appendix B**. We have also validated a subset of our results against data from finite-element simulations of indentation assays which were reported in Ref. [2] (Figure 2.3).

Besides predictions of the indentation stiffness, our results provide insights into the nature of geometric rigidity and the influence of internal and external pressure. We revealed a connection between the loss of stiffness and the buckling instability of thin shells subjected to external pressure (**Section 2.3.4**), and showed that the behavior of the stiffness as the critical buckling pressure is approached differs qualitatively for spherical and general spheroidal shells (**Section 2.3.6.2** and Figure 2.4). At large internal pressures, we proposed a new length scale—the distensile curvature radius, $\mathcal{R}$ [Eq. (2.32)]—which captures the contribution of membrane prestresses to the indentation stiffness in a manner akin to how the Gaussian curvature radius $1/\sqrt{K}$ captured the geometric contribution. The contrasting behaviors of the distensile and Gaussian curvatures as the asphericity is varied makes cylindrical shells weaker than spherical shells of the same radius at low pressures, yet stronger at high pressures—a phenomenon we termed stiffness switching. The loss of rigidity of oblate shells with $\beta \leq -1$ at positive internal pressures is also captured by the distensile curvature taking on imaginary values.

Our result also provides new insights about the indentation stiffness of long, thin cylindrical shells. Cylinder indentation was previously studied in the zero-pressure limit [3] and the membrane limit which incorporated the effects of pressure-related stresses while ignoring elastic stiffness [1, 4]. We connect these disparate regimes by exploiting a separation of pressure scales which arises for thin cylinders, which allowed us to calculate the indentation stiffness of cylindrical shells over a wide range of pressures (**Section 2.3.7** and Figure 2.5).

Our analysis points to several promising directions for future studies. While we focused on pressurized spheroidal shells, our approach could be used to find the indentation stiffness of any thin curved shell for which the in-plane stresses in the vicinity of the indentation point are known, as long as shallow-shell theory is applicable. For instance, the indentation stiffness of general ellipsoids could be numerically evaluated, even away from high-symmetry points. The approach could be extended to include the effects of a fluid or solid continuum in the shell interior, as well as material anisotropy in the shell, all of which are particularly relevant to biological structures. It would also be interesting to analyze the indentation behavior beyond the linear regime, which would require extending the Pogorelov scaling for the energetics of large inversions of spherical shells [16, 46, 47] to anisotropic geometries. Understanding the large-inversion behavior would also provide insight into the post-buckling shapes of general spheroids; in this regard, the case $\beta \leq -1$ will be particularly interesting since this type of shells has two buckling states for negative and positive pressures. Finally, it would be interesting to extend our technique to basis functions beyond the Fourier modes we use in our analysis, which would allow us to tackle non-shallow-shells and to consider the effects of edge constraints (e.g. indentation of clamped spherical caps).

Having just quantified the effects of geometric anisotropy on shell elasticity, we now consider shells made of an anisotropic material and study the associated effects of material anisotropy.

CHAPTER III

A GEOMETRIC MAPPING FROM RECTILINEAR MATERIAL ORTHOTROPY TO ISOTROPY: INSIGHTS TO PLATES AND SHELLS

The content of this chapter was posted in a preprint on `arXiv` in August 2023. I performed the analytical calculations and theoretical analysis, did `COMSOL` simulation on shell indentation and wrote the manuscript. Cody Rasmussen, my former group member, helped substantially with setting up and running the `COMSOL` simulation. Roman Vetter, an external researcher from the ETH Zürich, provided `C++` data on shell buckling, wrote the **Appendix H** and edited the manuscript. Jayson Paulose supervised the research, wrote and edited the manuscript.

3.1 Introduction

Isotropic elasticity, which assumes material properties that are independent of direction, provides a tractable and convenient description of many everyday mechanical phenomena. However, direction-dependent mechanical properties are the rule rather than the exception in natural materials, from muscle tissue [48] and wood [49] to the cell walls of bacteria [19] and plants [13]. The mechanical anisotropy is typically a result of high-strength filaments or fibers within these materials that are oriented in a particular direction, strengthening the direction and hence breaking the material rotational symmetry (i.e., isotropy) [10]. In the technological realm, composite materials with directional reinforcements such as plywood [50] and corrugated materials [9] are used to build structures that are mechanically strong and resilient in desired directions; the elastic description of

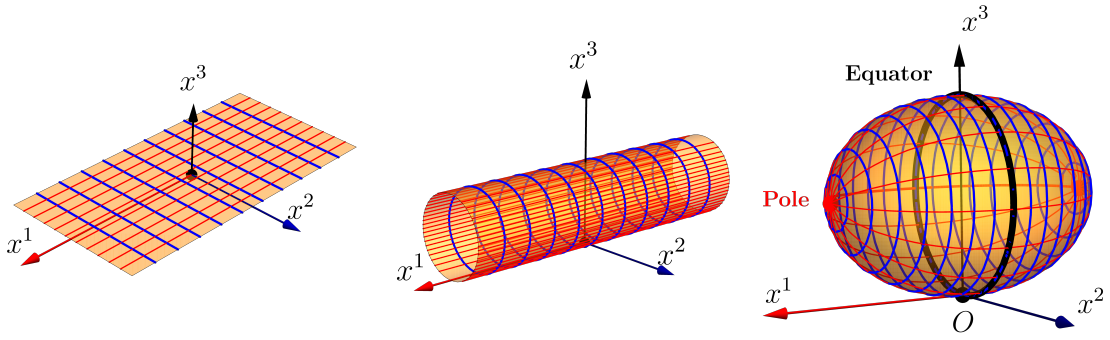

(a) An orthotropic plate (b) An orthotropic cylinder (c) An orthotropic spheroid

FIGURE 3.1. Plates and shells with local rectilinear orthotropy. The two material orthotropic directions are marked by different colors, the x^1-direction by red and x^2-direction by blue. For all the three structures, these two directions are also the principal directions of curvature. In this paper, we only consider rectilinear orthotropy—shell sections that locally look like (a); shell regions that are curvilinearly orthotropic, e.g., the poles of the orthotropic spheroid, are beyond the scope of this study. For curved shells, (b) and (c), we take the x^2-direction to be the azimuthal direction, so R_2 denotes the equatorial radius of the spheroid.

these structures at length scales larger than the reinforcement features also requires anisotropic material parameters.

Thin-walled elastic structures, or shells, provide a rich setting for interesting elastic phenomena that arise from the interplay of material anisotropy and geometry. For example, a thin cylindrical shell whose inner wall is wrapped helically by polymer fibers can develop into a spiral shape upon expansion, which has been proposed as a model for bacterial growth [51]. In engineered shell structures, closely spaced ribs provide strength in high-stress directions with minimal addition of material in e.g., masonry domes [52] and pressure vessels [53]; these directional reinforcements strongly influence the failure modes of the shells [54] and can generate multistability in shell conformations [6, 55, 56, 57]. Besides its fundamental interest to mechanics, the interplay of anisotropic elasticity, shell geometry and external loading is crucial to our understanding of cell biophysics as well as to structural engineering.

One obstacle to building a fundamental understanding of shells with anisotropic elasticity is that the reduction in material symmetries makes the governing differential equations more challenging to solve. For instance, twenty-one independent elastic constants are needed to fully characterize a three-dimensional anisotropic material (while only two are needed in the isotropic case) [7, 9]. Here, we study a particular type of material anisotropy—two-dimensional orthotropic materials (or equivalently thin three-dimensional transversely isotropic materials). Such materials have different elastic properties along two orthogonal in-plane directions, one of which has the same material composition as the material thickness direction [50], see Fig. 3.1. This form of anisotropy provides a good approximation to engineered thin-walled structures such as fiber-reinforced shells [9, 58] and shells with linear corrugations [59]. Orthotropic elasticity also arises as a natural consequence of the growth mechanism of rod-shaped bacterial cell walls, in which stiff carbohydrate chains are laid down by molecular complexes along the circumferential direction [60, 61, 62] breaking local material symmetry [1, 63]. Orthotropy therefore serves as a tractable yet relevant model for assessing the influence of material anisotropy on shell mechanics. Nevertheless, the lowered symmetry of the governing shell equations has typically favored numerical analyses of orthotropic shell response [54, 64, 65, 66, 67, 68], although a few analytical results exist for buckling thresholds [69] and multistability criteria [6, 55, 56, 57] of orthotropic shells.

In this work, we establish an exact mapping between orthotropic and isotropic shells, and apply this mapping to generate analytical results for the local mechanical response of orthotropic shells. Specifically, we will demonstrate that although the orthotropic materials still have a reduced symmetry compared to isotropic materials, they become effectively isotropic under an appropriately chosen coordinate

transformation. A specific version of this isotropy-orthotropy equivalence have been recognized for linear orthotropic plate equations [70, 71]; here, we rigorously establish the equivalence using the tensor formulation of elasticity, and generalize it to nonlinear deflections of curved shell sections described by shallow-shell theory [9]. Under the aforementioned coordinate transformation, the orthotropic shallow-shell equations are mapped to a system of equations describing a shallow shell made of an isotropic material, but with different geometric parameters. We apply the transformation to study local mechanical properties—linear response to an indentation force [14, 24, 25, 72] and buckling load—of thin-walled structures that are made of orthotropic materials. These local mechanical properties have recently been established rigorously for isotropic shells with arbitrary curvatures and pressures [5, 14, 72]; however, to our knowledge, our mapping enables the first analytical results for the local response of orthotropic shells.

3.2 Background

We start with the elastic description for a two-dimensional[1] orthotropic material, which relates local strains to local stresses via a stiffness tensor. Let $u_{\alpha\beta}$ be the covariant components of the strain tensor, and let $\sigma^{\alpha\beta}$ denote the contravariant components of the stress tensor; $(\alpha, \beta \in \{1, 2\})$. The generalized Hooke's law for an orthotropic material is: $u_{\alpha\beta} = C_{\alpha\beta\gamma\delta}\, \sigma^{\gamma\delta}$, where $\mathbf{C}$ is the rank-four stiffness tensor [7]. (The Einstein convention of summation over repeated upper and lower indices is

[1]Realistically, every material has a finite thickness and is hence three-dimensional. The materials considered here are effectively two-dimensional, i.e., so thin that the Kirchhoff-Love hypothesis [9] applies.

implied throughout the paper.) In Voigt notation, this reads [50]

$$\begin{pmatrix} u_{11} \\ u_{22} \\ u_{12} \end{pmatrix} = \begin{pmatrix} \dfrac{1}{E_1} & -\dfrac{\upsilon_{12}}{E_2} & 0 \\ -\dfrac{\upsilon_{21}}{E_1} & \dfrac{1}{E_2} & 0 \\ 0 & 0 & \dfrac{1}{2G_{12}} \end{pmatrix} \begin{pmatrix} \sigma^{11} \\ \sigma^{22} \\ \sigma^{12} \end{pmatrix}, \tag{3.1}$$

where E_α and $\upsilon_{\alpha\beta}$ ($\alpha \neq \beta$) denote Young's moduli and Poisson's ratios along the two orthogonal directions, respectively. In this paper, we consider the common case where these elastic constants are all positive. By Betti's reciprocal theorem [9],

$$\frac{\upsilon_{12}}{E_2} = \frac{\upsilon_{21}}{E_1}. \tag{3.2}$$

We can accordingly define a parameter which characterizes the degree of material anisotropy:

$$\lambda \coloneqq \frac{E_1}{E_2} = \frac{\upsilon_{21}}{\upsilon_{12}} > 0. \tag{3.3}$$

The positive definiteness of the stiffness matrix in Voigt notation, $\det\left(C_{[\alpha\beta][\gamma\delta]}\right) > 0$, imposes an upper bound for the anisotropy parameter: $\lambda < \frac{1}{\upsilon_{12}^2}$. The Poisson's ratio υ_{12} can in principle be zero [73]; as a result, $\lambda \in (0, \infty)$ (recall that we assume $\upsilon_{12}, \upsilon_{21} > 0$). The inverse of λ, $\frac{1}{\lambda} \coloneqq \frac{E_2}{E_1}$, also has the same range of values. In practice, given a general two-dimensional orthotropic material, one is free to call the first direction either of the two principal directions of the stiffness tensor $\mathbf{C}$ and hence use either λ or $\frac{1}{\lambda}$ to characterize the degree of material anisotropy.

Because of Eq. (3.2), one only needs four independent parameters to fully characterize a two-dimensional orthotropic material. We choose the four to be $E_{\text{eff}} \coloneqq \sqrt{E_1 E_2}$, $\upsilon_{\text{eff}} \coloneqq \sqrt{\upsilon_{12}\upsilon_{21}}$, λ and G_{12}. We will see the reason for this choice in Eq. (3.4) and **Section 3.3.1**. The elastic constant G_{12} is the material's in-plane shear modulus and is, in general, an independent quantity. However, in practice it is closely related to the Young's moduli in the orthotropic directions. To eliminate this degree of freedom, M. T. Huber proposed the following form for G_{12} [74],

$$G_{12} \overset{!}{=} \frac{E_{\text{eff}}}{2(1+\upsilon_{\text{eff}})} = \frac{\sqrt{E_1 E_2}}{2(1+\sqrt{\upsilon_{12}\upsilon_{21}})}, \tag{3.4}$$

substituting the *geometric means* of the anisotropic elastic constants as effective constants into the expression of the shear modulus of an isotropic material. The Huber form for the orthotropic shear modulus has been accepted and widely employed in both analytical and numerical calculations [9, 54, 70, 75, 76]. Panc demonstrated, based on theoretical arguments, that for orthotropic materials, the Huber form may be used as an approximation [71]. Cheng and He further argued that although the Huber form is itself inaccurate for fiber-reinforced composite materials, it can still yield accurate analytical results when substituted in governing differential equations of shell theory (at least for cylinders) [75].

The following result section is structured as follows. In **Section 3.3.1**, we introduce the main result of this paper–the rescaling transformation which shows that an orthotropic two-dimensional material becomes effectively isotropic if we use a rescaled Cartesian coordinate system. In **Section 3.3.2**, we exploit the use of the transformation in shallow-shell systems. We demonstrate that the general Donnell-Mushtari-Vlasov (DMV) equations, the governing equations in the shallow-shell theory, are covariant under the transformation and use the transformation to

derive the DMV equations for orthotropic shells in a physically transparent manner. In **Section 3.3.4** and **Section 3.3.5**, by solving these equations, we obtain the indentation stiffness and buckling pressure of orthotropic ellipsoids and cylinders.

3.3 Results

3.3.1 A Rescaling Transformation

Transformation Step 1. We first notice that with the Huber form [Eq. (3.4)], Eq. (3.1) can be rewritten, in terms of the effective elastic constants and the anisotropy parameter λ, as

$$\begin{pmatrix} \sqrt[4]{\lambda}u_{11} \\ \dfrac{1}{\sqrt[4]{\lambda}}u_{22} \\ u_{12} \end{pmatrix} = \begin{pmatrix} \dfrac{1}{E_{\text{eff}}} & -\dfrac{\upsilon_{\text{eff}}}{E_{\text{eff}}} & 0 \\ -\dfrac{\upsilon_{\text{eff}}}{E_{\text{eff}}} & \dfrac{1}{E_{\text{eff}}} & 0 \\ 0 & 0 & \dfrac{1+\upsilon_{\text{eff}}}{E_{\text{eff}}} \end{pmatrix} \begin{pmatrix} \dfrac{1}{\sqrt[4]{\lambda}}\sigma^{11} \\ \sqrt[4]{\lambda}\sigma^{22} \\ \sigma^{12} \end{pmatrix}. \tag{3.5}$$

The stiffness matrix now takes the form of that for an isotropic material with elastic constants $\{E_{\text{eff}}, \upsilon_{\text{eff}}\}$ [50]. Equation (3.5) in fact implies that an orthotropic material can be treated as isotropic if we rescale physical quantities in a systematic way. This can be seen more clearly using tensors. In tensor notation, Eq. (3.5) can be written as $u_{\alpha'\beta'} = C_{\alpha'\beta'\gamma'\delta'}\,\sigma^{\gamma'\delta'}$. Primed indices are used here to denote the transformed tensor components:

$$u_{\alpha'\beta'} = \Lambda^{\alpha}{}_{\alpha'}\,\Lambda^{\beta}{}_{\beta'}\,u_{\alpha\beta}, \tag{3.6, a}$$

$$\sigma^{\alpha'\beta'} = \Lambda^{\alpha'}{}_{\alpha}\,\Lambda^{\beta'}{}_{\beta}\,\sigma^{\alpha\beta}, \tag{3.6, b}$$

and

$$C_{\alpha'\beta'\gamma'\delta'} = \Lambda^{\alpha}{}_{\alpha'}\,\Lambda^{\beta}{}_{\beta'}\,\Lambda^{\gamma}{}_{\gamma'}\,\Lambda^{\delta}{}_{\delta'}\,C_{\alpha\beta\gamma\delta}, \tag{3.6, c}$$

where $(\Lambda^{i}{}_{i'}) \coloneqq \operatorname{diag}\left\{\sqrt[8]{\lambda}, \frac{1}{\sqrt[8]{\lambda}}, 1\right\}$, and $\Lambda^{i}{}_{i'}\,\Lambda^{i'}{}_{j} = \delta^{i}_{j}$ with δ^{i}_{j} the Kronecker delta. (Latin indices run from 1 to 3, while Greek indices only take on values 1 and 2.) That is, when written in terms of the rescaled tensor components, the anisotropic Hooke's law takes the isotropic form. This shows that the orthotropic material becomes effectively isotropic if we hide the material anisotropy by rescaling the strain and the stress components. We note that this rescaling transformation preserves the elastic energy density: $\frac{1}{2}u_{\alpha\beta}\,\sigma^{\alpha\beta} = \frac{1}{2}u_{\alpha'\beta'}\,\sigma^{\alpha'\beta'}$.

In fact, the total elastic energy is also invariant under the transformation. Equations (3.6) hint at the following coordinate transformation:

$$x^{i'} = \Lambda^{i'}{}_{j}\,x^{j}. \tag{3.7}$$

Let g_{ij} denote the unscaled components of the metric tensor; its rescaled components can then be computed: $g_{i'j'} = \Lambda^{i}{}_{i'}\,\Lambda^{j}{}_{j'}\,g_{ij}$. Note that $\det(g_{i'j'}) = \det(g_{ij})$, since $\det(\Lambda^{i}{}_{i'}) = 1$. This further implies that

$$U = \frac{1}{2}\int_{\mathcal{M}} \sqrt{\det(g_{ij})}\,\mathrm{d}^2\mathbf{x}\,u_{\alpha\beta}\,\sigma^{\alpha\beta} = \frac{1}{2}\int_{\mathcal{M}'} \sqrt{\det(g_{i'j'})}\,\mathrm{d}^2\mathbf{x}'\,u_{\alpha'\beta'}\,\sigma^{\alpha'\beta'}, \tag{3.8}$$

i.e., the total energy is preserved.

Transformation Step 2. The strain tensor is related to deformation displacement fields via the so-called strain-displacement relations. We are now going to demonstrate that the rescaling transformation is compatible with these relations. Since all materials are three-dimensional, we will use the relations for a thin curved

material (i.e., a shallow shell) that satisfies the Kirchhoff-Love hypothesis [9], which basically assumes that no deformation occurs along the thickness direction.

For such a shell, the Green-Lagrange strain tensor is given, in terms of two in-plane phonon fields $u_\alpha(\mathbf{x})$ and one out-of-plane deformation field $u_3(\mathbf{x})$, by [9, 31]

$$u_{\alpha\beta} = \frac{1}{2}\left(\partial_\alpha u_\beta + \partial_\beta u_\alpha + \partial_\alpha u_3 \cdot \partial_\beta u_3\right) - \mathcal{K}^0_{\alpha\beta}\, u_3 - x_3\, \partial_\alpha \partial_\beta u_3, \tag{3.9}$$

where $\partial_\alpha \equiv \frac{\partial}{\partial x^\alpha}$, and $(\mathcal{K}^0_{\alpha\beta}) = \mathrm{diag}\,\{\kappa_1, \kappa_2\}$ is the extrinsic curvature tensor that encodes the two local principal curvatures of the material's undeformed middle surface. For a sphere with radius R, $\mathcal{K}^0_{\alpha\beta} = \frac{1}{R}\,\delta^\alpha_\beta$, while a cylinder of the same radius has $\mathcal{K}^0_{\alpha\beta} = \frac{1}{R}\,\delta^1_\alpha\,\delta^1_\beta$ (or $\mathcal{K}^0_{\alpha\beta} = \frac{1}{R}\,\delta^2_\alpha\,\delta^2_\beta$). The last term in Eq. (3.9) is the bending strain [9], where x_3 denotes the distance away from the middle surface.

The rescaled components can then be written, using Eq. (3.6, a), as

$$\begin{aligned} u_{\alpha'\beta'} &= \frac{1}{2}\Big[\left(\Lambda^\alpha{}_{\alpha'}\,\partial_\alpha\right)\left(\Lambda^\beta{}_{\beta'}\,u_\beta\right) + \left(\Lambda^\beta{}_{\beta'}\,\partial_\beta\right)\left(\Lambda^\alpha{}_{\alpha'}\,u_\alpha\right) + \left(\Lambda^\alpha{}_{\alpha'}\,\partial_\alpha\right) u_3 \cdot \left(\Lambda^\beta{}_{\beta'}\,\partial_\beta\right) u_3\Big] - \\ &\quad - \left(\Lambda^\alpha{}_{\alpha'}\,\Lambda^\beta{}_{\beta'}\,\mathcal{K}^0_{\alpha\beta}\right) u_3 - x_3\,\left(\Lambda^\alpha{}_{\alpha'}\,\partial_\alpha\right)\left(\Lambda^\beta{}_{\beta'}\,\partial_\beta\right) u_3 \\ &= \frac{1}{2}\left(\partial_{\alpha'} u_{\beta'} + \partial_{\beta'} u_{\alpha'} + \partial_{\alpha'} u_{3'} \cdot \partial_{\beta'} u_{3'}\right) - \mathcal{K}^0_{\alpha'\beta'}\, u_{3'} - x_{3'}\,\partial_{\alpha'}\partial_{\beta'} u_{3'}. \end{aligned} \tag{3.10}$$

For the sake of consistency, we have written in the above equation $x_{3'} = \Lambda^i{}_{3'}\,x_i = x_3$ and $u_{3'} = \Lambda^i{}_{3'}\,u_i = u_3$. Note that both the coordinate and the displacement along the thickness direction remain unrescaled.

Equations (3.9) and (3.10) take exactly the same form. This means that rescaling the underlying deformation displacement fields can indeed lead to the rescaled strain-tensor field, indicating the compatibility between the rescaling transformation and the strain-displacement relations. The only difference between the two equations is

that the extrinsic curvature tensor, in the rescaled coordinate system, now becomes

$$(\mathcal{K}^0_{\alpha'\beta'}) = \mathrm{diag}\left\{\kappa_{1'}, \kappa_{2'}\right\} \coloneqq \mathrm{diag}\left\{\sqrt[4]{\lambda}\kappa_1, \frac{1}{\sqrt[4]{\lambda}}\kappa_2\right\}. \tag{3.11}$$

This shows that the material's middle surface has a different local geometry in the rescaled coordinate system. For example, a sphere with radius R becomes locally an ellipsoid with principle radii of curvature $\frac{1}{\sqrt[4]{\lambda}}R$ and $\sqrt[4]{\lambda}R$. Nonetheless, note that the local Gaussian curvature remains unchanged:

$$K \equiv \det(\mathcal{K}^0_{\alpha\beta}) = \kappa_1\kappa_2 = \det(\mathcal{K}^0_{\alpha'\beta'}) \equiv K', \tag{3.12}$$

while the other invariant of the extrinsic curvature tensor, the local mean curvature $H \equiv \frac{1}{2}\,\mathrm{tr}(\mathcal{K}^0_{\alpha\beta})$, does not remain invariant under the rescaling:

$$H = \frac{1}{2}\left(\kappa_1 + \kappa_2\right) \neq \frac{1}{2}\left(\kappa_{1'} + \kappa_{2'}\right) = \frac{1}{2}\,\mathrm{tr}(\mathcal{K}^0_{\alpha'\beta'}) \equiv H'. \tag{3.13}$$

To sum up, we have established a curious rescaling transformation [Eqs. (3.7) and (3.6)], assuming the Huber form for the orthotropic in-plane shear modulus. The transformation implies that under certain circumstances, such as cases where shear deformations are negligible, an orthotropic material can exhibit similar elastic behaviors as an isotropic one with different local geometrical properties.

It should be pointed out that we have made a couple of assumptions when establishing the above equivalence relationship. The first one is that the material-orthotropy pattern must be *rectilinear* (i.e., can be characterized locally by a Cartesian coordinate system), not *curvilinear*, and the two orthogonal directions have to coincide with directions of local principal curvatures. Also, the form of

the strain tensor, Eq. (3.9), implicitly requires that the deformation displacements vary rapidly, on the scale of curvature radii, along the principal directions, i.e., $\left|\frac{1}{u_\beta}\partial_\alpha u_\beta\right| \gg \frac{1}{\min\{R_1,R_2\}}$, where $R_\alpha \equiv \frac{1}{\kappa_\alpha}$ [9]. Given that λ is of order one, which implies that $\sqrt[8]{\lambda}$ is approximately unity, the same requirement in the rescaled coordinate system, $\left|\frac{1}{u_{\beta'}}\partial_{\alpha'} u_{\beta'}\right| \gg \frac{1}{\min\{R_{1'},R_{2'}\}}$, can accordingly still be satisfied. In the context of thin shells, this means that a shallow shell remains shallow after getting rescaled.

We now move on to discuss several implications of the established equivalence relationship. The first and foremost perhaps is that we can effortlessly obtain, without performing any functional analysis, the equation of equilibrium and the compatibility equation for an orthotropic doubly-curved shallow shell. The equations will be presented in a covariant way, in tensor notation, to illustrate that they are form-invariant under the rescaling transformation.

3.3.2 Equations of the Shallow-Shell Theory

Recall that we have demonstrated that an orthotropic shallow shell with the set of parameters $\{E_1, \upsilon_{21}, \lambda; R_1, R_2\}$ shares the same total-energy functional with an *isotropic* one whose corresponding parameters are given by $\left\{E_{\text{eff}} \equiv \sqrt{E_1 E_2}, \upsilon_{\text{eff}} \equiv \sqrt{\upsilon_{12}\upsilon_{21}}; R_{1'} \equiv \frac{R_1}{\sqrt[4]{\lambda}}, R_{2'} \equiv \sqrt[4]{\lambda} R_2\right\}$. Since minimizing the total-energy functional gives the equation of equilibrium (EOE), we conclude that the EOE for the orthotropic shell will be the same as the corresponding isotropic EOE when written in terms of rescaled quantities

$$D' \, \boldsymbol{\pounds}' \, u_{3'} + \sigma^{\alpha'\beta'} t' \left(\mathcal{K}^0_{\alpha'\beta'} - \partial_{\alpha'}\partial_{\beta'} u_{3'}\right) = p'\left(x^{\alpha'}\right), \qquad (3.14,\ \text{a})$$

where $D' \coloneqq \frac{E_{\text{eff}} t^3}{12(1-\upsilon_{\text{eff}}^2)}$ is the effective bending modulus; $t = t'$ the shell thickness; and p' describes the load applied to the shell. The operator $\boldsymbol{\pounds}'$ denotes the linear differential operator $\frac{\partial^4}{\partial x'^4} + 2\frac{\partial^2}{\partial x'^2}\frac{\partial^2}{\partial y'^2} + \frac{\partial^4}{\partial y'^4}$.[2] Note that in spite of its appearance, $\boldsymbol{\pounds}'$ is in fact *not* the biharmonic operator in the rescaled coordinate system.[3]

Recall that the strain-displacement relations [Eq. (3.9)] also take the same form in both coordinate systems. By the same reasoning, the fact that the compatibility equation stems from strain-displacement relations [77] implies that for the orthotropic shell, the compatibility equation is given by

$$\frac{1}{Y'}\,\boldsymbol{\pounds}'\,\Phi' = \varepsilon^{\alpha'\gamma'}\varepsilon^{\beta'\delta'}\partial_{\gamma'}\partial_{\delta'}u_{3'}\left(\mathcal{K}^0_{\alpha'\beta'} - \frac{1}{2}\partial_{\alpha'}\partial_{\beta'}u_{3'}\right), \tag{3.14, b}$$

where $Y' \coloneqq E_{\text{eff}} t$ is the effective two-dimensional Young's modulus. The Airy stress function Φ' is a scalar field and hence unrescaled, i.e., $\Phi'\left(x^{\alpha'}\right) = \Phi(x^{\alpha})$. It is related to the rescaled stress components in the following way

$$\sigma^{\alpha'\beta'}t' = \varepsilon^{\alpha'\gamma'}\varepsilon^{\beta'\delta'}\partial_{\gamma'}\partial_{\delta'}\Phi', \tag{3.15}$$

where $\varepsilon^{\alpha'\beta'}$ is the rescaled components of the two-dimensional alternating tensor.

---

[2]The fully covariant way of writing the operator is $D^{\alpha\beta\gamma\delta}\,\partial_\alpha\partial_\beta\partial_\gamma\partial_\delta$, where $\mathbf{D}$ denotes the bending-stiffness tensor: In Voigt notation,

$$\left(D^{[\alpha\beta][\gamma\delta]}\right) = \begin{pmatrix} D^{1111} & D^{1122} & D^{1112} & D^{1121} \\ D^{2211} & D^{2222} & D^{2212} & D^{2221} \\ D^{1211} & D^{1222} & D^{1212} & D^{1221} \\ D^{2111} & D^{2122} & D^{2112} & D^{2121} \end{pmatrix} = D' \begin{pmatrix} \sqrt{\lambda} & \upsilon_{\text{eff}} & 0 & 0 \\ \upsilon_{\text{eff}} & \frac{1}{\sqrt{\lambda}} & 0 & 0 \\ 0 & 0 & \frac{1-\upsilon_{\text{eff}}}{2} & \frac{1-\upsilon_{\text{eff}}}{2} \\ 0 & 0 & \frac{1-\upsilon_{\text{eff}}}{2} & \frac{1-\upsilon_{\text{eff}}}{2} \end{pmatrix},$$

again using the Huber form.

[3]The Laplacian operator, or rather the Laplace-Beltrami operator, in the rescaled coordinate system, which is non-Euclidean, is $\Delta' \equiv \frac{1}{\sqrt{g'}}\partial_{\alpha'}\left(\sqrt{g'}g^{\alpha'\beta'}\,\partial_{\beta'}\right) = \frac{1}{\sqrt[4]{\lambda}}\frac{\partial^2}{\partial x'^2} + \sqrt[4]{\lambda}\frac{\partial^2}{\partial y'^2}$, where $g' \equiv \det(g_{\alpha'\beta'})$.

Equations (3.14) are the nonlinear shallow-shell equations for the orthotropic shell. The linearized version can be obtained via the procedure outlined in Ref. [9]; the results are shown below:

$$D' \boldsymbol{\pounds}' u_{3'} + \sigma^{\alpha'\beta'} t' \mathcal{K}^0_{\alpha'\beta'} - \sigma_0^{\alpha'\beta'} t' \partial_{\alpha'} \partial_{\beta'} u_{3'} = 0 \qquad (3.16, \text{a})$$

$$Y' \varepsilon^{\alpha'\gamma'} \varepsilon^{\beta'\delta'} \mathcal{K}^0_{\alpha'\beta'} \partial_{\gamma'} \partial_{\delta'} u_{3'} = \boldsymbol{\pounds}' \Phi', \qquad (3.16, \text{b})$$

where $\sigma_0^{\alpha'\beta'}$ denotes the rescaled prestress components. Equations (3.16) are consistent with known expressions in the literature [78]. Equations written in terms of unrescaled quantities without tensor notation can be found in **Appendix C**.

The linearized equations can be employed to study the local indentation stiffness of a shell subject to a concentrated load and to perform linear buckling analysis [17], which will be the topics for the following discussions.

3.3.3 Re-Deriving Some Established Results Using the Rescaling Transformation

We first demonstrate the convenience of the rescaling transformation by deriving the buckling load of orthotropic cylinders and plates from the corresponding isotropic expressions. Our results are consistent with the established expressions in literature.

3.3.3.1 Long Cylindrical Shells.

Edge Load. By "edge load" we mean the load applied at the ends of an open cylindrical shell; it has units of pressure. Paschero and Hyer have observed the curious fact that the critical edge load of an orthotropic cylinder, when the real in-plane shear modulus is large enough (so that shear deformations are negligible), is

exactly the classical buckling load of an isotropic cylinder with elastic constants E_{eff} and υ_{eff} [76]. The rescaling transformation provides an explanation for this fact. The isotropic critical axial stress is in this case [9]

$$\sigma^{11}_{\text{c, iso}} = \frac{E}{\sqrt{3(1-\upsilon^2)}}\frac{t}{R}. \tag{3.17}$$

Since an orthotropic cylinder can be treated effectively as isotropic with a modified radius, we can use the same formula to write the *rescaled* orthotropic critical stress:

$$\sigma^{1'1'}_{\text{c, ortho}} = \frac{E_{\text{eff}}}{\sqrt{3(1-\upsilon^2_{\text{eff}})}}\frac{t}{R'}. \tag{3.18}$$

Now recall that $\sigma^{1'1'} = \frac{1}{\sqrt[4]{\lambda}}\sigma^{11}$, and $R' = \sqrt[4]{\lambda}R$. Substituting these into the above expression will yield the desired result

$$\sigma^{11}_{\text{c, ortho}} = \frac{E_{\text{eff}}}{\sqrt{3(1-\upsilon^2_{\text{eff}})}}\frac{t}{R}. \tag{3.19}$$

Surface Load. In this case, a uniform pressure is applied at the outer surface of an open cylindrical shell. The isotropic critical circumferential stress is known as [9]

$$\sigma^{22}_{\text{c, iso}} t = \frac{D}{R^2}\left(n^2-1\right) \equiv \frac{D}{R^2}\left(n^2-n^2_{\min}\right), \tag{3.20}$$

where n is the number of half-waves in the circumferential direction. To obtain the orthotropic critical stress, we again substitute into the above expression the effective

elastic constants and the rescaled quantities:

$$\begin{aligned}\sigma^{2'2'}_{\text{c, ortho}}t &= \frac{D'}{R'^2}\left(n'^2 - {n'_{\min}}^2\right)\\ \sqrt[4]{\lambda}\sigma^{22}_{\text{c, ortho}}t &= \frac{\sqrt{\lambda}D_\theta}{\sqrt{\lambda}R^2}\left(\sqrt[4]{\lambda}n^2 - \sqrt[4]{\lambda}\right);\end{aligned} \tag{3.21}$$

$n' = \frac{R'}{R}\frac{y}{y'}n = \sqrt[8]{\lambda}n$ is the rescaled half-wave number [see Eq. (E.13)]. That it is not integral and related to the anisotropy parameter λ arises from the following fact. Although distances and radii of curvature have the same dimension, the former are related to the square root of the metric, while the latter get rescaled in the same way as the metric since both the extrinsic curvature tensor and the metric tensor are rank-two. Cancelling all factors involving λ, we get

$$\sigma^{22}_{\text{c, ortho}}t = \frac{D_\theta}{R^2}\left(n^2 - 1\right), \tag{3.22}$$

which is consistent with the result by Wang et al. [79].

3.3.3.2 Plates. We consider here a rectangular orthotropic plate which is subject to in-plane compressive forces. The edges of the plate are simply supported; in other words, bending moments shall vanish along the edges which are held fixed but allowed to rotate during a deformation event [see Eqs. (3.23)]. We assume that shear deformations are negligible. In this case, the rescaling transformation maps the orthotropic plate with parameters $\{E_1, \upsilon_{21}, \lambda; a, b; \sigma^{11}\}$ to an isotropic plate with parameters $\left\{E_{\text{eff}}, \upsilon_{\text{eff}}; a' = \frac{a}{\sqrt[8]{\lambda}}, b' = \sqrt[8]{\lambda}b; \sigma^{1'1'}\right\}$. (See Fig. 3.2 for labels.) It should be pointed out that the orthotropic boundary conditions also become effectively

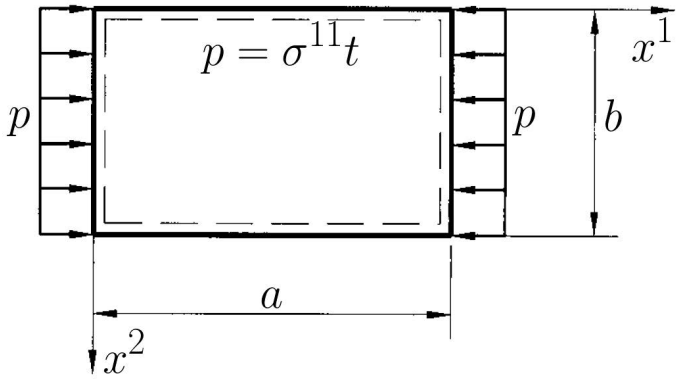

FIGURE 3.2. A rectangular plate with side lengths a and b, being compressed horizontally. The intensity of the forces is p, which equals $\sigma^{11} t$ by force balancing at equilibrium.

isotropic, i.e.,

$$\begin{cases} u_3|_{\substack{x=0,a \\ y=0,b}} = 0, \\ \left(\dfrac{\partial^2 u_3}{\partial x^2} + \upsilon_{12} \dfrac{\partial^2 u_3}{\partial y^2} \right)\Big|_{x=0,a} = 0, \\ \left(\dfrac{\partial^2 u_3}{\partial y^2} + \upsilon_{21} \dfrac{\partial^2 u_3}{\partial x^2} \right)\Big|_{y=0,b} = 0, \end{cases} \quad \mapsto \quad \begin{cases} u_3|_{\substack{x'=0,a' \\ y'=0,b'}} = 0, \\ \left(\dfrac{\partial^2 u_3}{\partial x'^2} + \upsilon_{\text{eff}} \dfrac{\partial^2 u_3}{\partial y'^2} \right)\Big|_{x'=0,a'} = 0, \\ \left(\dfrac{\partial^2 u_3}{\partial y'^2} + \upsilon_{\text{eff}} \dfrac{\partial^2 u_3}{\partial x'^2} \right)\Big|_{y'=0,b'} = 0. \end{cases} \tag{3.23}$$

Therefore, the transformation only affects the way how quantities get "measured" but does not change the system physically.

The resulting deformations manifest themselves as elastic waves. These waves are subject to the boundary conditions, Eqs. (3.23), and hence take the form $A_{mn} \sin\left(\frac{m\pi x}{a}\right) \sin\left(\frac{n\pi y}{b}\right)$, where A_{mn} is the wave amplitude, and m (n) denotes the number of half-waves propagating along the horizontal (vertical) direction. Because x and a (y and b) rescale in the same way, $m' = m$ ($n' = n$), i.e., the half-wave numbers are invariant in this case [cf. Eqs. (3.21)].

For an isotropic plate, the intensity of the load that gives rise to waves of a particular (m, n) is given in Ref. [9]:

$$\sigma_{\text{iso}}^{11} t = \frac{\pi^2 D}{b^2} \left(\frac{mb}{a} + n^2 \frac{a}{mb} \right)^2 . \tag{3.24}$$

The corresponding orthotropic stresses are hence

$$\sigma_{\text{ortho}}^{1'1'} t = \frac{\pi^2 D'}{b'^2} \left(\frac{mb'}{a'} + n^2 \frac{a'}{mb'} \right)^2 \tag{3.25, a}$$

$$\sigma_{\text{ortho}}^{11} t = \frac{\pi^2}{b^2} \left[D_1 \left(\frac{mb}{a} \right)^2 + 2D' n^2 + D_2 n^4 \left(\frac{a}{mb} \right)^2 \right], \tag{3.25, b}$$

which agrees with the known expression in the literature [9]. Its global minimum, with respect to the half-wave numbers, is the critical stress.[4]

In contrast to plates and singly-curved cylindrical shells with orthotropy, few exact results exist for the mechanical response of doubly-curved orthotropic shells. As a concrete application of our mapping, we next show that patches of orthotropic spheroidal shells transform locally to isotropic spheroidal shells with a different geometry, and use this mapping to derive new results for the indentation stiffness and buckling load of general orthotropic spheroidal shells.

3.3.4 Indentation Stiffness of Orthotropic Spheroidal Shells

3.3.4.1 The Zero-Pressure Case.

[4] If the real shear modulus G_{12} deviates much from the Huber form, to obtain the orthotropic stress, we can simply replace D' in Eq. (3.25, b) with $H = \frac{G_{12} t^3}{6} + D_1 \upsilon_{12}$, the real bending stiffness that penalizes twisting deformations (which reduces to D' when assuming the Huber form).

General Doubly-Curved Shells. For this simple case, $\sigma_0^{\alpha'\beta'} = 0$, and an extra term, $-F\delta(x^1)\delta(x^2)$, needs to be included on the right-hand side of Eq. (3.16, a) to model the concentrated load at the origin, where F denotes the load strength, and $\delta(x)$ is the Dirac delta function. Note that because of the scaling property of the delta function, $\delta(ax) = \frac{1}{|a|}\delta(x)$, the load strength does not need rescaling, i.e., $F\delta(x^1)\delta(x^2) = F\delta\left(x^{1'}\right)\delta\left(x^{2'}\right) \equiv F'\delta\left(x^{1'}\right)\delta\left(x^{2'}\right)$.

The indentation stiffness is defined as

$$k \coloneqq -\frac{F}{u_3(0,0)} = -\frac{F'}{u_{3'}(0,0)}, \tag{3.26}$$

where $u_3(0,0)$ is the transverse displacement of the shell at the origin in response to the indentation load. As shown in to Ref. [5], the inverse of the indentation stiffness at zero pressure is given by the following definite integral:

$$\frac{1}{k^0} = \frac{1}{4\pi^2}\int_{\mathbb{R}^2} \frac{Q\,\mathrm{d}Q\,\mathrm{d}\varphi}{D'Q^4 + Y'\left(\frac{1}{R_{2'}}\cos^2\varphi + \frac{1}{R_{1'}}\sin^2\varphi\right)^2}, \tag{3.27}$$

where the integration variables Q and φ are related to wavevectors, $\mathbf{q} = \left(q^{1'}, q^{2'}\right)$, in the following way: $q^{1'} = \frac{1}{\sqrt[4]{\lambda}}Q\cos\varphi$ and $q^{2'} = \sqrt[4]{\lambda}Q\sin\varphi$. The fact that $Q^2 = \sqrt{\lambda}\left(q^{1'}\right)^2 + \frac{1}{\sqrt{\lambda}}\left(q^{2'}\right)^2$ implicitly reflects that the metric of the rescaled Fourier space is non-Euclidean, resulting from the original material orthotropy.

Evaluating the integral in Eq. (3.27) gives

$$k^0 = 8\sqrt{D'Y'}\sqrt{K'} = \frac{4E_{\text{eff}}t^2}{\sqrt{3\left(1-\upsilon_{\text{eff}}^2\right)}}\frac{1}{\sqrt{R_1R_2}} = \frac{4\sqrt{E_1E_2}t^2}{\sqrt{3\left(1-\upsilon_{12}\upsilon_{21}\right)}}\frac{1}{\sqrt{R_1R_2}}. \tag{3.28}$$

Equation (3.28) clearly shows the separate contributions of geometry and material anisotropy to the indentation stiffness. As in the isotropic case, the Gaussian

curvature, $K = K' = 1/(R_1 R_2)$, is still the dominant geometrical quantity that governs shell stiffness at zero pressure [5, 72]. Heuristically, we could have anticipated this K dependence based on the fact that K is invariant under our rescaling transformation [Eq. (3.12)], and therefore captures the geometric rigidity independently of how the rescaling is performed.

Just as the geometric contribution is captured by the geometric mean of the two curvatures, effects of material anisotropy also come in the form of geometric mean, $E_{\text{eff}} = \sqrt{E_1 E_2}$ and $\upsilon_{\text{eff}} = \sqrt{\upsilon_{12}\upsilon_{21}}$. These geometric-mean dependences are consistent with the requirement of invariance of the indentation stiffness under coordinate transformations. Consider the equator of an orthotropic sphere. We call the local polar (meridional) and azimuthal (zonal) direction the first and the second direction, respectively, i.e., $\theta \equiv x^1$ and $\phi \equiv x^2$. Assume that the shell is strengthened along the first direction, i.e., $E_1 > E_2$. We now rotate our local coordinate system clockwise by ninety degrees, so that $x^1 \mapsto -x^2$, and $x^2 \mapsto x^1$. The rotation leaves us with the same spherical shell locally but with the second direction strengthened. We can infer two conclusions from this simple argument. First, any *local* elastic property around the equator of an orthotropic sphere should exhibit an exchange symmetry: Interchanging 1 and 2 does not make a difference. Second, if material anisotropy and geometry affect shell elasticity locally separately from one another, then for shells of *any* type, their local elastic properties should depend on combinations of elastic constants which are invariant under the interchange $1 \leftrightarrow 2$.

More generally, local elastic properties should be functions of invariant quantities constructed from the corresponding tensors. In our problem, such examples are furnished by the Gaussian curvature (the square root of the extrinsic curvature tensor's *determinant*) as well as the combination $\frac{1-\upsilon_{12}\upsilon_{21}}{E_1 E_2}$, which happens to be

the determinant of the stiffness matrix $C_{[\alpha\beta][\gamma\delta]}$ [Eq. (3.1)], if we assume that the deformation is axisymmetrical, i.e., ignoring G_{12}. We can to some extent rule out taking the trace of these tensors based on the fact that these traces are not invariant under the rescaling transformation, such as the local mean curvature [Eq. (3.13)].

For general ellipsoidal shells of revolution, material properties are usually different along the polar and azimuthal direction, which are also the principal directions of such shell surfaces [80]. Therefore, according to the shallow-shell theory, for these shells, Eq. (3.28) can be applied almost globally, except at the two poles, where the material-orthotropy pattern becomes curvilinear. Nevertheless, if we think of the local indentation stiffness as a function of positions on the shell surface and consider only small deformations, one can imagine that taking the analytical continuation of the function to the poles will imply that Eq. (3.28) can be still valid there. We will prove this claim in **Appendix D**.

Long Cylindrical Shells. As for their isotropic counterparts [5], the case of long orthotropic cylinders also requires special attention. Following the analysis by Yuan on isotropic cylinders [18], we apply the rescaling transformation and accordingly obtain the following expression for the zero-pressure stiffness of orthotropic cylinders (see **Appendix E** for details)

$$k^0_{\rm cyl}(\lambda) \approx \frac{1}{\sqrt[4]{\lambda}} \frac{2\pi}{3\sqrt{2}\,(1-\upsilon^2_{\rm eff})} \frac{E_{\rm eff} t^3}{R^2} \left(\sum_{n=1}^{\infty} \frac{1}{n^3} \frac{\sqrt{1+\Xi_n}}{\Xi_n} \right)^{-1}, \tag{3.29}$$

where $\Xi_n^2 \coloneqq 1 + \frac{3\left(1-\upsilon^2_{\rm eff}\right)}{4n^4} \left(\frac{R}{t}\right)^2$. The dependence of the stiffness expression on the cylinder's thickness and radius in the thin-shell limit ($R/t \gg 1$) is obtained by keeping the leading term of the series in Eq. (3.29), which dominates when $\frac{R}{t}$ is

sufficiently large:

$$k^0_{\text{cyl}}(\lambda) \approx \frac{1}{\sqrt[4]{\lambda}} \frac{2\pi}{3\sqrt{2}\left(1-\upsilon^2_{\text{eff}}\right)} \frac{E_{\text{eff}} t^3}{R^2} \sqrt{\Xi_1} \approx \frac{1}{\sqrt[4]{\lambda}} \frac{\pi}{\left[3\left(1-\upsilon^2_{\text{eff}}\right)\right]^{\frac{3}{4}}} \frac{E_{\text{eff}} t^{\frac{5}{2}}}{R^{\frac{3}{2}}}. \tag{3.30}$$

For isotropic ($\lambda = 1$) cylinders with a negligible Poisson's ratio ($\upsilon \approx 0$), Eq. (3.30) becomes

$$k^0_{\text{cyl}}(\lambda = 1) \approx 1.38 \frac{E t^{\frac{5}{2}}}{R^{\frac{3}{2}}}. \tag{3.31}$$

Equation (3.31) matches exactly, including the order-one prefactor, with the expression obtained by de Pablo et al. [3].

From Eq. (3.29), we observe that the zero-pressure indentation stiffness for long cylinders depends on the anisotropy parameter λ both implicitly (through the anisotropic elastic constants absorbed into E_{eff} and υ_{eff}) and explicitly (in the $1/\sqrt[4]{\lambda}$ factor), unlike the stiffness of orthotropic doubly-curved shells whose λ-dependence is purely implicit [see Eq. (3.28)]. The explicit λ-dependence breaks the aforementioned local exchange symmetry and is a consequence of the fact that open cylinders can deform isometrically (see **Section 3.3.4.2**).

Figure 3.3 illustrates the λ-dependence in the indentation stiffness of different types of shells in the absence of pressure. The $\tilde{k}$-axis denotes the nondimensionalized indentation stiffness. We used as our stiffness scale the zero-pressure stiffness of a corresponding isotropic shell with $\{E = E_1, \upsilon = \upsilon_{\text{eff}}, R = R_2\}$ (for spheroids, the chosen isotropic shell is a spherical shell with the same equatorial radius). This stiffness scale was chosen to show both the implicit and explicit λ-dependences as well as the dependence on Gaussian curvature for doubly-curved shells [Eq. (3.28)]. From the top inset of Fig. 3.3, we can see that the indentation stiffness of doubly-curved shells all scales as $\frac{1}{\sqrt{\lambda}}$, which shows the dependence on E_{eff} (since $E_{\text{eff}} = E_1/\sqrt{\lambda}$). On

the other hand, the stiffness of long cylinders has a λ-dependence given by $\frac{1}{\sqrt[4]{\lambda^3}}$; this is a combination of the same E_{eff} dependence and the explicit $\frac{1}{\sqrt[4]{\lambda}}$ factor in Eq. (3.29).

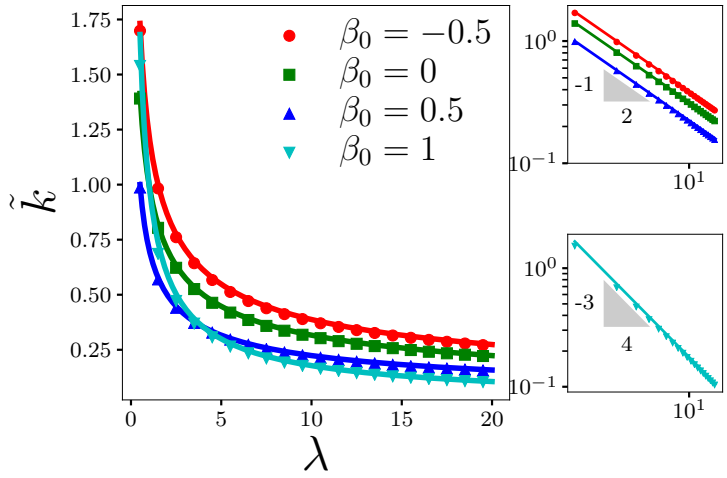

FIGURE 3.3. Zero-pressure indentation stiffness of four different types of orthotropic shells with varying values of the anisotropy parameter λ. Symbols denote data obtained from COMSOL simulation. Solid curves correspond to the analytical expressions Eqs. (3.28) and (3.30). For doubly-curved shells, $\beta_0 = 0, \pm 0.5$, their stiffness is scaled by $\frac{4E_1t^2}{\sqrt{3\left(1-\upsilon_{\text{eff}}^2\right)}}\frac{1}{R_2}$. On the other hand, the stiffness of cylinders, $\beta_0 = 1$, is scaled by $\frac{\pi}{\left[3\left(1-\upsilon_{\text{eff}}^2\right)\right]^{\frac{3}{4}}}\frac{E_1t^{\frac{5}{2}}}{R^{\frac{3}{2}}}$. The insets show the same data on double-log scale to demonstrate that the scaled stiffness of cylinders depends on λ differently from that of doubly-curved shells.

3.3.4.2 The Pressurized Case. We now consider the indentation stiffness of closed orthotropic shells subjected to a uniform pressure. This situation is relevant to biological shell-like structures, which often experience high turgor pressures; varying the pressure also provides a route to modifying the shape and stiffness of artificial shells [54, 81].

In the absence of indenting forces, the pressurized shell deforms from its original shape to attain a new equilibrium in which in-plane stresses balance the transverse loads due to the pressure. The indentation forces and deflections are then calculated

with reference to this prestressed state. For thin shells, the indentation response is still a local property of the geometry, elasticity, and prestresses in the vicinity of the indentation point, and a shallow-shell description of the local response will suffice to calculate the indentation stiffness. However, the prestressed state itself depends on the *global* shell shape—it is not determined solely by local properties [70]. For thin spheroidal and cylindrical orthotropic shells, these prestress configurations in response to a uniform pressure are known as a function of pressure and global geometry [9], and are independent of the elastic properties of the shell as long as the deformations in response to the pressure are small. We will use these prior results as inputs to our rescaled theory, which we then use to calculate the indentation stiffness as a function of geometry and pressure.

General Spheroids. Spheroids are ellipsoids of revolution. We are interested in the local indentation stiffness around a spheroid's equator. As in our previous work [5], we use $\beta_0 \coloneqq 1 - \frac{R_2}{R_1}$ to characterize the asphericity of a spheroid, where R_2 is the radius of its equator, and $\frac{1}{R_1}$ is the local principal curvature along the meridional direction for points on the equator. In the vicinity of the equator, the prestress components are given by $\sigma_0^{11}t = \frac{1}{2}pR_2$, $\sigma_0^{22}t = \frac{1}{2}pR_2(1+\beta_0)$ and $\sigma_0^{12}t = 0$ [9], where p denotes the uniform pressure to which the spheroid is subject.[5] The sign convention for the pressure is that a positive (negative) p means an internal (external) pressure.

Following the same procedure as the zero-pressure case, we obtain the inverse of the indentation stiffness which is now a function of three parameters, namely, the scaled pressure $\eta_{s,y}(\lambda) = \frac{pR_2^2}{4\sqrt{D'(\lambda)Y'(\lambda)}}$, the asphericity β_0 as well as the anisotropy

[5]We would like to mention that an orthotropic spheroid shares the same prestress as the corresponding isotropic one with the same geometry *only* on regions that are far away from the two poles [82, 83].

parameter λ *explicitly*

$$\begin{aligned}\frac{1}{k(\eta_{\mathrm{s},y}(\lambda),\beta_0,\lambda)} = \frac{1}{8\pi^2}\sqrt{\frac{R_{2'}^2}{D'Y'}}\int_0^{2\pi}\mathrm{d}\varphi\times \\ \times\int_0^{+\infty}\frac{\mathrm{d}u}{u^2+2\eta_{\mathrm{s},y}\left(1+\beta'_\lambda\sin^2\varphi\right)u+\left(1-\beta'\sin^2\varphi\right)^2},\end{aligned} \tag{3.32}$$

where $\beta' \coloneqq 1-\sqrt{\lambda}(1-\beta_0)$ and $\beta'_\lambda \coloneqq 2\sqrt{\lambda}-2+\beta'$ *appear* to couple the geometry and the material anisotropies. Nonetheless, it turns out that these explicit λ-dependences are *spurious*, as we will now demonstrate. The double integral in Eq. (3.32) can be evaluated in the following closed form (see **Appendix F** for details)

$$\begin{aligned}\frac{1}{k(\eta_{\mathrm{s},y}(\lambda),\beta_0)} = \frac{1}{2\pi}\sqrt{\frac{R_2^2}{D'Y'}}\frac{1}{\sqrt{1-\beta_0}}\frac{1}{\sqrt{(1-\eta_{\mathrm{s},y})(1+\alpha\eta_{\mathrm{s},y})}}\times \\ \times\mathrm{F}\left(\frac{1}{2}\arccos\eta_{\mathrm{s},y}\,\middle|-\frac{2(1-\alpha)\eta_{\mathrm{s},y}}{(1-\eta_{\mathrm{s},y})(1+\alpha\eta_{\mathrm{s},y})}\right),\end{aligned} \tag{3.33}$$

where $\alpha \coloneqq \frac{1+\beta'_\lambda}{1-\beta'} = \frac{1+\beta_0}{1-\beta_0}$ is independent of λ, and $\mathrm{F}\left(\vartheta\,|C^2\right)$ denotes the incomplete elliptic integral of the first kind:

$$\mathrm{F}\left(\vartheta\,\middle|C^2\right) \coloneqq \int_0^{\vartheta}\frac{\mathrm{d}\varphi}{\sqrt{1-C^2\sin^2\varphi}}. \tag{3.34}$$

Equation (3.33) is the primary result of this work: by applying the rescaling transformation, we have obtained a closed-form expression for the equatorial indentation stiffness of pressurized orthotropic spheroids, provided that the material anisotropy directions align with the latitudinal and longitudinal directions as shown in Fig. 3.1 (c). As a consistency check, setting $\beta_0 = 0$ ($R_1 = R_2 = R$) and $\lambda = 1$

($E_{\text{eff}} = E$ and $\upsilon_{\text{eff}} = \upsilon$) reduces Eq. (3.33) to, after taking the inverse,

$$k(\eta_{s,y}(1), 0) = \frac{2\pi\sqrt{DY}}{R} \frac{\sqrt{1-\eta^2}}{\mathrm{F}\left(\frac{1}{2}\arccos\eta \,|0\right)} = \frac{8\sqrt{DY}}{R} \frac{\sqrt{1-\eta^2}}{1-\frac{2}{\pi}\arcsin\eta}, \tag{3.35}$$

which recovers the established result of the indentation stiffness of pressurized isotropic spherical shells [14, 17].

Equation (3.33) demonstrates that the indentation stiffness depends on the anisotropy parameter λ only *implicitly* via the coupling constants $D' = \sqrt{D_1 D_2}$ and $Y' = E_{\text{eff}} t \equiv \sqrt{E_1 E_2}\, t$. In other words, the *only* effect of material anisotropy is modifying the elastic constants. As a consequence, our previous analysis on the behavior of the stiffness integral in different parameter regimes [5] should carry over to the orthotropic case. In particular, it was established in Ref. [5] that at high pressures, the geometry of the spheroid becomes less relevant. Instead, the indentation response is dominated by a new length scale—the *radius of distensile curvature*, defined as

$$\mathcal{R} \equiv \frac{1}{p}\sqrt{\det\left(\sigma_0^{\alpha\beta} t\right)}.$$

The indentation stiffness for arbitrary isotropic ellipsoids at high pressure approaches that of a sphere of radius $\mathcal{R}$ experiencing a non-dimensionalized pressure $\eta_{\mathcal{R}} \equiv p\mathcal{R}^2/(4\sqrt{DY})$. For anisotropic spheroids, we expect the same behavior provided the geometric-mean coupling constants D' and Y' are used in the rescaling. This expectation is confirmed in Fig. 3.4, which reports simulation data and theoretical predictions for the indentation stiffness of pressurized shells as a function of pressure over a range of geometry and anisotropy values. The data have been nondimensionalized using scales related to the radius of distensile curvature.

Theoretical curves and simulation data for different shell geometries converge in the limit $\eta_{\mathcal{R}} \gg 1$, mirroring the behavior of isotropic shells reported in Fig. 3 of Ref. [5].

Long Cylindrical Shells. It is possible to attain the indentation stiffness of long pressurized cylinders directly from Eq. (3.33) by taking the limit $\beta_0 \to 1^-$ and invoking the L'Hôpital's rule repeatedly. As a more direct approach, we first impose that limit in Eq. (3.32) and then evaluate the resulting definite integral. By doing so, we get, after some calculations (see **Appendix F**),

$$\begin{aligned} \frac{1}{k(\eta_{\mathrm{s},y}(\lambda),1)} \equiv \frac{1}{k_{\mathrm{cyl}}(\eta_{\mathrm{s},y}(\lambda))} &= \frac{1}{4\pi}\sqrt{\frac{R^2}{D'Y'}}\frac{1}{\sqrt{\eta_{\mathrm{s},y}}}\int_0^{+\infty}\frac{\mathrm{d}x}{\sqrt{x^4+2\eta_{\mathrm{s},y}x^2+1}} \\ &= \frac{1}{4\pi}\sqrt{\frac{R^2}{D'Y'}}\frac{1}{\sqrt{\eta_{\mathrm{s},y}}}\mathrm{K}\left(\frac{1}{2}(1-\eta_{\mathrm{s},y})\right), \end{aligned} \tag{3.36}$$

where $R \equiv R_2$ is the radius of cylinders, and $\mathrm{K}\left(C^2\right)$ denotes the complete elliptic integral of the first kind:

$$\mathrm{K}\left(C^2\right) \coloneqq \mathrm{F}\left(\frac{\pi}{2}\middle|C^2\right) = \int_0^{\frac{\pi}{2}}\frac{\mathrm{d}\varphi}{\sqrt{1-C^2\sin^2\varphi}}. \tag{3.37}$$

The fact that $\mathrm{K}\left(C^2\right)$ is analytic for $|C| < 1$ indicates that when $0 < \eta_{\mathrm{s},y} \ll 1$, $k_{\mathrm{cyl}}(\eta_{\mathrm{s},y}(\lambda)) \propto \sqrt{\eta_{\mathrm{s},y}}$ for orthotropic cylinders, just like their isotropic counterparts [5].

We here provide an explanation for the physical origin of the square-root dependence on pressure. It comes from the fact that an open cylindrical shell can bend or flatten without stretching [7]. This can be seen qualitatively as follows; for the sake of simplicity, we will first consider the isotropic case (setting $\lambda = 1$) and hence temporarily drop the primes. For cylinders under an inextensible deformation, $\frac{D}{R^3}$, instead of $\frac{4\sqrt{DY}}{R^2}$, is the more appropriate pressure scale since it does not contain

the two-dimensional Young's modulus which penalizes stretching. We can therefore write pressure in this case as $p = C_p \frac{D}{R^3}$ with C_p some pressure-dependent constant and

$$\eta_{\mathrm{s},y} \coloneqq \frac{pR^2}{4\sqrt{DY}} = \frac{1}{4\sqrt{\gamma}} \frac{pR^3}{D} = \frac{C_p}{4\sqrt{\gamma}}, \tag{3.38}$$

where γ denotes the Föppl-von Kármán number: $\gamma \coloneqq \frac{YR^2}{D} \simeq 10\left(\frac{R}{t}\right)^2 \gg 1$. Substituting Eq. (3.38) into Eq. (3.36), we find, after taking the inverse,

$$k_{\mathrm{cyl}}(\eta_{\mathrm{s},y}) \propto \sqrt{C_p} \frac{Et^{\frac{5}{2}}}{R^{\frac{3}{2}}} \tag{3.39}$$

for low pressures [$\eta_{\mathrm{s},y} \ll 1$, so that $\mathrm{K}\left(\frac{1}{2}(1-\eta_{\mathrm{s},y})\right) \approx \mathrm{K}\left(\frac{1}{2}\right)$]. The characteristic dependence on t and R is the very consequence of an inextensible deformation [cf. Eq. (3.30)] [3].

We can utilize the same approach to demonstrate that the stiffness of orthotropic cylindrical shells depends on λ explicitly at low pressures, and moreover, this explicit λ-dependence is indeed given by $\frac{1}{\sqrt[4]{\lambda}}$, as shown in Eq. (3.29). For an orthotropic cylinder, the pressure scale which corresponds to a flattening of the surface is $\frac{D_\theta}{R^3}$ [see Eq. (3.22)]. We then write $p = C_p \frac{D_\theta}{R^3}$ and

$$\eta_{\mathrm{s},y} \coloneqq \frac{pR^2}{4\sqrt{D'Y'}} = \frac{1}{4\sqrt{\gamma_{\mathrm{eff}}}} \frac{pR^3}{D'} = \frac{D_\theta}{D'} \frac{C_p}{4\sqrt{\gamma_{\mathrm{eff}}}} = \frac{1}{\sqrt{\lambda}} \frac{C_p}{4\sqrt{\gamma_{\mathrm{eff}}}} \tag{3.40}$$

with $\gamma_{\mathrm{eff}} \coloneqq \frac{Y'R^2}{D'}$. It follows that after substitution,

$$k_{\mathrm{cyl}}(\eta_{\mathrm{s},y}(\lambda), \lambda) \propto \frac{1}{\sqrt[4]{\lambda}} \sqrt{C_p} \frac{E_{\mathrm{eff}} t^{\frac{5}{2}}}{R^{\frac{3}{2}}}. \tag{3.41}$$

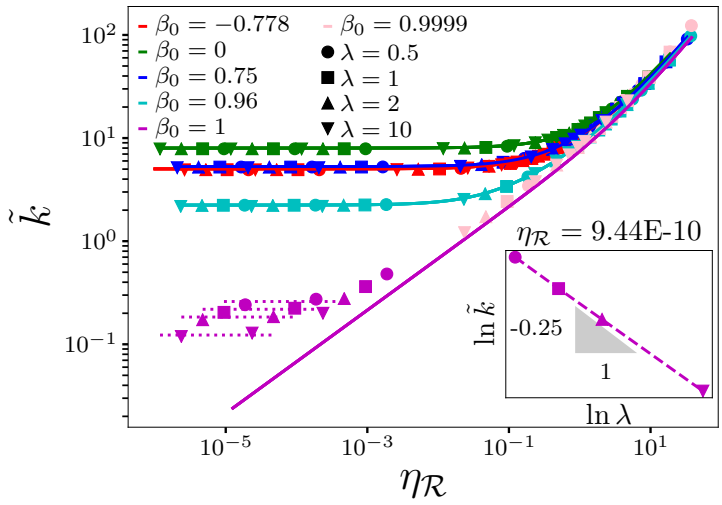

FIGURE 3.4. Indentation stiffness of orthotropic shells of five different geometries (β_0's) and four degrees of anisotropy (λ's) as a function of pressure. Symbols denote data obtained from `COMSOL` simulation. Solid curves correspond to the analytical expression Eq. (3.33). Data are scaled using the stiffness scale $\sqrt{\frac{D'Y'}{R_2^2(1+\beta_0)}}$ and the pressure scale $\frac{4\sqrt{D'Y'}}{R_2^2(1+\beta_0)}$ to match FIG. 3 in Ref. [5].

3.3.5 Buckling Load of Orthotropic Spheroids under Uniform Pressure

3.3.5.1 General Spheroids.

External Buckling Pressure. When a curved shell buckles under a uniform pressure, it also becomes locally soft, i.e., its indentation stiffness vanishes, because of the emergence of an unstable mode, for which the integral in Eq. (3.32) diverges [5]. We can then obtain the *local* buckling pressure around the equator of such shells by studying the zeros of $k\big(\eta_{s,y}(\lambda), \beta_0\big)$ for a given β_0. We can read off the zeros directly

from Eq. (3.33) and hence acquire the nondimensionalized buckling pressure:

$$\eta_{\mathrm{c}} = \begin{cases} -1, & \text{for the oblate } (\beta_0 \leq 0), \\ -\dfrac{1-\beta_0}{1+\beta_0}, & \text{for the prolate } (\beta_0 > 0). \end{cases} \tag{3.42, a}$$

Recall that the pressure scale used in Eq. (3.33) is $p_{\mathrm{sc}} \coloneqq \frac{4\sqrt{D'Y'}}{R_2^2}$. The dimensionful buckling pressure is thus

$$p_{\mathrm{c}} \coloneqq \eta_{\mathrm{c}} p_{\mathrm{sc}} = \begin{cases} -\dfrac{4\sqrt{D'Y'}}{R_2^2}, & \text{for } \beta_0 \leq 0, \\ -\dfrac{4\sqrt{D'Y'}}{2R_1R_2 - R_2^2}, & \text{for } \beta_0 > 0. \end{cases} \tag{3.42, b}$$

As was the case with the indentation stiffness expression, the local buckling pressure of orthotropic spheroids (both prolate and oblate) is exactly that of the corresponding isotropic shells [5] with the same geometry and with geometric-mean elastic constants taking the place of the isotropic elasticity parameters. This fact again shows that that the main effect of material anisotropy is to modify the elastic constants; the geometric contribution (radius dependence of the buckling pressure) is not affected. Our result is consistent with the established expression for the buckling pressure of spheroidal shells stiffened by reinforcements along the equatorial or longitudinal directions, which was also founded on the shallow-shell theory [69].

As a special case, the local buckling pressure of an orthotropic sphere around its equator is given by setting $\beta_0 = 0$ above:

$$p_{\mathrm{c,\ sph}} = -\frac{4\sqrt{D'Y'}}{R^2}. \tag{3.43}$$

The buckling of orthotropic spheres was investigated computationally and experimentally in Ref. [54]. In that work, it was found that upon increasing the external pressure on an orthotropic sphere with material anisotropy aligned to the polar and azimuthal directions, buckling first occurred in the vicinity of the equator when $\lambda \geq 1$ (i.e., when the stiffness E_1 along the polar direction is greater than the stiffness E_2 along the azimuthal direction). Consequently, our expression for the local buckling pressure at the equator provides a prediction for the *global* buckling pressure when $\lambda > 1$.

We compared our theoretical result against simulation results for the buckling load of orthotropic spherical shells with $\lambda > 1$, which were generated following the computational approach reported in Ref. [54] (see **Appendix H** for details). To isolate the explicit dependence of the buckling pressure on the anisotropy parameter, theory and simulation values were rescaled by the classical buckling pressure of an isotropic sphere with the same radius and elastic parameters $\{E_1, \upsilon_{12}\}$:

$$p_{\text{sc}}^{\text{M}} \coloneqq -\frac{2E_1}{\sqrt{3\left(1-\upsilon_{12}^2\right)}}\left(\frac{t}{R}\right)^2. \tag{3.44}$$

Using this pressure scale, the rescaled prediction for the buckling pressure of spheres with $\lambda > 1$ is

$$\eta_{\text{c, sph}}^{\text{M}} \coloneqq \frac{p_{\text{c, sph}}}{p_{\text{sc}}^{\text{M}}} = \frac{1}{\sqrt{0.91\lambda}}\sqrt{1-\frac{0.09}{\lambda}}, \tag{3.45}$$

which is plotted as a solid line in Fig. 3.5. We found that upon subtracting a constant offset of 0.0738, the theoretical result successfully captures the dependence of the buckling pressure on the anisotropy parameter. The constant offset is well within the expected deviation between theory and simulations due to factors such as imperfection sensitivity. Reference [54] also reported buckling pressures for

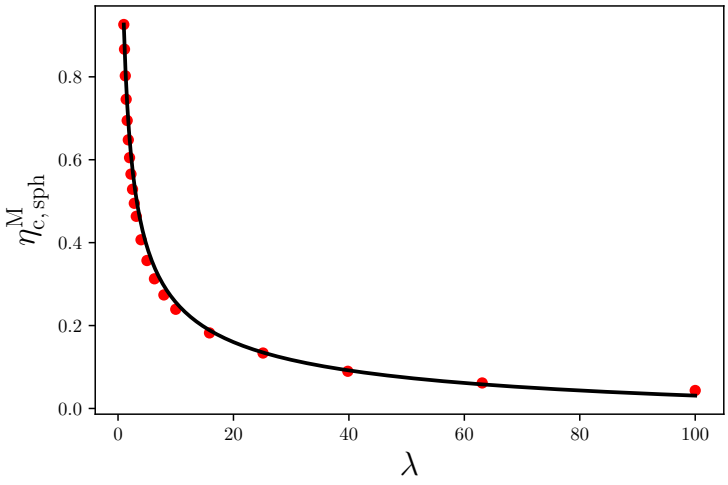

FIGURE 3.5. The scaled global buckling pressure of orthotropic spheres as a function of the degree of material anisotropy. The spheres considered here have a larger Young's modulus along the polar direction, i.e., $\lambda \geq 1$ ($E_1 \geq E_2$). Symbols denote finite element simulation data (see **Appendix H** for details). The solid curve corresponds to the analytical result Eq. (3.45) subtracting a constant offset of 0.0738. The inset shows the buckling mode along the equator.

orthotropic spherical shells with $\lambda < 1$, for which buckling was observed to first occur near the two poles where the type of orthotropy is not rectilinear but polar. The rescaling transformation does not apply to this form of anisotropy, so we cannot predict the global buckling pressure in this parameter region using our approach.

Internal Buckling Pressure. In our previous work [5], we demonstrated qualitatively that because of the sign switch of the prestress component σ_0^{22} $[= \frac{1}{2}pR_2\,(1+\beta_0)]$ at $\beta_0 = -1$, it is possible for a highly oblate spheroidal shell with $\beta_0 < -1$ to buckle under an internal pressure ($p, \eta_{\mathrm{s},y} > 0$) due to compressive stresses along its equator. Using Eq. (3.33), we are able to identify that pressure exactly. For $\beta_0 < -1$ ($\alpha < 0$) and $\eta_{\mathrm{s},y} > 0$, the function $k\big(\eta_{\mathrm{s},y}(\lambda), \beta_0\big)$ vanishes when $1 + \alpha\eta_{\mathrm{s},y} = 0$, or equivalently,

$$\eta_{\mathrm{s},y} = \eta_{\mathrm{c}}^{\mathrm{int}} \coloneqq -\frac{1}{\alpha} = \frac{1-\beta_0}{|1+\beta_0|} > 0. \tag{3.46, a}$$

(This is roughly because $\lim_{x\to+\infty} \left|\sqrt{x}\,\mathrm{F}\left(\vartheta\,|x\right)\right| = +\infty$.) Restoring the physical units gives

$$p_{\mathrm{c}}^{\mathrm{int}} = \frac{4\sqrt{D'Y'}}{R_2^2 - 2R_1R_2} \tag{3.46, b}$$

[cf. Eqs. (3.42)]. Equations (3.46) are consistent with the results by Tovstik and Smirnov on isotropic spheroids [84], and yet again show that the orthotropic shell response is dictated by replacing the isotropic elastic constants with their geometric-mean counterparts D' and Y'.

3.4 Discussions

We established that under a particular coordinate transformation [Eq. (3.7)], which we termed the rescaling transformation, an orthotropic shallow shell can be treated locally as an isotropic one of a different geometry. The main idea behind the rescaling transformation–hiding anisotropy by rescaling the coordinate system used–is also seen in other contexts, e.g., the anisotropic XY-model [85]. The rescaling transformation enabled us to obtain analytically local mechanical properties of orthotropic spheroidal and cylindrical shells, such as their buckling load [Eqs. (3.42), (3.19) and (3.22)] and indentation stiffness [Eqs. (3.33) and (3.30)], directly from using the corresponding isotropic results. Besides its mathematical convenience, the transformation also helped to quantify the separate effects of geometry and material anisotropy on these local mechanical properties. We demonstrated that when the principal directions of curvature and material anisotropy are aligned, the two effects are decoupled. In light of this, an orthotropic shell can have the same local mechanical properties as an isotropic one as long as they have the same local geometry. This rationalizes why it is valid to use GMI (geometric-mean isotropic) materials as an approximation of real orthotropic materials in certain cases [76].

Effects of geometry on local mechanical properties were studied in detail in our previous work [5]. Effects of material anisotropy differ depending on whether or not the deformation considered is localized. In the case of a localized deformation, the anisotropic elastic constants combine in the form of geometrical mean; the resulting combinations serve the role of effective isotropic elastic constants. If the deformation is not localized, like the case of indenting a cylinder at zero pressure, besides the aforementioned effect, local mechanical properties can also depend on other dimensionless combinations of the anisotropic elastic constants, such as their ratio [see Eq. (3.30)]. In such cases, it would be wrong to use GMI materials to approximate real orthotropic materials.

We assumed throughout this paper that the orthotropic in-plane shear modulus (denoted by G_{12}) is given by the Huber form [G_{H} given by Eq. (3.4)]. Our work provides theoretical insight on why this type of orthotropic materials can have isotropic behaviors, e.g., why they do not exhibit tristability [57]. We envision that our rescaling transformation can still be useful in studies of shells made of general orthotropic materials: In these cases, G_{12} is in general a free parameter, and a torsion-like term with coupling constant $G_{12} - G_{\mathrm{H}}$ needs to be added into the governing equations.

Our work also points to a couple of directions for future investigations. First, for spheroidal shells, the rescaling transformation can actually only be applied at their equator where the axes of curvature and material anisotropy perfectly coincide. At other locations, there will be some angle between the two sets of axes, and we hence expect that the effects of geometry and material anisotropy can couple together at these locations, making a shell locally stronger. We image that studying this more general case can be useful for structural design. Furthermore, we note that at the

poles, material orthotropy becomes curvilinear. The rescaling transformation does not apply in this case because of the complicated form that the biharmonic operator takes in polar coordinates [50]. It remains an open question what the buckling pressure and indentation stiffness of shells of curvilinear orthotropy are. Knowing these can shed some light on morphogenesis [54], such as the reason why an apple develops a cusp [86].

CHAPTER IV

CONCLUSION

In this final chapter, I summarize the key results obtained in the previous two chapters and point out some research directions for future investigations.

4.1 Summary

4.1.1 Indentation Stiffness of Isotropic Spheroidal and Cylindrical Shells

We solved the nonlinear shallow-shell equations using Fourier transform. The indentation stiffness was characterized by a Fourier integral termed the stiffness integral. Instead of exactly carrying out the stiffness integral, which was done in **Chapter III**, we here evaluated it in different limits.

4.1.1.1 General Spheroids ($-1 \leq \beta < 1$). For a general spheroidal shell, the stiffness integral was found to diverge at a particular external pressure, which is the spheroid's local buckling pressure (denoted by p_c). Near and below the buckling pressure ($|p| < |p_c|$), the stiffness integral diverges logarithmically for non-spheres ($\beta \neq 0$), while in the spherical limit, this becomes a power-law divergence.

At low internal pressures, the actual stiffness (the inverse of the stiffness integral) was found to be proportional to $\sqrt{K}$, where K is the spheroid's local Gaussian curvature. Since $K = \frac{1-\beta}{R_y^2}$, a spheroidal shell with a smaller β is locally stiffer (with R_y fixed). However, this does not hold true in the high-pressure limit. We found that the relevant geometric quantity in this case is the distensile curvature radius $\mathcal{R} \coloneqq \frac{1}{p}\sqrt{\det\{\boldsymbol{\sigma}\}} = R_y\sqrt{1+\beta}$. This implies exactly the opposite of the low-pressure

case: it is now a shell with a larger β that is locally stiffer. This contrast in the two limits predicts a phenomenon called the stiffness switching that between two shells, the shell which is locally softer in the low-pressure limit will become the stiffer one when getting highly pressurized.

4.1.1.2 Long Cylinders ($\beta = 1$). While the stiffness integral diverges when $p \leq 0$, this does not mean that the buckling pressure of a long cylindrical shell is zero. In fact, it is known that its buckling pressure is given by $p_c = -\frac{3D}{R^3}$ [9], which is identical to that of a ring with the same radius. The problem here is that the way we solved the shallow-shell equations—using the double Fourier transform—failed to capture the long-wavelength isometric deformation of the cylindrical shell. We fixed this issue in **Chapter III** using the approach by Yuan [18].

For finite internal pressures, deformations of the cylinder become localized and hence non-isometric. We derived a pressure range for which using the double Fourier transform is appropriate and further showed that the stiffness of the cylinder scales as $\sqrt{p}$ when the internal pressure within that range is low. At high pressures, the result in **Section 4.1.1.1** applies; in fact, according to the stiffness switching, the cylinder will be stiffer than any spheroidal shell after certain pressure.

4.1.2 The Rescaling Transformation and Indentation Stiffness of Orthotropic Shells

We found that by rescaling the coordinates, the generalized Hooke's law for an orthotropic elastic material takes the isotropic form. We termed the corresponding coordinate transformation the rescaling transformation. The rescaling transformation reveals the fact that even though having less symmetry, an

orthotropic material can behave as an isotropic material if we choose to measure physical quantities along the two orthotropic directions in a different way.[1] The principle underlying the rescaling transformation—mapping an anisotropic system to an isotropic one by rescaling the coordinate system used—has also been seen in other contexts, e.g., the anisotropic XY-model [85].

We derived the indentation stiffness and buckling pressure of rectilinearly orthotropic spheroidal and cylindrical shells by using the rescaling transformation on the corresponding known isotropic results. We found that in the case where the deformation considered is localized (so that the double Fourier transform can be used), an orthotropic shell behaves exactly as its isotropic counterpart, and so the discussions in **Section 4.1.1** on indentation stiffness in different limits still apply. The only effect of material orthotropy in this case is that the orthotropic elastic constants combine in the form of geometric mean to serve as the effective isotropic constants. On the other hand, in the case of long-wavelength deformations, such as indentation response of long cylinders at low pressures, besides the aforementioned effect, local mechanical properties of an orthotropic shell can also depend on some dimensionless combination of the orthotropic elastic constants, e.g., their ratio.

What is more, as previously mentioned, we exactly evaluated the stiffness integral. The exact expression makes it easy to obtain the local buckling pressure of spheroidal shells and clearly shows that shells with $\beta < -1$ can buckle under an internal pressure.

[1]Physically, rescaling the coordinates is like using a different set of units for measurements.

4.2 Research Outlook

4.2.1 Isotropic Shells

4.2.1.1 General Ellipsoidal Shells. A low-hanging fruit is studying the indentation stiffness of a general triaxial ellipsoidal shell made of an isotropic material. Using the known prestresses derived in Ref. [34], one can obtain a stiffness integral that is similar to the one in Eq. (3.32). From the integral, one can compute indentation stiffness and further obtain the shell's local buckling pressure.

4.2.1.2 Relevant Geometric Quantity for Large Deformations. Recall that we have established that at low pressures, it is a shell's local Gaussian curvature that governs its indentation stiffness. However, this result assumes a linear relation between force and displacement, which is valid only when the displacement due to an applied force is much smaller than the shell thickness. Therefore, it remains an open question whether Gaussian curvature is still the relevant geometric quantity in the case of large deformations. One promising way to solve the problem is, again, to rescale coordinates, so that the Vlasov operators in Eqs. (2.16) become Laplacian operators in the rescaled coordinate system, and then apply the argument in Ref. [14] for spheres.

4.2.2 Orthotropic Shells

4.2.2.1 Curvilinear Orthotropy. The rescaling transformation found previously only holds in the case of rectilinear orthotropy and hence does not apply to curvilinearly orthotropic shells, e.g., region around the poles of an orthotropic

spheroid. Nevertheless, we were still able to obtain their indentation stiffness in the absence of pressure by solving the linearized axisymmetric shallow-shell equations.

The situation becomes complicated when pressure is introduced. As Reissner has demonstrated [83], stress within a pressurized curvilinearly orthotropic shell has the power-law behavior $r^{-1+\frac{1}{\sqrt{\lambda}}}$, where r measures the distance away from the center of the shell. In particular, the stress at the center ($r = 0$) will either vanish ($\lambda < 1$) or diverge ($\lambda > 1$).

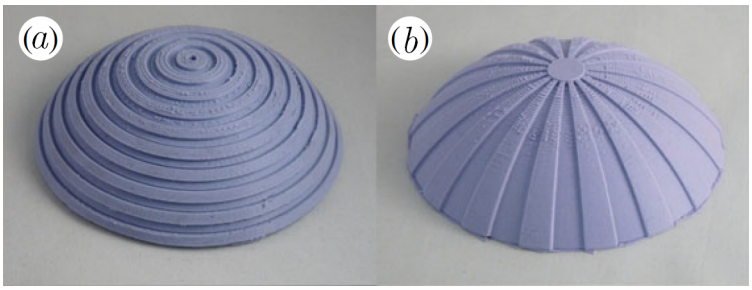

FIGURE 4.1. Spherical caps having polar orthotropy. Figure (a) shows a circumferentially stiffened shell ($\lambda < 1$); (b) a radially stiffened shell ($\lambda > 1$).
Image credits: Reference [6].

For large internal stresses, this behavior cannot be captured by linear theory which does not distinguish between the two cases[2]. The breakdown of linear theory makes it challenging to derive indentation stiffness and buckling pressure of shells of this type. At present, only numerical solutions are known [54].

Steele and Fartung [82] developed a deep-shell theory to study these shells. They were able to get solutions which describe deformation of these shells under a uniform pressure. It is possible to linearize the nonlinear shell equations around the deformation state obtained by them and derive the indentation stiffness and buckling pressure by analysing the resulting linearized equation. We expect techniques of asymptotic analysis [87] to be used.

[2]In the low-pressure regime, linear theory does give a good prediction.

4.2.2.2 More General Cases of Rectilinear Orthotropy.

While our rescaling transformation relies on the use of Huber form G_{H} for in-plane shear modulus G_{12}, this does not mean that it cannot be applied to study cases where $G_{12} \neq G_{\mathrm{H}}$. In these more general cases, a torsion-like term with coupling constant given by the difference $G_{12} - G_{\mathrm{H}}$ needs to be added in the governing equilibrium equations. In more physical terms, a general orthotropic shell can be treated as a *pre-twisted* isotropic shell with a different local geometry; strength of the torsion is related to how large the difference $|G_{12} - G_{\mathrm{H}}|$ is.

The case where the principal axes of curvature and material orthotropy are misaligned is a little paradoxical, for the following reason, and needs to be investigated. On one hand, we, based on intuition, expect that effects of geometry and material orthotropy can couple together because of the misalignment. On the other hand, our previous results that indentation stiffness only depends on coordinate-independent quantities (e.g., Gaussian curvature K, distensile radius $\mathcal{R}$ and determinant of the stiffness matrix $\mathbf{C}$) imply the opposite: the misalignment should have no effect on local mechanical properties at all. To resolve the disagreement, one way is to use the material coordinates, which correspond to the material principal axes. In this coordinate system, extrinsic curvature tensor and prestress tensor are not diagonal; their off-diagonal components will act like the coupling constant of a second torsion-like term in the equilibrium equations. We can understand the true effect of the misalignment by adding this term and studying the resulting stiffness integral.

APPENDIX A

DIFFERENTIAL GEOMETRY DESCRIPTION FOR SHELLS

A.1 Geometry of a shell's middle surface

Let $\mathcal{M}$ denote the middle surface of a shell. We choose to locally parametrize $\mathcal{M}$ using coordinates corresponding to lines of principal curvature (denoted by x^α). Since these lines are orthogonal, their tangent vectors at any arbitrary point $P \in \mathcal{M}$ are also orthogonal: if $\alpha \neq \beta$,

$$\left\langle \left.\frac{\boldsymbol{\partial}}{\boldsymbol{\partial} x^\alpha}\right|_P , \left.\frac{\boldsymbol{\partial}}{\boldsymbol{\partial} x^\beta}\right|_P \right\rangle = 0. \tag{A.1}$$

This means that the induced metric on $\mathcal{M}$ takes the diagonal form in this coordinate system:

$$\mathbf{a} = a_{\alpha\beta}\, \mathrm{d}x^\alpha \otimes \mathrm{d}x^\beta = a_{11}\, \mathrm{d}x^1 \otimes \mathrm{d}x^1 + a_{22}\, \mathrm{d}x^2 \otimes \mathrm{d}x^2. \tag{A.2}$$

Defining the one-forms $\tilde{\boldsymbol{\phi}}^\alpha \coloneqq \sqrt{a_{\alpha\alpha}}\, \mathrm{d}x^\alpha$ (no Einstein summation convention), we can rewrite the metric as

$$\mathbf{a} = \tilde{\boldsymbol{\phi}}^1 \otimes \tilde{\boldsymbol{\phi}}^1 + \tilde{\boldsymbol{\phi}}^2 \otimes \tilde{\boldsymbol{\phi}}^2 = \delta_{\alpha\beta}\, \tilde{\boldsymbol{\phi}}^\alpha \otimes \tilde{\boldsymbol{\phi}}^\beta, \tag{A.3}$$

where $\delta_{\alpha\beta}$ is the Kronecker delta symbol. The second fundamental form of $\mathcal{M}$ also takes the diagonal form in the coordinates (x^α) and can be written as

$$\begin{aligned}\mathbf{b} = b_{\alpha\beta}\,\mathrm{d}x^\alpha \otimes \mathrm{d}x^\beta &= b_{11}\,\mathrm{d}x^1 \otimes \mathrm{d}x^1 + b_{22}\,\mathrm{d}x^2 \otimes \mathrm{d}x^2 \\ &= \frac{b_{11}}{a_{11}}\,\tilde{\boldsymbol{\phi}}^1 \otimes \tilde{\boldsymbol{\phi}}^1 + \frac{b_{22}}{a_{22}}\,\tilde{\boldsymbol{\phi}}^2 \otimes \tilde{\boldsymbol{\phi}}^2 \\ &\equiv \kappa_1\,\tilde{\boldsymbol{\phi}}^1 \otimes \tilde{\boldsymbol{\phi}}^1 + \kappa_2\,\tilde{\boldsymbol{\phi}}^2 \otimes \tilde{\boldsymbol{\phi}}^2,\end{aligned} \tag{A.4}$$

where κ_α denotes the principal curvatures of $\mathcal{M}$.

A.2 Geometry of the entire shell

The outward unit normal vectors $\hat{\mathbf{n}}$ of the middle surface $\mathcal{M}$ are given by

$$\hat{\mathbf{n}} = \frac{\dfrac{\boldsymbol{\partial}}{\boldsymbol{\partial} x^1} \times \dfrac{\boldsymbol{\partial}}{\boldsymbol{\partial} x^2}}{\left\| \dfrac{\boldsymbol{\partial}}{\boldsymbol{\partial} x^1} \times \dfrac{\boldsymbol{\partial}}{\boldsymbol{\partial} x^2} \right\|}. \tag{A.5}$$

Let $\mathcal{S}$ denote the three-dimensional solid shell and h the shell thickness. We can use the orthogonal coordinates $(x^i) \equiv (x^\alpha, z)$ to parametrize $\mathcal{S}$; the new coordinate $z \in \left[-\frac{h}{2}, \frac{h}{2}\right]$ measures the distance along the $\hat{\mathbf{n}}$-direction away from the shell middle surface, at which $z = 0$.

The metric on $\mathcal{S}$ still takes the diagonal form in this coordinate system:

$$\begin{aligned}\mathbf{g} = g_{ij}\,\mathrm{d}x^i \otimes \mathrm{d}x^j &= g_{11}\,\mathrm{d}x^1 \otimes \mathrm{d}x^1 + g_{22}\,\mathrm{d}x^2 \otimes \mathrm{d}x^2 + g_{33}\,\mathrm{d}x^3 \otimes \mathrm{d}x^3 \\ &= a_{11}(1 + z\kappa_1)^2\,\mathrm{d}x^1 \otimes \mathrm{d}x^1 + a_{22}(1 + z\kappa_2)^2\,\mathrm{d}x^2 \otimes \mathrm{d}x^2 + \mathrm{d}x^3 \otimes \mathrm{d}x^3.\end{aligned} \tag{A.6}$$

Notice that $\mathbf{g}(x^3 = 0) = \mathbf{a}$. The rest of the section is devoted to show Eq. (A.6).

A.2.1 Proving Eq. (A.6)*.*

A.2.1.1 A Pedagogical Approach. We first use a pedagogical approach. Let $\mathbf{X}(x^\alpha)$ denote a parametrization of the shell middle surface $\mathcal{M}$. Then $\mathcal{S}$ can be parametrized as

$$\mathbf{Y}(x^i) = \mathbf{X}(x^\alpha) + z\,\hat{\mathbf{n}}(x^\alpha). \tag{A.7}$$

We can compute the components of the metric $\mathbf{g}$ using

$$g_{ij} = \mathbf{g}\left(\frac{\boldsymbol{\partial}}{\boldsymbol{\partial} x^i}, \frac{\boldsymbol{\partial}}{\boldsymbol{\partial} x^j}\right) \equiv \mathbf{g}\left(\frac{\partial \mathbf{Y}}{\partial x^i}, \frac{\partial \mathbf{Y}}{\partial x^j}\right) = \left\langle \frac{\partial \mathbf{Y}}{\partial x^i}, \frac{\partial \mathbf{Y}}{\partial x^j} \right\rangle. \tag{A.8}$$

We have

$$g_{33} = \left\langle \frac{\partial \mathbf{Y}}{\partial z}, \frac{\partial \mathbf{Y}}{\partial z} \right\rangle = \|\hat{\mathbf{n}}\|^2 = 1 \tag{A.9}$$

and

$$\begin{aligned} g_{\alpha\alpha} = \left\langle \frac{\partial \mathbf{Y}}{\partial x^\alpha}, \frac{\partial \mathbf{Y}}{\partial x^\alpha} \right\rangle &= \left\langle \frac{\partial \mathbf{X}}{\partial x^\alpha} + z\frac{\partial \hat{\mathbf{n}}}{\partial x^\alpha}, \frac{\partial \mathbf{X}}{\partial x^\alpha} + z\frac{\partial \hat{\mathbf{n}}}{\partial x^\alpha} \right\rangle \\ &= \left\| \frac{\partial \mathbf{X}}{\partial x^\alpha} \right\|^2 + z^2 \left\| \frac{\partial \hat{\mathbf{n}}}{\partial x^\alpha} \right\|^2 + 2z \left\langle \frac{\partial \mathbf{X}}{\partial x^\alpha}, \frac{\partial \hat{\mathbf{n}}}{\partial x^\alpha} \right\rangle \end{aligned} \tag{A.10}$$

(no Einstein summation convention). The first term in Eq. (A.10) is just $a_{\alpha\alpha}$. To understand what the other two terms mean, let us first review the concept of shape operator.

Shape operator. The shape operator $\mathscr{S}$ at a point $P \in \mathcal{M}$ is a linear map on the tangent space at P, $\mathscr{S}_P : T_P\mathcal{M} \to T_P\mathcal{M}$, which is given by

$$\mathscr{S}_P(\mathbf{V}) = -\,\boldsymbol{\nabla}_{\mathbf{V}}\,\hat{\mathbf{n}}|_P \equiv -\,V^\alpha \frac{\partial \hat{\mathbf{n}}}{\partial x^\alpha}\bigg|_P. \tag{A.11}$$

The second fundamental form $\mathbf{b}$ is defined in terms of $\mathscr{S}$ as follows:

$$\mathbf{b}(\cdot,\cdot) \coloneqq \langle \cdot, \mathscr{S}(\cdot) \rangle \,. \tag{A.12}$$

Since $\mathscr{S}$ maps a vector to a vector in the same tangent space, it is a $\binom{1}{1}$-tensor field:

$$\mathscr{S} = b_\alpha{}^\beta \, \mathrm{d}x^\alpha \otimes \frac{\boldsymbol{\partial}}{\boldsymbol{\partial} x^\beta}. \tag{A.13}$$

In component form, Eq. (A.12) reads

$$\begin{aligned} b_{\alpha\beta} = \mathbf{b}\left(\frac{\boldsymbol{\partial}}{\boldsymbol{\partial} x^\alpha}, \frac{\boldsymbol{\partial}}{\boldsymbol{\partial} x^\beta}\right) &= \left\langle \frac{\boldsymbol{\partial}}{\boldsymbol{\partial} x^\alpha}, \mathscr{S}\left(\frac{\boldsymbol{\partial}}{\boldsymbol{\partial} x^\beta}\right) \right\rangle \\ &= \left\langle \frac{\boldsymbol{\partial}}{\boldsymbol{\partial} x^\alpha}, b_\beta{}^\gamma \frac{\boldsymbol{\partial}}{\boldsymbol{\partial} x^\gamma} \right\rangle \\ &= b_\beta{}^\gamma \, a_{\alpha\gamma}. \end{aligned} \tag{A.14}$$

Note that in the coordinates (x^α), all of the three matrices— $(a_{\alpha\beta})$, $(b_{\alpha\beta})$ and $\left(b_\alpha{}^\beta\right)$— are diagonal; what is more, it is known that in these coordinates, $b_1{}^1 = \kappa_1$, and $b_2{}^2 = \kappa_2$.

With these new definitions we can take a closer look at Eq. (A.10). We first write

$$\frac{\partial \hat{\mathbf{n}}}{\partial x^\alpha} \equiv -\mathscr{S}\left(\frac{\boldsymbol{\partial}}{\boldsymbol{\partial} x^\alpha}\right) \tag{A.15}$$

using the definition Eq. (A.11). Thanks to Eq. (A.12), the meaning of the third term in Eq. (A.10) now becomes immediately recognizable: it is just $-2z\, b_{\alpha\alpha} = -2z\kappa_\alpha \, a_{\alpha\alpha}$. To understand the meaning of the second term, we can rewrite it using the shape

operator as follows:

$$z^2 \left\langle \mathscr{S}\left(\frac{\boldsymbol{\partial}}{\boldsymbol{\partial} x^\alpha}\right), \mathscr{S}\left(\frac{\boldsymbol{\partial}}{\boldsymbol{\partial} x^\alpha}\right) \right\rangle = z^2 \left\langle b_\alpha{}^\beta \frac{\boldsymbol{\partial}}{\boldsymbol{\partial} x^\beta}, b_\alpha{}^\gamma \frac{\boldsymbol{\partial}}{\boldsymbol{\partial} x^\gamma} \right\rangle$$
$$= z^2 \, b_\alpha{}^\beta \, b_\alpha{}^\gamma \, a_{\beta\gamma} = z^2 \kappa_\alpha^2 \, a_{\alpha\alpha}. \tag{A.16}$$

After some rearrangements, we arrive at the desired result[1].

A.2.1.2 An Intuitive Argument. Let us consider a surface, M_z, which is parallel to $\mathcal{M}$ with a distance z away. To get $g_{\alpha\alpha}$, we can just compute the length of an infinitesimal arc on M_z in the x^α-direction: the arclength $d\ell_z$ is given by

$$d\ell_z = \sqrt{\left\| \frac{\partial \mathbf{Y}}{\partial x^\alpha} \, dx^\alpha \right\|^2} = \sqrt{g_{\alpha\alpha}} \, dx^\alpha. \tag{A.17}$$

It is related to the length of the corresponding arc on $\mathcal{M}$, $d\ell$, in the following way:

$$\frac{d\ell_z}{d\ell} = \frac{R_\alpha + z}{R_\alpha} \coloneqq \frac{\dfrac{1}{\kappa_\alpha} + z}{\dfrac{1}{\kappa_\alpha}} = 1 + z\kappa_\alpha, \tag{A.18}$$

where $R_\alpha \coloneqq \frac{1}{\kappa_\alpha}$ denotes the curvature radius. It follows that

$$d\ell_z = (1 + z\kappa_\alpha) \, d\ell = \sqrt{a_{\alpha\alpha}}(1 + z\kappa_\alpha) \, dx^\alpha, \tag{A.19}$$

which gives the desired result.

[1]There is a sign difference which results from our choice for $\hat{\mathbf{n}}$.

APPENDIX B

CATALOGUE OF DIMENSIONFUL ANALYTICAL RESULTS FOR INDENTATION STIFFNESS IN DIFFERENT LIMITS

This appendix contains analytical expressions written in terms of dimensionful parameters for the indentation stiffness of isotropic spheroidal and cylindrical shells in different limits. These expressions also hold for orthotropic shells in which case the effective elastic constants—E_{eff} and υ_{eff} (see **Section 3.2**)—should be used in place of the isotropic Young's modulus E and Poisson's ratio υ.

First, the zero-pressure stiffness of a doubly-curved shell can be written in terms of the shell material's Young's modulus E, Poisson's ratio υ and the shell thickness t as

$$k_0 = 8\sqrt{\frac{\kappa Y}{R_x R_y}} = \frac{4Et^2}{\sqrt{3(1-\upsilon^2)}}\frac{1}{\sqrt{R_x R_y}}. \tag{B.1}$$

When computing the indentation stiffness of a *pressurized* spheroidal shell, we believe that it is generally easier to first scale the pressure and then use the resulting nondimensionalized pressure to perform the calculation. Therefore, the following expressions are given in terms of the scaled pressure

$$\eta_{\text{s},y} = \frac{pR_y^2}{4\sqrt{\kappa Y}} = \frac{\sqrt{3(1-\upsilon^2)}}{2}\left(\frac{R_y}{t}\right)^2\frac{p}{E} \tag{B.2}$$

and the asphericity of the given shell $\beta = 1 - \frac{R_y}{R_x}$, which is another combination of parameters that commonly shows up in indentation expressions.

The high-pressure stiffness of spheroidal shells with $-1 < \beta \leq 1$ can be recast as

$$k_{\text{asy}} \approx \pi p R_y \sqrt{1+\beta}\left[\ln\left(4\eta_{\text{s},y}\frac{1+\beta}{1+\sqrt{1-\beta^2}}\right)\right]^{-1}. \tag{B.3}$$

Setting $\beta \overset{!}{=} 1$ in Eq. (B.3), we obtain the dimensionful asymptotic stiffness of a long cylindrical shell:

$$k_{\text{asy,cyl}} \approx \frac{\sqrt{2}\pi p R_y}{\ln 8\eta_{\text{s},y}}. \tag{B.4}$$

For the same cylindrical shell, when the internal pressure is relatively low, its indentation stiffness becomes

$$k_{\text{cyl}} \approx 2\pi^2 p R_y \left(11.6\sqrt{\eta_{\text{s},y}} - 2.66\eta_{\text{s},y}^{\frac{3}{2}} + 1.83\eta_{\text{s},y}^{\frac{5}{2}} - 0.998\eta_{\text{s},y}^{\frac{7}{2}}\right)^{-1}. \tag{B.5}$$

Finally, for spheroidal shells with $|\beta| < 1$, their stiffness near the critical external pressure is dictated by

$$k \approx \pi\,|p|\,R_y\sqrt{\left|\frac{\beta}{\eta_{\text{s},y}}\right|}\frac{1}{\sqrt{1-\epsilon}\,\sinh^{-1}\left(\sqrt{\dfrac{2}{\frac{4}{\pi^2}\frac{1}{|\beta|}+1+f(\beta)}}\dfrac{1}{\sqrt{\epsilon}}\right)}, \quad (p, \eta_{\text{s},y} < 0) \tag{B.6}$$

where

$$\epsilon = \begin{cases} 1 - \dfrac{1+\beta}{1-\beta}\,|\eta_{\text{s},y}|\,, & \text{for} \quad 0 \le \beta < 1, \\ 1 - |\eta_{\text{s},y}|\,, & \text{for} \quad -1 < \beta < 0, \end{cases} \tag{B.7}$$

and

$$f(\beta) = \begin{cases} \left(1 - \dfrac{4}{\pi^2}\right)\beta, & \text{for} \quad 0 \le \beta < 1, \\ 0, & \text{for} \quad -1 < \beta < 0. \end{cases} \tag{B.8}$$

APPENDIX C

UNRESCALED LINEAR ORTHOTROPIC SHALLOW-SHELL EQUATIONS

This appendix contains expressions for linearized (rectilinearly) orthotropic shallow-shell equations [1] written in terms of unrescaled coordinates without using tensor notation. The dimensionless version of the equations has been derived in Ref. [78]; we are here going to restore physical units.

For shells made of an orthotropic material, the compatibility equation takes the following form:

$$\sqrt{\lambda}\frac{\partial^4\Phi}{\partial x^4}+2E_{\text{eff}}\left(\frac{1}{2G_{12}}-\frac{\upsilon_{12}}{E_2}\right)\frac{\partial^4\Phi}{\partial x^2\,\partial y^2}+\frac{1}{\sqrt{\lambda}}\frac{\partial^4\Phi}{\partial y^4}=Y'\left(\frac{1}{R_2}\frac{\partial^2 w}{\partial x^2}+\frac{1}{R_1}\frac{\partial^2 w}{\partial y^2}\right), \quad \text{(C.1)}$$

and the EOE is given by

$$\begin{aligned}\sqrt{\lambda}\frac{\partial^4 w}{\partial x^4}+2\frac{1}{D'}\frac{t^3}{12}\left(2G_{12}+\frac{E_1\upsilon_{12}}{1-\upsilon_{12}\upsilon_{21}}\right)\frac{\partial^4 w}{\partial x^2\,\partial y^2}+\frac{1}{\sqrt{\lambda}}\frac{\partial^4 w}{\partial y^4}+\\ +\frac{1}{D'}\left(\frac{1}{R_2}\frac{\partial^2\Phi}{\partial x^2}+\frac{1}{R_1}\frac{\partial^2\Phi}{\partial y^2}\right)=\frac{1}{D'}\left(\sigma_0^{11}t\,\frac{\partial^2 w}{\partial x^2}+2\sigma_0^{12}t\,\frac{\partial^2 w}{\partial x\,\partial y}+\sigma_0^{22}t\,\frac{\partial^2 w}{\partial y^2}\right).\end{aligned} \quad \text{(C.2)}$$

Let $G_{12}\overset{!}{=}\frac{E_{\text{eff}}}{2(1+\upsilon_{\text{eff}})}$, i.e., assuming that the Huber form applies. We notice the following simplifications:

$$\frac{1}{2G_{12}}-\frac{\upsilon_{12}}{E_2}=\frac{1+\upsilon_{\text{eff}}}{E_{\text{eff}}}-\frac{\upsilon_{\text{eff}}}{E_{\text{eff}}}=\frac{1}{E_{\text{eff}}} \quad \text{(C.3)}$$

[1] The fact that the original nonlinear shallow-shell equations can be linearized implies that rectilinearly orthotropic shells can deform uniformly under a uniform pressure, at least in an approximate sense.

and

$$\frac{t^3}{12}\left(2G_{12}+\frac{E_1\upsilon_{12}}{1-\upsilon_{12}\upsilon_{21}}\right)=\frac{t^3}{12}\left(\frac{E_{\text{eff}}}{1+\upsilon_{\text{eff}}}+\frac{E_{\text{eff}}\upsilon_{\text{eff}}}{1-\upsilon_{\text{eff}}^2}\right)=\frac{E_{\text{eff}}t^3}{12\,(1-\upsilon_{\text{eff}}^2)}\equiv D'. \quad \text{(C.4)}$$

The two shallow-shell equations then reduce to

$$\left(\sqrt[4]{\lambda}\frac{\partial^2}{\partial x^2}+\frac{1}{\sqrt[4]{\lambda}}\frac{\partial^2}{\partial y^2}\right)^2\Phi =: \boldsymbol{\pounds}\,\Phi = Y'\,\Delta_{\text{V}}\,w \quad \text{(C.5, a)}$$

and

$$D'\,\boldsymbol{\pounds}\,w+\Delta_{\text{V}}\,\Phi=\sigma_0^{11}t\,\frac{\partial^2 w}{\partial x^2}+2\sigma_0^{12}t\,\frac{\partial^2 w}{\partial x\,\partial y}+\sigma_0^{22}t\,\frac{\partial^2 w}{\partial y^2}, \quad \text{(C.5, b)}$$

where $\Delta_{\text{V}} \equiv \frac{1}{R_2}\frac{\partial^2}{\partial x^2}+\frac{1}{R_1}\frac{\partial^2}{\partial y^2}$ denotes the Vlasov operator. Combining the two equations, we obtain

$$D'\,\boldsymbol{\pounds}^2\,w+Y'\,{\Delta_{\text{V}}}^2\,w=\boldsymbol{\pounds}\left(\sigma_0^{11}t\,\frac{\partial^2 w}{\partial x^2}+2\sigma_0^{12}t\,\frac{\partial^2 w}{\partial x\,\partial y}+\sigma_0^{22}t\,\frac{\partial^2 w}{\partial y^2}\right). \quad \text{(C.6)}$$

APPENDIX D

MECHANICAL PROPERTIES OF CURVILINEARLY ORTHOTROPIC SPHERES.

In this appendix, we will derive the indentation stiffness at the poles of an orthotropic spheroid in the absence of pressure. Recall that the type of orthotropy is curvilinear at the poles [see Fig. 3.1 (c)]. The result is obtained in two ways, first by a qualitative energy-balance argument which is then supported by analytically solving the governing linearized EOEs. We finish the appendix with a short discussion about what will happen if the spheroid is pressurized.

D.1 Zero-Pressure Indentation Stiffness.

D.1.1 The Energy-Balance Argument.

Landau and Lifshitz first used this approach to obtain the indentation stiffness and buckling pressure of an isotropic spherical shell [7]. We here modify their approach to include polar material orthotropy.

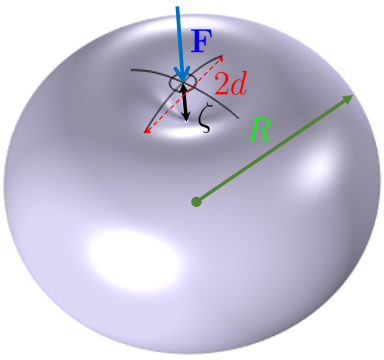

FIGURE D.1. Indenting a spheroidal shell near one of its poles. The part of the shell in the vicinity of the pole is locally spherical with radius denoted by R. A point load, $\mathbf{F}$, is applied right at the pole. The dimension of the resulting deformed region is roughly d, and the vertical deflection along $\mathbf{F}$ is denoted by ζ.

Figure D.1 depicts that a point load $\mathbf{F}$ is applied at one of a spheroid's poles, the center of a locally spherical region with radius R. The area of the resulting deformed region is of the order d^2 ($\sim d^2$). The deflection ζ varies significantly over a distance of d, which implies that the bending energy is $\sim E_r t^3 \left(\frac{\zeta}{d^2}\right)^2 d^2$, where E_r denotes Young's modulus along the meridional direction [the red curves in Fig. 3.1 (c)]. The reason why E_r was used to estimate the bending energy is that from the cross-sectional view, Fig. D.1, shell bending mainly occurs in the meridional direction, while stretching happens in the zonal direction [the blue curves in Fig. 3.1 (c)].

Strain does not depend on d and is $\sim \frac{\zeta}{R}$. The stretching energy is thus $\sim E_\theta t \left(\frac{\zeta}{R}\right)^2 d^2$, and the total elastic energy is roughly

$$U_{\text{tot}} \sim \frac{E_r t^3 \zeta^2}{d^2} + \frac{E_\theta t \zeta^2}{R^2} d^2. \tag{D.1}$$

The global minimum of U_{tot} can be rapidly obtained by recalling the AM-GM inequality:

$$U_{\text{min}} \sim \frac{2\sqrt{E_r E_\theta} t^2 \zeta^2}{R} = 2\sqrt{\left(\frac{E_r t^3 \zeta^2}{d^2}\right)\left(\frac{E_\theta t \zeta^2}{R^2} d^2\right)} \leq \frac{E_r t^3 \zeta^2}{d^2} + \frac{E_\theta t \zeta^2}{R^2} d^2 \sim U_{\text{tot}}. \tag{D.2}$$

Varying U_{min} with respect to ζ and equating the result to $F\,\delta\zeta$, the variation of the work done by the point load, we find the deflection $\zeta \sim \frac{FR}{4\sqrt{E_r E_\theta} t^2}$ and hence the indentation stiffness

$$k_0^{\text{pole}} = \frac{F}{\zeta} \sim \frac{4\sqrt{E_r E_\theta} t^2}{R}, \tag{D.3}$$

which agrees with Eq. (3.28) up to a factor of two. As this argument explicitly shows, although the local symmetry at the equator (see **Section 3.3.4**) completely breaks down at the poles, i.e., the two orthogonal directions now become curvilinear

and hence distinguishable, the geometric-mean dependence persists and stems from balancing the bending and stretching energies.

D.1.2 The Analytical Approach.

Equation (D.3) can also be obtained by solving the EOEs that govern the deformations of a curvilinearly orthotropic shallow spherical shell. The full nonlinear EOEs can be found in, for example, Ref. [50]. Since we only consider small deformations due to a point load at the center of the shell, it is reasonable to linearize these equations and further assume, from a symmetry point of view, that the deformations of interest are axisymmetric, i.e., do not vary along the azimuthal direction. In this case, the governing equations reduce to [66]

$$D_r \, \Delta_{\frac{1}{\sqrt{\lambda}}} \, y(r) + \frac{y(r)}{R} = -\frac{F}{2\pi} \frac{1}{r} \tag{D.4, a}$$

$$\frac{1}{Y_\theta} \, \Delta_{\frac{1}{\sqrt{\lambda}}} \, \phi(r) - \frac{\phi(r)}{R} = 0, \tag{D.4, b}$$

where $D_r \coloneqq \frac{E_r t^3}{12(1-\upsilon_{r\theta}\upsilon_{\theta r})}$ is the bending stiffness along the meridional direction, and $Y_\theta \coloneqq E_\theta t$ the Young's modulus in the zonal direction. That D_r and E_θ show up in the governing equations supports our previous observation that shell bending and stretching occur in different directions. The fields y and ϕ are the first derivative of the normal displacement w and the Airy stress function Φ, respectively: $y \coloneqq \frac{\mathrm{d}w}{\mathrm{d}r}$, and $\phi \coloneqq \frac{\mathrm{d}\Phi}{\mathrm{d}r}$, where r is the distance away from the pole. The operator $\Delta_\nu \equiv \frac{\mathrm{d}^2}{\mathrm{d}r^2} + \frac{1}{r}\frac{\mathrm{d}}{\mathrm{d}r} - \left(\frac{\nu}{r}\right)^2$ ($\nu \in \mathbb{C}$) is the Bessel differential operator. It is known that Bessel functions of the first kind with order ν (denoted by J_ν) are its eigenfunctions. This motivates us to solve Eqs. (D.4) using the Hankel transform.

Hankel transform. Roughly speaking, Hankel transform is like Fourier transform in polar coordinates and is often used to solve *linear axisymmetric* differential equations. The Hankel transform of a well-behaved axisymmetric function $f(r)$ is given by [88]

$$\hat{f}_\nu(k) \equiv \mathscr{H}_\nu \left\{ f(r) \right\} (k) = \int_0^{+\infty} r \, \mathrm{d}r \, f(r) J_\nu(kr). \tag{D.5}$$

The inverse transform is given by

$$f(r) = \int_0^{+\infty} k \, \mathrm{d}k \, \hat{f}_\nu(k) J_\nu(kr). \tag{D.6}$$

The Hankel transform of the Bessel operator, Δ_ν, is simply $-k^2$, which is independent of ν. This can be most easily seen by recalling the definition of the Bessel differential equation:

$$\left(\Delta_\nu + k^2 \right) J_\nu(kr) = 0. \tag{D.7}$$

It follows that for an axisymmetric function $f(r)$,

$$\Delta_\nu \, f(r) = \Delta_\nu \int_0^{+\infty} k \, \mathrm{d}k \, \hat{f}_\nu(k) J_\nu(kr) = \int_0^{+\infty} k \, \mathrm{d}k \, \left(-k^2 \hat{f}_\nu(k) \right) J_\nu(kr). \tag{D.8}$$

It is also straightforward to obtain the Hankel transform of the function $\frac{1}{r}$: by definition,

$$\mathscr{H}_\nu \left\{ \frac{1}{r} \right\} (k) = \int_0^{+\infty} r \, \mathrm{d}r \, \frac{1}{r} J_\nu(kr) = \int_0^{+\infty} \mathrm{d}r \, J_\nu(kr) = \frac{1}{k} \int_0^{+\infty} \mathrm{d}u \, J_\nu(u) = \frac{1}{k}, \tag{D.9}$$

where we have used the fact that for all ν,

$$\int_0^{+\infty} \mathrm{d}x\, J_\nu(x) = 1. \tag{D.10}$$

The Hankel transform of Eqs. (D.4) is hence

$$-D_r k^2 \hat{y}_{\frac{1}{\sqrt{\lambda}}}(k) + \frac{1}{R}\hat{\phi}_{\frac{1}{\sqrt{\lambda}}}(k) = -\frac{F}{2\pi}\frac{1}{k} \tag{D.11, a}$$

$$-\frac{1}{Y_\theta}k^2\hat{\phi}_{\frac{1}{\sqrt{\lambda}}}(k) - \frac{1}{R}\hat{y}_{\frac{1}{\sqrt{\lambda}}}(k) = 0. \tag{D.11, b}$$

Substituting Eq. (D.11, b) into Eq. (D.11, a) to eliminate $\hat{\phi}_{\frac{1}{\sqrt{\lambda}}}(k)$, we get, after applying the inverse transform,

$$\frac{\mathrm{d}w}{\mathrm{d}r}(r) =: y(r) = \frac{F}{2\pi}\int_0^{+\infty} \mathrm{d}k\, \frac{k^2}{D_r k^4 + \dfrac{Y_\theta}{R^2}} J_{\frac{1}{\sqrt{\lambda}}}(kr). \tag{D.12}$$

To proceed, we impose the boundary conditions $w(0) = -\zeta$ and $\lim\limits_{r\to+\infty} w(r) = 0$ which together give

$$\int_0^{+\infty} \mathrm{d}r\, \frac{\mathrm{d}w}{\mathrm{d}r}(r) = \lim_{r\to+\infty} w(r) - w(0) = \zeta. \tag{D.13}$$

Combining Eqs. (D.12) and (D.13), we finally attain the following relation between ζ and F:

$$\begin{aligned}\zeta &= \int_0^{+\infty} \mathrm{d}r \, \frac{F}{2\pi} \int_0^{+\infty} \mathrm{d}k \, \frac{k^2}{D_r k^4 + \dfrac{Y_\theta}{R^2}} J_{\frac{1}{\sqrt{\lambda}}}(kr) \\ &= \frac{F}{2\pi} \int_0^{+\infty} \mathrm{d}k \, \frac{k^2}{D_r k^4 + \dfrac{Y_\theta}{R^2}} \int_0^{+\infty} \mathrm{d}r \, J_{\frac{1}{\sqrt{\lambda}}}(kr) \\ &= \frac{F}{2\pi} \int_0^{+\infty} \mathrm{d}k \, \frac{k}{D_r k^4 + \dfrac{Y_\theta}{R^2}} = F \frac{R}{8\sqrt{D_r Y_\theta}}.\end{aligned} \tag{D.14}$$

From Eq. (D.14), we can get the indentation stiffness:

$$k \coloneqq \frac{F}{\zeta} = \frac{8\sqrt{D_r Y_\theta}}{R} = \frac{4\sqrt{E_r E_\theta} t^2}{\sqrt{3\left(1 - \upsilon_{r\theta}\upsilon_{\theta r}\right)}} \frac{1}{R} \tag{D.15}$$

(cf. Eq. (3.28)). This proves our claim in the main text (see **Section 3.3.4**).

D.2 Pressurized Orthotropic Spheroids.

Recall the fact that near its poles, a spheroid is locally spherical. Therefore, the following discussions are centered around curvilinearly orthotropic spherical shells.

Unlike its isotropic counterpart, a curvilinearly orthotropic sphere does not deform uniformly under a constant pressure. This can be seen by substituting the membrane solution

$$\begin{cases} y_{\mathrm{m}}(r) = 0, \\ \phi_{\mathrm{m}}(r) = \dfrac{1}{2} p R r, \end{cases} \tag{D.16}$$

into the nonlinear shallow-shell equations [66]

$$D_r\,\Delta_{\frac{1}{\sqrt{\lambda}}}\,y(r) - \frac{\phi(r)}{r}\left(y(r) - \frac{r}{R}\right) = \frac{1}{2}pr \qquad \text{(D.17, a)}$$

$$\frac{1}{Y_\theta}\,\Delta_{\frac{1}{\sqrt{\lambda}}}\,\phi(r) + \frac{1}{2}\frac{y(r)}{r}\left(y(r) - \frac{2r}{R}\right) = 0. \qquad \text{(D.17, b)}$$

Equation (D.17, b) gives $\left(1-\frac{1}{\lambda}\right)\frac{pR}{Y_\theta} = 0$ which only holds in the isotropic case ($\lambda = 1$). Moreover, we notice that $\left(1-\frac{1}{\lambda}\right)\frac{pR}{Y_\theta}$ switches its sign at $\lambda = 1$. The presence of this term illustrates the fact that upon being pressurized, spheres with a curvilinear orthotropy pattern deform differently depending on whether $E_r > E_\theta$ or the other way around [6, 83]. Therefore, the term cannot be ignored in general, and linearization using the membrane solution thus generally fails for these shells.

In fact, as Reissner has demonstrated, for pressurized curvilinearly orthotropic spheres, both the displacement field $w(r)$ and the Airy stress function $\Phi(r)$ scale as $r^{\frac{1}{\sqrt{\lambda}}+1}$ near the origin [83]. As a result, the actual stress, $\|\boldsymbol{\sigma}(r)\|\,t \sim \frac{\Phi(r)}{r^2}$ will have the power-law behavior $r^{\frac{1}{\sqrt{\lambda}}-1}$; that is, depending on the magnitude of λ, the stress at the poles will either vanish ($\lambda < 1$) or explode ($\lambda > 1$). This stress singularity makes it challenging to derive the indentation stiffness and buckling pressure of pressurized curvilinearly orthotropic spheres in general.

However, for sufficiently low pressures, such that the approximation $\left(1-\frac{1}{\lambda}\right)\frac{pR}{Y_\theta} \approx 0$ can be safely made, following the same procedure as in the pressureless case, we

obtain

$$\begin{aligned}\zeta &= \frac{F}{2\pi}\int_0^{+\infty}\mathrm{d}k\,\frac{k}{D_r k^4+\frac{pR}{2}k^2+\frac{Y_\theta}{R^2}} = \frac{F}{4\pi}\sqrt{\frac{R^2}{D_r Y_\theta}}\int_0^{+\infty}\frac{\mathrm{d}u}{u^2+2\eta_{\mathrm{s},y}u+1}\\ &= F\frac{R}{8\sqrt{D_r Y_\theta}}\frac{1-\frac{2}{\pi}\arcsin\eta_{\mathrm{s},y}}{\sqrt{1-\eta_{\mathrm{s},y}^2}},\end{aligned} \tag{D.18}$$

where $\eta_{\mathrm{s},y} \coloneqq \frac{pR^2}{4\sqrt{D_r Y_\theta}}$. The indentation stiffness in this case is hence

$$k \equiv \frac{F}{\zeta} = \frac{8\sqrt{D_r Y_\theta}}{R}\frac{\sqrt{1-\eta_{\mathrm{s},y}^2}}{1-\frac{2}{\pi}\arcsin\eta_{\mathrm{s},y}}. \tag{D.19}$$

Note that Eq. (D.19) is still invariant under interchange of labels r and θ. Mathematically, this means that $k(\lambda) = k\left(\frac{1}{\lambda}\right)$. This analytical insight is confirmed by `COMSOL` simulations, as Fig. D.2 shows. At low pressures, such that $\frac{pR}{Y_\theta} \approx 0$, indentation stiffness of the two orthotropic spheres is basically identical to each other; however, when the scaled pressure increases to order one ($\eta_{\mathrm{s},y} \sim 1$), we start to see deviations from the theory. The fact that the two sets of data fall onto different sides of the theory curve is a result of the term $\left(1-\frac{1}{\lambda}\right)\frac{pR}{Y_\theta}$ being non-negligible.

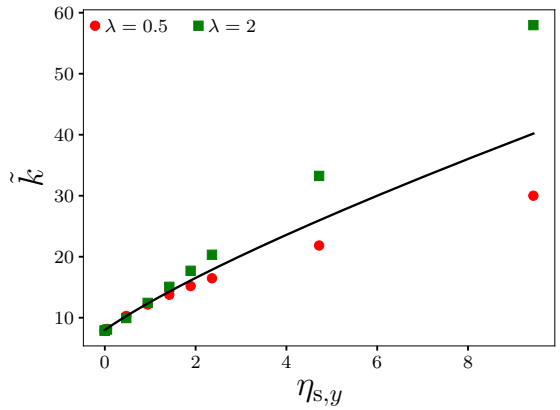

FIGURE D.2. Indentation stiffness of two orthotropic spheres with different degrees of anisotropy as a function of pressure. Symbols denote data obtained from COMSOL simulations. The solid curve corresponds to the analytical expression Eq. (D.19). Indentation stiffness is scaled by $\frac{\sqrt{D_r Y_\theta}}{R}$.

APPENDIX E

DERIVING THE ZERO-PRESSURE INDENTATION STIFFNESS OF LONG CYLINDERS

In this appendix, we will combine Yuan's approach [18] and the rescaling transformation to solve the linearized shallow-shell equation for long cylindrical shells:

$$D' \, \boldsymbol{\pounds}^2 \, w(x,s) + \frac{Y'}{R^2} \frac{\partial^4 w(x,s)}{\partial x^4} = \boldsymbol{\pounds} \, q(x,s) \tag{E.1, a}$$

(see Eq. (C.6)) or equivalently,

$$D' \, \boldsymbol{\pounds}'^2 \, w'(x',s') + \frac{Y'}{R'^2} \frac{\partial^4 w'(x',s')}{\partial x'^4} = \boldsymbol{\pounds}' \, q'(x',s'). \tag{E.1, b}$$

E.1 Yuan's Approach

In short, the approach by Yuan has two main distinctive features compared with our analysis in Ref. [5]. First, along the circumferential direction (associated with the coordinate s), a Fourier series defined on $(-\pi R, \pi R]$, instead of a Fourier transform, was used: More specifically, a well-behaved function $f(x,s)$ can be written as

$$f(x,s) = \int_{-\infty}^{+\infty} \frac{\mathrm{d}k}{2\pi} \, \hat{f}(k,s) e^{\mathrm{i}kx} = \int_{-\infty}^{+\infty} \frac{\mathrm{d}k}{2\pi} \sum_{n=-\infty}^{\infty} \hat{f}_n(k) e^{\mathrm{i}n\frac{s}{R}} e^{\mathrm{i}kx}. \tag{E.2}$$

Furthermore, if the function $f(x,s)$ is even in both x and s, the above expression reduces to

$$f(x,s) = 2 \int_0^{+\infty} \frac{\mathrm{d}k}{2\pi} \left[\frac{1}{2} \hat{f}_0(k) + \sum_{n=1}^{\infty} \hat{f}_n(k) \cos\left(n \frac{s}{R}\right) \right] \cos kx, \tag{E.3}$$

where we have implicitly used the fact that the Fourier transform of an even function is even. For a separable function, i.e., $f(x,s) = X(x)S(s)$, Eq. (E.3) becomes

$$f(x,s) = 2\left[\frac{1}{2}S_0 + \sum_{n=1}^{\infty} S_n \cos\left(n\frac{s}{R}\right)\right] \int_0^{+\infty} \frac{\mathrm{d}k}{2\pi}\, \hat{X}(k) \cos kx. \tag{E.4}$$

Second, Yuan did not use the Dirac delta function to model a concentrated load; instead, he first considered a uniformly distributed load over a rectangular region and then shrank the size of the region.

E.2 The Rescaling Transformation

We can thus write

$$\begin{aligned} w(x,s) &= \int_0^{+\infty} \frac{\mathrm{d}k}{2\pi} \left[\hat{w}_0(k) + \sum_{n=1}^{\infty} 2\hat{w}_n(k) \cos\left(n\frac{s}{R}\right)\right] \cos kx \\ &= \sum_{n=0}^{\infty} \left[(2-\delta_{0n}) \int_0^{+\infty} \frac{\mathrm{d}k}{2\pi}\, \hat{w}_n(k) \cos kx \cos\left(n\frac{s}{R}\right)\right] \end{aligned} \tag{E.5}$$

since the normal displacement field $w(x,s)$ must be an even function in both x and s from a symmetry point of view. The constant load is applied on a rectangular region that is symmetric with respect to the origin; therefore, $q(x,s)$ is even and separable: $q(x,s) = X(x)Q(s)$, and

$$q(x,s) = \sum_{n=0}^{\infty} \left[(2-\delta_{0n}) \int_0^{+\infty} \frac{\mathrm{d}k}{2\pi}\, \hat{X}(k) Q_n \cos kx \cos\left(n\frac{s}{R}\right)\right]. \tag{E.6}$$

Letting the region be $R = \{(x, s) \in [-\epsilon, \epsilon] \times [-c, c]\}$, we can then determine $\hat{X}(k)$ and Q_n. By definition,

$$\hat{X}(k) = \int_{-\infty}^{+\infty} \mathrm{d}x\, X(x) e^{-\mathrm{i}kx} = 2\int_0^{\epsilon} \mathrm{d}x\, \cos kx = 2\epsilon\, \mathrm{sinc}\, k\epsilon, \tag{E.7}$$

and

$$Q_n = \frac{2}{\pi R}\int_0^{\pi R} \mathrm{d}s\, Q(s) \cos\left(n\frac{s}{R}\right) = \frac{2}{\pi R}\int_0^{c} \mathrm{d}s\, q_0 \cos\left(n\frac{s}{R}\right) = \frac{2}{\pi}\frac{c}{R}\,\mathrm{sinc}\left(n\frac{c}{R}\right) q_0. \tag{E.8}$$

The intensity of the load is denoted by q_0, and the total force is hence $F = q_0 A = 4q_0 c\epsilon$. In the limits of $k\epsilon \to 0$ and $n\frac{c}{R} \to 0$,

$$\hat{X}(k) \approx 2\epsilon, \quad \text{and} \quad Q_n \approx \frac{2}{\pi}\frac{c}{R} q_0. \tag{E.9}$$

Remark. In Yuan's original formulation of the problem, there is an additional concentrated load being applied at the bottom of the cylinder ($s = \pm\pi R$). As a consequence, when computing the Fourier coefficients Q_n for the original system, an extra term,

$$\frac{2}{\pi R}\int_{\pi R - c}^{\pi R} \mathrm{d}s\, Q(s) \cos\left(n\frac{s}{R}\right) = (-1)^n Q_n, \tag{E.10}$$

needs to be added. This leads to vanishing of the odd terms in the Fourier series.

Therefore, for a point load,

$$q(x, s) \approx \frac{F}{\pi R}\sum_{n=0}^{\infty}\left[(2 - \delta_{0n})\int_0^{+\infty} \frac{\mathrm{d}k}{2\pi}\, \cos kx \cos\left(n\frac{s}{R}\right)\right]. \tag{E.11}$$

Substituting Eqs. (E.5) and (E.11) into Eq. (E.1, a), we obtain, after some algebra,

$$\hat{w}_n(k) = \frac{F}{\pi R} \frac{\left(\sqrt[4]{\lambda} k^2 + \dfrac{1}{\sqrt[4]{\lambda}} \dfrac{n^2}{R^2} \right)^2}{D' \left(\sqrt[4]{\lambda} k^2 + \dfrac{1}{\sqrt[4]{\lambda}} \dfrac{n^2}{R^2} \right)^4 + \dfrac{Y'}{R^2} k^4}. \tag{E.12}$$

We now apply the rescaling transformation in Fourier space: $R \mapsto R' = \sqrt[4]{\lambda} R$, $k \mapsto k' = \sqrt[8]{\lambda} k$ and $n \mapsto n' = \sqrt[8]{\lambda} n$; Eq. (E.12) then reduces to

$$\hat{w}_n(k) = \sqrt[4]{\lambda} \frac{1}{\pi} \frac{F R'^3}{D'} \frac{\left(\tilde{k}'^2 + n'^2 \right)^2}{\left(\tilde{k}'^2 + n'^2 \right)^4 + \gamma' \tilde{k}'^4}, \tag{E.13}$$

where $\tilde{k}' \coloneqq R' k' = \sqrt[8]{\lambda^3} R k$, which is dimensionless, and $\gamma' \coloneqq \frac{Y' R'^2}{D'}$ is the Föppl-von Kármán number for the rescaled system. We note that Eq. (E.13) can also be attained by directly substituting into Eq. (E.1, b) Fourier series and transforms that are written in terms of the rescaled variables, e.g.,

$$f(x', s') = \frac{1}{\sqrt[8]{\lambda}} \int_{-\infty}^{+\infty} \frac{\mathrm{d}k'}{2\pi} \sum_{n=-\infty}^{\infty} \hat{f}_{n'}(k') e^{\mathrm{i}n' \frac{s'}{R'}} e^{\mathrm{i}k' x'}. \tag{E.14}$$

From Eq. (E.13), we can get the following expression for the inverse of the indentation stiffness:

$$\begin{aligned} \frac{1}{k^0_{\mathrm{cyl}}(\lambda)} \coloneqq \frac{w(0,0)}{F} &= \frac{1}{2\pi^2} \sqrt[8]{\lambda} \frac{R'^2}{D'} \sum_{n=0}^{\infty} \left[(2 - \delta_{0n}) \int_0^{+\infty} \mathrm{d}u \, \frac{\left(u^2 + n'^2\right)^2}{\left(u^2 + n'^2\right)^4 + \gamma' u^4} \right] \\ &= \frac{1}{2\pi^2} \sqrt[8]{\lambda} \frac{R'^2}{D'} \int_0^{+\infty} \frac{\mathrm{d}u}{u^4 + \gamma'} + \\ &\quad + \frac{1}{\pi^2} \sqrt[8]{\lambda} \frac{R'^2}{D'} \sum_{n=1}^{\infty} \int_0^{+\infty} \mathrm{d}u \, \frac{\left(u^2 + n'^2\right)^2}{\left(u^2 + n'^2\right)^4 + \gamma' u^4}. \end{aligned} \tag{E.15}$$

Remark. Notice that the $n = 0$ mode does not lead to a divergence, unlike the situation in Ref. [5] where the stiffness was written in terms of the following double integral:

$$\frac{1}{k^0_{\text{cyl}}(\lambda = 1)} = \frac{1}{2\pi^2}\frac{R}{\sqrt{DY}}\int_0^{\frac{\pi}{2}} \mathrm{d}\theta \int_0^{+\infty} \frac{\mathrm{d}u}{u^2 + \cos^4\theta}, \tag{E.16}$$

which diverges in the infrared limit ($\mathbf{u} \to \mathbf{0}$). As Yuan found, the contribution of the $n = 0$ mode to the indentation stiffness is in fact negligible compared to other modes; as a result, the first term on the right-hand side of Eq. (E.15) can be neglected.

Equation (E.15) takes the same form as Eq. (10) in Ref. [18], except for an extra factor of $\frac{1}{2}\sqrt[8]{\lambda}$. We can hence directly apply Yuan's final result, Eq. (17), without actually evaluating the definite integrals in Eq. (E.15):

$$\frac{1}{k^0_{\text{cyl}}(\lambda)} \approx \frac{1}{2\pi}\sqrt[8]{\lambda}\frac{3\sqrt{2}\,(1-\upsilon^2_{\text{eff}})}{E_{\text{eff}}}\frac{R'^2}{t^3}\sum_{n=1}^{\infty}\frac{1}{n'^3}\frac{\sqrt{1+\Xi_n}}{\Xi_n}, \tag{E.17}$$

where $\Xi_n^2 \coloneqq 1 + \frac{3\left(1-\upsilon^2_{\text{eff}}\right)}{4n'^4}\left(\frac{R'}{t}\right)^2 = 1 + \frac{3\left(1-\upsilon^2_{\text{eff}}\right)}{4n^4}\left(\frac{R}{t}\right)^2$. After some rearrangements, we finally get Eq. (3.29).

APPENDIX F

EVALUATING THE STIFFNESS INTEGRAL

In this appendix, we will show the details how we evaluated the definite integrals in Eqs. (3.32) and (3.36). We will start with the latter, which is a special case of the former.

F.1 Equation (3.36)

Setting $\beta_0 = 1$ (and hence $\beta' = 1$ and $\beta'_\lambda = 2\sqrt{\lambda} - 1$) in Eq. (3.32) gives

$$\frac{1}{k_{\text{cyl}}(\eta_{\text{s},y}(\lambda), \lambda)} \coloneqq \frac{1}{8\pi^2}\sqrt{\frac{R'^2}{D'Y'}}\mathcal{I}_1(\eta_{\text{s},y}(\lambda), \lambda), \tag{F.1}$$

where $R' = \sqrt[4]{\lambda}R$ with R the radius of cylinders, and

$$\begin{aligned}\mathcal{I}_1(\eta_{\text{s},y}(\lambda), \lambda) &\coloneqq \int_0^{2\pi} \mathrm{d}\varphi \int_0^{+\infty} \frac{\mathrm{d}u}{u^2 + 2\eta_{\text{s},y}\left(1 + \beta'_\lambda \sin^2\varphi\right) u + \cos^4\varphi} \\ &= 4\int_0^{\frac{\pi}{2}} \mathrm{d}\varphi \int_0^{+\infty} \frac{\mathrm{d}u}{u^2 + 2\eta_{\text{s},y}\left(1 + \beta'_\lambda \cos^2\varphi\right) u + \sin^4\varphi};\end{aligned} \tag{F.2}$$

we have used the fact

$$\int_0^{2\pi} \mathrm{d}\varphi\, f(\cos^2\varphi) = 4\int_0^{\frac{\pi}{2}} \mathrm{d}\varphi\, f(\sin^2\varphi). \tag{F.3}$$

To evaluate $\mathcal{I}_1(\eta_{\mathrm{s},y}(\lambda),\lambda)$, we make two changes of variables: $s = u\csc^2\varphi$ and $t = \cot\varphi$; as a result,

$$\begin{aligned}\mathcal{I}_1(\eta_{\mathrm{s},y}(\lambda),\lambda) &= 4\int_0^{\frac{\pi}{2}} \mathrm{d}\varphi\, \frac{\csc^4\varphi}{\csc^4\varphi} \int_0^{+\infty} \frac{\mathrm{d}u}{u^2 + 2\eta_{\mathrm{s},y}\left(1+\beta'_\lambda\cos^2\varphi\right)u + \sin^4\varphi} \\ &= 4\int_0^{\frac{\pi}{2}} \mathrm{d}\varphi\, \csc^2\varphi \int_0^{+\infty} \frac{\mathrm{d}(u\csc^2\varphi)}{\left(u\csc^2\varphi\right)^2 + 2\eta_{\mathrm{s},y}\left(\csc^2\varphi + \beta'_\lambda\cot^2\varphi\right)\left(u\csc^2\varphi\right) + 1} \\ &= 4\int_0^{+\infty}\int_0^{+\infty} \frac{\mathrm{d}s\,\mathrm{d}t}{s^2 + 2\eta_{\mathrm{s},y}\left(1+2\sqrt{\lambda}t^2\right)s + 1},\end{aligned} \tag{F.4}$$

where in the last step, we changed the order of integration. We notice at this point that we can easily "tease out" the integral's explicit λ-dependence by making another change of variables $v = 2\sqrt{\eta_{\mathrm{s},y}}\sqrt[4]{\lambda}t$:

$$\mathcal{I}_1(\eta_{\mathrm{s},y}(\lambda),\lambda) = \frac{2}{\sqrt{\eta_{\mathrm{s},y}}\sqrt[4]{\lambda}} \int_0^{+\infty}\int_0^{+\infty} \frac{\mathrm{d}s\,\mathrm{d}v}{sv^2 + (s^2 + 2\eta_{\mathrm{s},y}s + 1)}. \tag{F.5}$$

It is now straightforward to evaluate $\mathcal{I}_1(\eta_{\mathrm{s},y}(\lambda),\lambda)$:

$$\begin{aligned}\mathcal{I}_1(\eta_{\mathrm{s},y}(\lambda),\lambda) &= \frac{2}{\sqrt{\eta_{\mathrm{s},y}}\sqrt[4]{\lambda}} \int_0^{+\infty} \frac{\mathrm{d}s}{s} \int_0^{+\infty} \frac{\mathrm{d}v}{v^2 + \left(\sqrt{\dfrac{s^2 + 2\eta_{\mathrm{s},y}s + 1}{s}}\right)^2} \\ &= \frac{\pi}{\sqrt{\eta_{\mathrm{s},y}}\sqrt[4]{\lambda}} \int_0^{+\infty} \frac{\mathrm{d}s}{\sqrt{s}} \frac{1}{\sqrt{s^2 + 2\eta_{\mathrm{s},y}s + 1}} \\ &= \frac{2\pi}{\sqrt{\eta_{\mathrm{s},y}}\sqrt[4]{\lambda}} \int_0^{+\infty} \frac{\mathrm{d}x}{\sqrt{x^4 + 2\eta_{\mathrm{s},y}x^2 + 1}}.\end{aligned} \tag{F.6}$$

The last integral in the equation above can be expressed in terms of the complete elliptic integral of the first kind [89]:

$$\begin{aligned}
\int_0^{+\infty} \frac{\mathrm{d}x}{\sqrt{x^4+2\eta_{\mathrm{s},y}x^2+1}} &= \int_0^{+\infty} \frac{\mathrm{d}x}{\sqrt{(x^2+1)^2-2(1-\eta_{\mathrm{s},y})x^2}} \\
&= \int_0^{\frac{\pi}{2}} \frac{\mathrm{d}(\tan\theta)}{\sqrt{(\tan^2\theta+1)^2-2(1-\eta_{\mathrm{s},y})\tan^2\theta}} \\
&= \int_0^{\frac{\pi}{2}} \frac{\sec^2\theta\,\mathrm{d}\theta}{\sqrt{\sec^4\theta-2(1-\eta_{\mathrm{s},y})\tan^2\theta}} \\
&= \int_0^{\frac{\pi}{2}} \frac{\mathrm{d}\theta}{\sqrt{1-\frac{1}{2}(1-\eta_{\mathrm{s},y})\sin^2 2\theta}} = \frac{1}{2}\int_0^{\pi} \frac{\mathrm{d}\phi}{\sqrt{1-\frac{1}{2}(1-\eta_{\mathrm{s},y})\sin^2\phi}} \\
&= \mathrm{K}\left(\frac{1}{2}(1-\eta_{\mathrm{s},y})\right);
\end{aligned} \tag{F.7}$$

to arrive at the last step, we have used

$$\int_0^{\pi} \mathrm{d}\phi\, g(\sin^2\phi) = 2\int_0^{\frac{\pi}{2}} \mathrm{d}\phi\, g(\sin^2\phi). \tag{F.8}$$

After some more algebra, we obtain Eq. (3.36).

Remark. By changing the order of integration, like what we did in Ref. [5], we get the following identity for the complete elliptic integral of the first kind:

$$\boxed{\mathrm{K}(x) = \frac{\sqrt{2}}{\pi}\int_0^{+\infty} \mathrm{d}u\, \frac{\arccos\left(u^2+1-2x\right)}{\sqrt{1-\left(u^2+1-2x\right)^2}}}. \tag{F.9}$$

F.2 Equation (3.32)

We now return to the more general case, Eq. (3.32); the way of evaluating the integral is essentially the same, but the changes of variables involved will require slightly more thoughts.

We start by rewriting the integral in Eq. (3.32):

$$\begin{aligned}\mathcal{I}(\eta_{\mathrm{s},y}(\lambda),\beta_0,\lambda) &\coloneqq \int_0^{2\pi}\mathrm{d}\varphi\int_0^{+\infty}\frac{\mathrm{d}u}{u^2+2\eta_{\mathrm{s},y}\left(1+\beta'_\lambda\sin^2\varphi\right)u+\left(1-\beta'\sin^2\varphi\right)^2}\\ &= 4\int_0^{\frac{\pi}{2}}\mathrm{d}\varphi\int_0^{+\infty}\frac{\mathrm{d}u}{u^2+2\eta_{\mathrm{s},y}\left(1+\beta'_\lambda\cos^2\varphi\right)u+\left(1-\beta'\cos^2\varphi\right)^2}\\ &= 4\int_0^{\frac{\pi}{2}}\frac{\mathrm{d}\varphi}{1-\beta'\cos^2\varphi}\int_0^{+\infty}\frac{\mathrm{d}v}{v^2+2\eta_{\mathrm{s},y}\left(\dfrac{1+\beta'_\lambda\cos^2\varphi}{1-\beta'\cos^2\varphi}\right)v+1},\end{aligned} \tag{F.10}$$

where $v \coloneqq \frac{u}{1-\beta'\cos^2\varphi}$. Realizing

$$\frac{\mathrm{d}}{\mathrm{d}\varphi}\arctan\left(\frac{1}{\sqrt{1-\beta'}}\tan\varphi\right) = \sqrt{1-\beta'}\frac{1}{1-\beta'\cos^2\varphi}, \tag{F.11}$$

we make the change of variables

$$s = \arctan\left(\frac{1}{\sqrt{1-\beta'}}\tan\varphi\right). \tag{F.12}$$

As a result, we can make the following simplification:

$$\frac{1+\beta'_\lambda\cos^2\varphi}{1-\beta'\cos^2\varphi} = 1+\frac{\beta'+\beta'_\lambda}{\sec^2\varphi-\beta'}$$
$$= 1+\frac{\beta'+\beta'_\lambda}{1+(1-\beta')\tan^2 s-\beta'} = 1+\frac{\beta'+\beta'_\lambda}{1-\beta'}\cos^2 s \coloneqq 1+\alpha'\cos^2 s, \tag{F.13}$$

where

$$\alpha' \coloneqq \frac{\beta'+\beta'_\lambda}{1-\beta'} = \frac{2\beta_0}{1-\beta_0} = \frac{1+\beta_0}{1-\beta_0} - 1 \coloneqq \alpha - 1, \tag{F.14}$$

a combination of parameters, which is independent of λ; accordingly, with the new integration variable,

$$\mathcal{I}(\eta_{\mathrm{s},y}(\lambda),\beta_0,\lambda) = \frac{4}{\sqrt{1-\beta'}}\int_0^{\frac{\pi}{2}}\mathrm{d}s\int_0^{+\infty}\frac{\mathrm{d}v}{v^2+2\eta_{\mathrm{s},y}\left(1+\alpha'\cos^2 s\right)v+1}. \tag{F.15}$$

We notice that all the *explicit* λ-dependence is in the prefactor $\frac{4}{\sqrt{1-\beta'}}$.

Changing the order of integration, we first evaluate the s-integral. After some algebra, we arrive at

$$\mathcal{I}(\eta_{\mathrm{s},y}(\lambda),\beta_0,\lambda) = \frac{2\pi}{\sqrt{1-\beta'}}\int_0^{+\infty}\frac{\mathrm{d}v}{v^2+2\eta_{\mathrm{s},y}v+1}\frac{1}{\sqrt{1+\dfrac{2\alpha'\eta_{\mathrm{s},y}v}{v^2+2\eta_{\mathrm{s},y}v+1}}}, \tag{F.16}$$

where we have used

$$\int_0^{\frac{\pi}{2}}\frac{\mathrm{d}s}{A+B\cos^2 s} = \frac{\pi}{2}\frac{1}{\sqrt{A}}\frac{1}{\sqrt{A+B}}. \tag{F.17}$$

We notice that the term $\left(1+\frac{2\alpha'\eta_{\mathrm{s},y}v}{v^2+2\eta_{\mathrm{s},y}v+1}\right)^{-\frac{1}{2}}$ contains all the non-trivial geometric dependence: Setting $\beta_0=0$ ($\beta'=1-\sqrt{\lambda}$ and $\alpha'=0$) gives

$$\mathcal{I}(\eta_{\mathrm{s},y}(\lambda),\beta_0=0,\lambda)=\frac{2\pi}{\sqrt[4]{\lambda}}\int_0^{+\infty}\frac{\mathrm{d}v}{v^2+2\eta_{\mathrm{s},y}v+1} \tag{F.18}$$

which is the familiar integral corresponding to the stiffness of a spherical shell.

Realizing

$$\frac{\mathrm{d}}{\mathrm{d}v}\arctan\left(\frac{v+\eta_{\mathrm{s},y}}{\sqrt{1-\eta_{\mathrm{s},y}^2}}\right)=\sqrt{1-\eta_{\mathrm{s},y}^2}\frac{1}{v^2+2\eta_{\mathrm{s},y}v+1}, \tag{F.19}$$

we make the change of variables

$$t=\arctan\left(\frac{v+\eta_{\mathrm{s},y}}{\sqrt{1-\eta_{\mathrm{s},y}^2}}\right). \tag{F.20}$$

As a consequence, we can rewrite the term just mentioned, which is related to geometric anisotropy, in terms of t:

$$\begin{aligned}\frac{v}{v^2+2\eta_{\mathrm{s},y}v+1}&=\frac{\sqrt{1-\eta_{\mathrm{s},y}^2}\tan t-\eta_{\mathrm{s},y}}{\sqrt{1-\eta_{\mathrm{s},y}^2}}\left(\frac{\mathrm{d}v}{\mathrm{d}t}(t)\right)^{-1}=\frac{\sqrt{1-\eta_{\mathrm{s},y}^2}\tan t-\eta_{\mathrm{s},y}}{(1-\eta_{\mathrm{s},y}^2)\sec^2 t}\\&=-\frac{1}{2(1-\eta_{\mathrm{s},y}^2)}\left(-\sqrt{1-\eta_{\mathrm{s},y}^2}\sin 2t+\eta_{\mathrm{s},y}\cos 2t+\eta_{\mathrm{s},y}\right)\\&=-\frac{1}{2(1-\eta_{\mathrm{s},y}^2)}\left[\cos\left(2t+\arccos\eta_{\mathrm{s},y}\right)+\eta_{\mathrm{s},y}\right].\end{aligned} \tag{F.21}$$

It follows that in terms of the new integration variable,

$$\begin{aligned}\mathcal{I}(\eta_{\mathrm{s},y}(\lambda),\beta_0,\lambda) &= \frac{2\pi}{\sqrt{1-\beta'}}\frac{1}{\sqrt{1-\eta_{\mathrm{s},y}^2}}\times \\ &\quad\times\int_{\arcsin\eta_{\mathrm{s},y}}^{\frac{\pi}{2}}\frac{\mathrm{d}t}{\sqrt{1-\alpha'\dfrac{\eta_{\mathrm{s},y}}{1-\eta_{\mathrm{s},y}^2}\left[\cos\left(2t+\arccos\eta_{\mathrm{s},y}\right)+\eta_{\mathrm{s},y}\right]}} \\ &= \frac{\pi}{\sqrt{1-\beta'}}\frac{1}{\sqrt{1-\eta_{\mathrm{s},y}^2}}\times \\ &\quad\times\int_{\pi-\arccos\eta_{\mathrm{s},y}}^{\pi+\arccos\eta_{\mathrm{s},y}}\frac{\mathrm{d}\theta}{\sqrt{1-\alpha'\dfrac{\eta_{\mathrm{s},y}^2}{1-\eta_{\mathrm{s},y}^2}-\alpha'\dfrac{\eta_{\mathrm{s},y}}{1-\eta_{\mathrm{s},y}^2}\cos\theta}},\end{aligned} \tag{F.22}$$

where we used the following identities:

$$\arctan\left(\frac{\eta_{\mathrm{s},y}}{\sqrt{1-\eta_{\mathrm{s},y}^2}}\right)=\arcsin\eta_{\mathrm{s},y}\quad\text{and}\quad\arccos\eta_{\mathrm{s},y}+\arcsin\eta_{\mathrm{s},y}=\frac{\pi}{2}, \tag{F.23}$$

and we also changed the integration variable from t to $\theta = 2t+\arccos\eta_{\mathrm{s},y}$. Performing another change of variables $\phi = \theta - \pi$, we can rewrite $\mathcal{I}(\eta_{\mathrm{s},y}(\lambda),\beta_0,\lambda)$ as follows: Factoring out the term $\sqrt{1-\alpha'\frac{\eta_{\mathrm{s},y}^2}{1-\eta_{\mathrm{s},y}^2}}$ from the denominator of the integrand,

$$\mathcal{I}(\eta_{\mathrm{s},y}(\lambda),\beta_0,\lambda)=\frac{2\pi}{\sqrt{1-\beta'}}\frac{1}{\sqrt{1-\alpha\eta_{\mathrm{s},y}^2}}\int_0^{\arccos\eta_{\mathrm{s},y}}\frac{\mathrm{d}\phi}{\sqrt{1+\dfrac{\alpha'\eta_{\mathrm{s},y}}{1-\alpha\eta_{\mathrm{s},y}^2}\cos\phi}}; \tag{F.24}$$

recall $\alpha = \alpha' + 1$. Using the identity

$$\int_0^{\vartheta}\frac{\mathrm{d}\phi}{\sqrt{1+A\cos\phi}}=\frac{2}{\sqrt{1+A}}\mathrm{F}\left(\frac{1}{2}\vartheta\,\middle|\,\frac{2A}{1+A}\right), \tag{F.25}$$

we finally get, after some rewriting, Eq. (3.33).

APPENDIX G

SIMULATION METHODS: SHELL INDENTATION (COMSOL)

Cody Rasmussen set up the initial indentation models for isotropic shells, figured out how to check the material principal directions and, more importantly, generously passed to me all his knowledge about using COMSOL without holding back.

In this appendix, we provide implementation details of finite element simulations of the indentation studies (**3.3.4**), which were performed using the software COMSOL Multiphysics. We used the Stationary solver with the Shell module to simulate the equilibrium configurations of orthotropic thin shells under combined pressure and point loads. Geometric nonlinearity was enabled to ensure that the influence of the pressure-induced prestress was correctly accounted for in the indentation study.

G.1 Orthotropic Materials

COMSOL allows for the definition of arbitrary anisotropic elastic materials using the Material module. It is known that a three-dimensional orthotropic material has *nine* independent elastic constants; these include three Young's moduli (E_1, E_2 and E_3), three Poisson's ratios (υ_{12}, υ_{13} and υ_{23}) and three shear moduli (G_{12}, G_{13} and G_{23}) [50]. The nine parameters have to satisfy constraints that stem from positive definiteness of the corresponding stiffness tensor. This makes it challenging to choose sets of these parameters which can guarantee stable simulations. We therefore followed the presentation by Li and Barbič for simulating orthotropic materials [90]. The essence of their approach is summarized below.

Li and Barbič consider a subclass of orthotropic materials which can be characterized with only *four* independent parameters: $\Big\{E_1, \lambda \equiv \lambda_{12} \coloneqq \frac{E_1}{E_2}, \lambda_{13} \coloneqq$

$\frac{E_1}{E_3}, \upsilon_{\text{eff}}\Big\}$. The last parameter υ_{eff} is related to the three Poisson's ratios in the following way:

$$\upsilon_{\text{eff}} \coloneqq \sqrt{\upsilon_{12}\upsilon_{21}} \overset{!}{=} \sqrt{\upsilon_{13}\upsilon_{31}} \overset{!}{=} \sqrt{\upsilon_{23}\upsilon_{32}}, \tag{G.1}$$

which implies (using the facts $\frac{\upsilon_{ij}}{E_i} = \frac{\upsilon_{ji}}{E_j}$) that

$$\upsilon_{ij} = \upsilon_{\text{eff}}\sqrt{\frac{E_i}{E_j}} \quad (i, j \in \{1, 2, 3\}). \tag{G.2}$$

The three shear moduli are given by the corresponding Huber form:

$$G_{ij} \overset{!}{=} \frac{\sqrt{E_i E_j}}{2(1 + \upsilon_{\text{eff}})}. \tag{G.3}$$

The positive definiteness constraints require that $E_1, \lambda, \lambda_{13} \in \mathbb{R}_{>0}$, and $\upsilon_{\text{eff}} \in (-1, \frac{1}{2}]$.[1]

In our simulations, we fixed the value of E_1 and υ_{eff} to be 70 GPa and 0.3, respectively. We also fixed the value of λ_{13} after having verified that transverse shear deformations were indeed negligible in our studies. We chose $\lambda_{13} \overset{!}{=} 2$. Therefore, in our simulations, there was really only *one* free parameter that needed tuning to vary the degree of a thin shell's material anisotropy, namely λ.

G.2 Shells with Material Orthotropy and Boundary Conditions

The `3D Component` feature was first used to generate spheroidal and cylindrical surfaces. We then used the `Shell` module to turn these surfaces into actual shells.

[1]Note that the isotropic Poisson's ratio υ_{iso} has the same range as υ_{eff}: $\upsilon_{\text{iso}} \in (-1, \frac{1}{2}]$. This is indeed the key motivation for introducing υ_{eff}.

G.2.1 Spheroidal Shells

A spheroid is an ellipsoid of revolution. To parametrize a spheroid, $\frac{x^2}{a^2}+\frac{y^2+z^2}{b^2}=1$, two parameters, a and b, are needed. In our simulations, we fixed $b \stackrel{!}{=} 1$ m (so that $R_y \stackrel{!}{=} 1$ m) and set $a \stackrel{!}{=} \frac{b}{\sqrt{1-\beta_0}}$. We varied the asphericity of a spheroid by changing β_0 ($\beta_0 \in (-1, 1]$). The thickness of the spheroidal shell (denoted by t) was also fixed during each simulation. Since we were simulating thin shells, it is required that $\frac{b}{t} \gtrsim 50$. We used $t \stackrel{!}{=} 1$ mm in our simulations.

For best results, we aimed for the mesh in the vicinity of the indentation point to be as fine as possible, relative to the characteristic length scales for thin-shell deflections which are the geometric means $\sqrt{R_1 t}$ and $\sqrt{R_2 t}$; however, setting the same fine mesh size for the entire shell was computationally impractical and also unnecessary: the main contribution of the rest of the shell away from the indentation region is to provide the geometry-determined prestress in response to the internal pressure, which varies on much longer length scales of order R_1 and R_2. Therefore, we assembled the shell surface out of separate regions with different mesh fineness requirements to balance physics performance with computational efficiency, as described below.

We used both the `Physics-controlled mesh` and the `User-controlled mesh` to build our spheroidal shells ($\beta_0 \neq 1$). Each shell surface S is composed of three disjoint regions: $S = S_{\text{top}} \sqcup S_{\text{bot}} \sqcup S_{\text{rest}}$. Take the ellipsoid in Fig. 3.1 (c) as an example. Among the three, the second region S_{bot} is centered at O. Its projection onto the tangent plane at O is an elliptical disk $\mathcal{E}$ whose semi-major (semi-minor) axis is given by $\max\left\{3\sqrt{R_x t}, 3\sqrt{R_y t}\right\}$ ($\min\left\{3\sqrt{R_x t}, 3\sqrt{R_y t}\right\}$). The first region S_{top} is centered at the top of the ellipsoid but otherwise identical to S_{bot}, and S_{rest} represents the rest of the shell surface. The first two regions can be built by obtaining the `Intersection`

of S and a *solid* elliptical cylinder with cross-section $\mathcal{E}$ (the cylinder can be built with the built-in `Extrude` function), and the third region by taking the `Difference`. For S_{top} and S_{bot}, we used the `User-controlled mesh` and set the mesh size *exactly* to $3t = 3$ mm (we enforced `Maximum element size` and `Minimum element size` to be equal). For S_{rest}, the physics-controlled `Extremely fine` mesh size was used.

Material orthotropy was implemented using the `Material` module. Orientations of material orthotropy were conveniently set, by default in `COMSOL`, to coincide with the shell's `Global coordinate system`, which can be found under Shell/Linear Elastic Material/Shell Local System/Coordinate System Selection/Coordinate system. The default orientation recreated the desired alignment of the material directions with the symmetry directions of spheroidal shells for equatorial indentations (Fig. 1). For simulations on indentation response at the poles of an orthotropic sphere (**Appendix D**), we instead used the `Boundary System` for orienting the orthotropy directions, which conveniently put the two poles at the sphere's top and bottom.

We used the boundary condition `Rigid Motion Suppression` for `All boundaries`. We also used the boundary condition `Symmetry` for `All edges` except the boundary of S_{top} and S_{bot}.

To simulate an internal pressure, a *negative* `Face Load` was applied. For the zero-pressure simulations, the magnitude of the `Face Load` was set to zero. The indentation itself was implemented using two instances of `Point Load` to ensure force balance: one `Point Load` with a *negative* magnitude was applied at the top of the shell, $(0, 0, b)$, and a *positive* one at the bottom, $(0, 0, -b)$. The absolute magnitude of the two loads was identical (this is essential for `Rigid Motion Suppression` to be used properly) and small, such that the resulting normal displacement, `shell.w`,

was much less than the shell thickness t. In our simulations, the force magnitude used was 1 N. The ratio of the force magnitude to the resulting normal displacement provided the desired indentation stiffness measurement in our simulations.

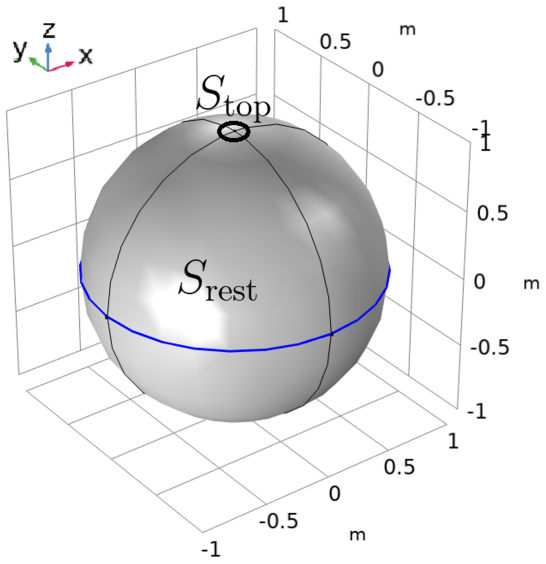

FIGURE G.1. `COMSOL` setup for a sphere ($\beta_0 = 0$). The different mesh regions are indicated.

G.2.2 Cylindrical Shells

The radius of the cylindrical shells (denoted by R) was fixed to be 1 m. As for spheroidal shells, it is required that $\frac{R}{t} \gtrsim 50$, where t again denotes the shell thickness. As before, we used 1 mm for t. We also used the same loading conditions (`Face Load` and `Point Load`); however, depending on the magnitude of the internal pressure, different geometries with associated boundary conditions were employed.

G.2.2.1 Low pressures. Under this circumstance, which includes the zero-pressure case, indentation response of long cylinders is not localized. In our simulations, this corresponds to the pressure range $\eta_{s,y} \lesssim 10^{-4}$. For this pressure

range, we run our simulations with real cylindrical shells for which β_0 is exactly equal to one. Because `COMSOL` is not able to simulate infinite cylinders, we set the length of our shells to be $10R\sqrt{\frac{R}{t}}$. The combination $R\sqrt{\frac{R}{t}}$ is the characteristic deformation length scale for indenting a cylinder at zero pressure [3]: The indentation response becomes negligible at distances greater than this length scale away from the point load. For this geometry, `Rigid Motion Suppression` was again imposed for `All boundaries`, and `Symmetry` for `All edges`. We only used the `User-controlled mesh` to build our cylindrical shells; the mesh size belongs to the range $(10t, 1000t)$.

G.2.2.2 High pressures. By "high pressure" we mean that the internal pressure that a cylinder is subjected to is high enough, so that the resulting indentation response starts to become localized [5], and it is accurate to use the double Fourier transform. In our simulations, this happens when the scaled pressure is of the order of 10^{-2} ($\eta_{s,y} \sim 10^{-2}$). However, we found that for perfectly cylindrical shells, the prestress components computed by `COMSOL` did not match the well-established results for cylindrical pressure vessels [10]. While we could not pinpoint the source of this discrepancy, we observed that the discrepancy was eliminated upon using highly elongated spheroids with $\beta_0 = 0.9999$, which have approximately the same prestress profile and the same local geometry as cylinders at the equator. Therefore, for $\eta_{s,y} \gtrsim 10^{-2}$, we run our simulations using elongated spheroids with $\beta_0 = 0.9999$. The `Rigid Motion Suppression` was again imposed for `All boundaries`. Unlike before, `Symmetry` was only imposed for the edges with respect to which the top and bottom of a spheroid are symmetric (e.g., the blue curves in Fig. G.1); imposing `Symmetry` for `All edges` created issues related to a known "bursting" instability of nearly cylindrical shells at very high pressures [91].

We built the surface of these elongated spheroidal shells using the same three regions as before (see **Appendix G.2.1**). For S_{top} and S_{bot}, the `User-controlled mesh` was used with mesh size belonging to the range $(3t, 30t)$, and the physics-controlled `Extremely fine` mesh size was used for S_{rest}.

APPENDIX H

SIMULATION METHODS: BUCKLING OF ORTHOTROPIC SPHERES

Professor Roman Vetter performed the `C++` simulations on shell buckling and contributed this appendix.

The buckling pressure of orthotropic spherical shells, Fig. 3.5, was determined with finite element simulations. As the implementation in C++ is based on previous work [54, 92, 93, 94], we summarize only the main aspects here.

Denote by $\Omega \subset \mathbb{R}^3$ the middle surface of the thin shell with thickness t. We now distinguish between the stress-free reference configuration denoted by barred symbols, and the deformed configuration, denoted by bare symbols. Thus, $\overline{\Omega} \subset \mathbb{R}^3$ is the middle surface of the unstrained shell (a sphere in the case considered here). We describe the shell in a total Lagrangian formulation, with $\overline{\mathbf{x}}(x^1, x^2)$ and $\mathbf{x}(x^1, x^2)$ curvilinear parameterizations of $\overline{\Omega}$ and Ω, respectively. The tangent spaces of $\overline{\Omega}$ and Ω are then spanned by

$$\overline{\mathbf{a}}_\alpha(x^1, x^2) = \overline{\mathbf{x}}_{,\alpha} = \frac{\partial \overline{\mathbf{x}}}{\partial x^\alpha}, \qquad \mathbf{a}_\alpha(x^1, x^2) = \mathbf{x}_{,\alpha} = \frac{\partial \mathbf{x}}{\partial x^\alpha}, \tag{H.1}$$

and by virtue of the Kirchhoff assumption, the shell directors are given by the unit surface normals

$$\overline{\mathbf{a}}_3 = \frac{\overline{\mathbf{a}}_1 \times \overline{\mathbf{a}}_2}{\|\overline{\mathbf{a}}_1 \times \overline{\mathbf{a}}_2\|}, \qquad \mathbf{a}_3 = \frac{\mathbf{a}_1 \times \mathbf{a}_2}{\|\mathbf{a}_1 \times \mathbf{a}_2\|}. \tag{H.2}$$

To define the membrane and bending strains, we require the covariant components of the metric tensor,

$$\overline{a}_{\alpha\beta} = \overline{\mathbf{a}}_\alpha \cdot \overline{\mathbf{a}}_\beta, \qquad a_{\alpha\beta} = \mathbf{a}_\alpha \cdot \mathbf{a}_\beta, \tag{H.3}$$

and those of the shape tensor,

$$\overline{b}_{\alpha\beta} = \overline{\mathbf{a}}_3 \cdot \overline{\mathbf{a}}_{\alpha,\beta}, \qquad b_{\alpha\beta} = \mathbf{a}_3 \cdot \mathbf{a}_{\alpha,\beta}. \tag{H.4}$$

Since the thin shell is in a state of locally plane stress, the strain tensors for stretching and bending with respect to the curvilinear coordinates can be expressed in Voigt notation as

$$\boldsymbol{\alpha} = \begin{pmatrix} \alpha_{11} \\ \alpha_{22} \\ 2\alpha_{12} \end{pmatrix} = \frac{1}{2} \begin{pmatrix} a_{11} - \overline{a}_{11} \\ a_{22} - \overline{a}_{22} \\ 2(a_{12} - \overline{a}_{12}) \end{pmatrix}, \qquad \boldsymbol{\beta} = \begin{pmatrix} \beta_{11} \\ \beta_{22} \\ 2\beta_{12} \end{pmatrix} = \begin{pmatrix} \overline{b}_{11} - b_{11} \\ \overline{b}_{22} - b_{22} \\ 2(\overline{b}_{12} - b_{12}) \end{pmatrix}. \tag{H.5}$$

We now transform these into an orthonormal basis $\{\mathbf{e}_1, \mathbf{e}_2\}$ of the tangent space, with respect to which the material orthotropy is expressed, using a transformation matrix $\mathbf{T}$ [94]:

$$\boldsymbol{\varepsilon} = \mathbf{T}\boldsymbol{\alpha}, \qquad \boldsymbol{\kappa} = \mathbf{T}\boldsymbol{\beta} \tag{H.6}$$

with

$$\mathbf{T} = \begin{pmatrix} t_{11}^2 & t_{21}^2 & t_{11}t_{21} \\ t_{12}^2 & t_{22}^2 & t_{12}t_{22} \\ 2t_{11}t_{12} & 2t_{21}t_{22} & t_{11}t_{22} + t_{12}t_{21} \end{pmatrix}, \qquad t_{\alpha\beta} = \overline{\mathbf{a}}^{\alpha} \cdot \mathbf{e}_{\beta}. \tag{H.7}$$

For a spherical shell, we define the material coordinate system aligned with the polar and azimuthal directions:

$$\mathbf{e}_1 = \frac{\overline{\mathbf{x}}}{\|\overline{\mathbf{x}}\|} \times \mathbf{e}_2, \qquad \mathbf{e}_2 = \frac{\hat{\mathbf{z}} \times \overline{\mathbf{x}}}{\|\hat{\mathbf{z}} \times \overline{\mathbf{x}}\|} \tag{H.8}$$

where $\hat{\mathbf{z}} = (0, 0, 1)^\top$.

With these definitions, the potential energy of a pressurized, orthotropic thin shell can be expressed as [94]

$$U = \int_{\overline{\Omega}} \frac{1}{2} \left(t \boldsymbol{\varepsilon}^\top \mathbf{C} \boldsymbol{\varepsilon} + \frac{t^3}{12} \boldsymbol{\kappa}^\top \mathbf{C} \boldsymbol{\kappa} \right) - p \, \mathbf{a}_3 \cdot (\mathbf{x} - \overline{\mathbf{x}}) \, d\overline{\Omega} \tag{H.9}$$

where p is the internal-to-external pressure difference, $d\overline{\Omega} = \|\overline{\mathbf{a}}_1 \times \overline{\mathbf{a}}_2\| \; dx^1 dx^2$ the reference area element, and

$$\mathbf{C} = \begin{pmatrix} E_1/(1 - \upsilon_{12}\upsilon_{21}) & \upsilon_{21}E_1/(1 - \upsilon_{12}\upsilon_{21}) & 0 \\ \upsilon_{12}E_2/(1 - \upsilon_{12}\upsilon_{21}) & E_2/(1 - \upsilon_{12}\upsilon_{21}) & 0 \\ 0 & 0 & G_{12} \end{pmatrix} \tag{H.10}$$

the elastic tensor for orthotropic plane stress. To minimize U numerically, we discretized the spherical shell into a triangulated mesh that was built by recursively subdividing a regular icosahedron five times, resulting in a so-called "icosphere" consisting of 20480 triangles and 10242 vertices. 10% of the average edge length was added to each vertex position on the sphere as random noise to break the mesh symmetry. Using C^1-conforming Loop subdivision surface shape functions [95], the middle surface can then be expressed as linear combinations of the shape functions N_I with the nodal positions x_I as weights:

$$\overline{\mathbf{x}}(x^1, x^2) = \sum_{I=1}^{12} \overline{\mathbf{x}}_I N_I, \qquad \mathbf{x}(x^1, x^2) = \sum_{I=1}^{12} \mathbf{x}_I N_I. \tag{H.11}$$

(Note that for evaluation of the surface on patches with nodes of valence other than six, a recursive procedure is needed [95].) With this finite element discretization, and

using a single Gauss point per triangle, the nodal forces can be assembled as [94]

$$\mathbf{f}_I = -\sum_e \left\{ \left(t\mathbf{M}_I^\top \hat{\mathbf{C}}\boldsymbol{\alpha} + \frac{t^3}{12}\mathbf{B}_I^\top \hat{\mathbf{C}}\boldsymbol{\beta} - pN_I\,\mathbf{a}_3 \right) \frac{\|\overline{\mathbf{a}}_1 \times \overline{\mathbf{a}}_2\|}{2} \right\}_e , \tag{H.12}$$

where the sum runs over all triangles e within the local support of N_I, $\{\cdot\}_e$ denotes evaluation at the barycenter of e,

$$\hat{\mathbf{C}} = \mathbf{T}^\top \mathbf{C}\mathbf{T} \tag{H.13}$$

is the elastic tensor transformed to the local frame, and $\mathbf{M}_I$ and $\mathbf{B}_I$ are membrane and bending matrices, whose transpose are column-wise given by [94]

$$\mathbf{M}_I^\top = \begin{pmatrix} N_{I,1}\mathbf{a}_1 & N_{I,2}\mathbf{a}_2 & N_{I,1}\mathbf{a}_2 + N_{I,2}\mathbf{a}_1 \end{pmatrix} \tag{H.14}$$

$$\mathbf{B}_I^\top = \begin{pmatrix} \mathbf{b}_{11}^I & \mathbf{b}_{22}^I & 2\mathbf{b}_{12}^I \end{pmatrix} \tag{H.15}$$

with

$$\mathbf{b}_{\alpha\beta}^I = \frac{1}{\|\mathbf{a}_1 \times \mathbf{a}_2\|} \left(\mathbf{a}_{\alpha,\beta} - b_{\alpha\beta}\,\mathbf{a}_3\right) \times \left(N_{I,1}\mathbf{a}_2 - N_{I,2}\mathbf{a}_1\right) - N_{I,\alpha\beta}\mathbf{a}_3. \tag{H.16}$$

With the nodal forces, we solved Newton's equations of motion with far-subcritical viscous damping added, using a Newmark predictor-corrector method [94]. To determine the critical pressure, we slowly ramped up the applied pressure p in the simulations until the shell collapsed.

REFERENCES CITED

[1] Huanxin Zhang, Huabin Wang, Jonathan J. Wilksch, Richard A. Strugnell, Michelle L. Gee, and Xi-Qiao Feng. Measurement of the interconnected turgor pressure and envelope elasticity of live bacterial cells. *Soft Matter*, 17: 2042–2049, 2021. doi: 10.1039/D0SM02075C.

[2] Dominic Vella, Amin Ajdari, Ashkan Vaziri, and Arezki Boudaoud. Indentation of Ellipsoidal and Cylindrical Elastic Shells. *Physical Review Letters*, 109 (14gain):144302, 2012. ISSN 0031-9007. doi: 10.1103/PhysRevLett.109.144302.

[3] Pedro J de Pablo, Iwan AT Schaap, Frederick C MacKintosh, and Christoph F Schmidt. Deformation and collapse of microtubules on the nanometer scale. *Physical Review Letters*, 91(9), 2003. doi: 10.1103/PhysRevLett.91.098101.

[4] Yi Deng, Mingzhai Sun, and Joshua W. Shaevitz. Direct Measurement of Cell Wall Stress Stiffening and Turgor Pressure in Live Bacterial Cells. *Physical Review Letters*, 107(15):158101, 2011. doi: 10.1103/PhysRevLett.107.158101.

[5] Wenqian Sun and Jayson Paulose. Indentation responses of pressurized ellipsoidal and cylindrical elastic shells: Insights from shallow-shell theory. *Phys. Rev. E*, 104:025004, Aug 2021. doi: 10.1103/PhysRevE.104.025004. URL `https://link.aps.org/doi/10.1103/PhysRevE.104.025004`.

[6] P. M. Sobota and K. A. Seffen. Bistable polar-orthotropic shallow shells. *Royal Society Open Science*, 6(8), 2019. doi: 10.1098/rsos.190888.

[7] L. Landau and E. Lifshitz. *Theory of Elasticity*. Butterworth-Heinemann, Boston, 3rd ed. edition, 1986.

[8] Frithiof I. Niordson. *Shell Theory*. North-Holland, Amsterdam, 1985.

[9] Eduard Ventsel and Theodor Krauthammer. *Thin Plates and Shells: Theory, Analysis, and Applications*. Taylor & Francis Group, 2001.

[10] James M. Gere and Stephen P. Timoshenko. *Mechanics of Materials*. PWS PUBLISHING COMPANY, Boston, 4th ed. edition, 1997.

[11] Eleni Katifori, Silas Alben, Enrique Cerda, David R. Nelson, and Dumais Jacques. Foldable structures and the natural design of pollen grains. *Proceedings of the National Academy of Sciences*, 107(17), 2010. doi: 10.1073/pnas.0911223107.

[12] Sven Kerstens, Willem F. Decraemer, and Jean-Pierre Verbelen. Cell walls at the plant surface behave mechanically like fiber-reinforced composite materials. *Plant Physiology*, 127(2), 2001. doi: 10.1104/pp.010423.

[13] Tobias I. Baskin. Anisotropic expansion of the plant cell wall. *Annual Review of Cell and Developmental Biology*, 21(1), 2005. doi: 10.1146/annurev.cellbio.20.082503.103053.

[14] Dominic Vella, Amin Ajdari, Ashkan Vaziri, and Arezki Boudaoud. The indentation of pressurized elastic shells: From polymeric capsules to yeast cells. *Journal of The Royal Society Interface*, 9(68), 2012. doi: 10.1098/rsif.2011.0352.

[15] Eric Reissner. Stresses and small displacements of shallow spherical shells. ii. *Journal of Mathematics and Physics*, 25(1-4), 1946.

[16] A. V. Pogorelov. *Bendings of Surfaces and Stability of Shells*. American Mathematical Society, Providence, Rhode Island, 1986.

[17] Jayson Paulose, Gerard A. Vliegenthart, Gerhard Gompper, and David R. Nelson. Fluctuating shells under pressure. *Proceedings of the National Academy of Sciences*, 109(48), 2012. doi: 10.1073/pnas.1212268109.

[18] Shao Wen Yuan. Thin cylindrical shells subjected to concentrated loads. *Quarterly of Applied Mathematics*, 4(1), 1946.

[19] John J. Thwaites and Neil H. Mendelson. Mechanical behaviour of bacterial cell walls. *Advances in microbial physiology*, 32, 1991. doi: 10.1016/S0065-2911(08)60008-9.

[20] B. Audoly and Y. Pomeau. *Elasticity and geometry: from hair curls to the nonlinear response of shells*. Oxford University Press, 2010.

[21] I L Ivanovska, P J de Pablo, B Ibarra, G Sgalari, F C MacKintosh, J L Carrascosa, C F Schmidt, and G J L Wuite. Bacteriophage capsids: tough nanoshells with complex elastic properties. *Proceedings of the National Academy of Sciences of the United States of America*, 101(20):7600–5, may 2004. ISSN 0027-8424. doi: 10.1073/pnas.0308198101.

[22] Somnath Chattopadhyay. *Pressure vessels: design and practice*. CRC press, 2004.

[23] Yang-Tse Cheng and Che-Min Cheng. Scaling, dimensional analysis, and indentation measurements. *Materials Science and Engineering: R: Reports*, 44 (4-5):91–149, 2004.

[24] Ashkan Vaziri and L Mahadevan. Localized and extended deformations of elastic shells. *Proceedings of the National Academy of Sciences*, 105(23): 7913–7918, jun 2008. ISSN 0027-8424. doi: 10.1073/pnas.0707364105.

[25] A. Lazarus, H. C. B. Florijn, and P. M. Reis. Geometry-Induced Rigidity in Nonspherical Pressurized Elastic Shells. *Physical Review Letters*, 109(14): 144301, 2012. doi: 10.1103/PhysRevLett.109.144301.

[26] Vernita D Gordon, Xi Chen, John W Hutchinson, Andreas R Bausch, Manuel Marquez, and David A Weitz. Self-assembled polymer membrane capsules inflated by osmotic pressure. *Journal of the American Chemical Society*, 126 (43):14117–14122, 2004.

[27] C. I. Zoldesi, I. L. Ivanovska, C. Quilliet, G. J. L. Wuite, and A. Imhof. Elastic properties of hollow colloidal particles. *Phys. Rev. E*, 78:051401, Nov 2008. doi: 10.1103/PhysRevE.78.051401.

[28] M Arnoldi, M Fritz, E Bäuerlein, M Radmacher, E Sackmann, and a Boulbitch. Bacterial turgor pressure can be measured by atomic force microscopy. *Physical review. E, Statistical physics, plasmas, fluids, and related interdisciplinary topics*, 62(1 Pt B):1034–44, 2000. ISSN 1063-651X.

[29] Alexander E Smith, Zhibing Zhang, Colin R Thomas, Kennith E Moxham, and Anton PJ Middelberg. The mechanical properties of saccharomyces cerevisiae. *Proceedings of the National Academy of Sciences*, 97(18):9871–9874, 2000.

[30] Iwan A. T. Schaap, Carolina Carrasco, Pedro J. de Pablo, Frederick C. MacKintosh, and Christoph F. Schmidt. Elastic response, buckling, and instability of microtubules under radial indentation. *Biophysical journal*, 91(4), 2006. doi: 10.1529/biophysj.105.077826.

[31] A. M. A. van der Heijden. *W. T. Koiter's Elastic Stability of Solids and Structures*. Cambridge University Press, Cambridge, UK, 2009.

[32] Ariel Amir, Farinaz Babaeipour, Dustin B. McIntosh, David R. Nelson, and Suckjoon Jun. Bending forces plastically deform growing bacterial cell walls. *Proceedings of the National Academy of Sciences of the United States of America*, 111(16), 2014. doi: 10.1073/pnas.1317497111.

[33] Felix Wong, Lars D. Renner, Gizem Özbaykal, Jayson Paulose, Douglas B. Weibel, Sven van Teeffelen, and Ariel Amir. Mechanical strain sensing implicated in cell shape recovery in escherichia coli. *Nature Microbiology*, 2 (17115), 2017. doi: 10.1038/nmicrobiol.2017.115.

[34] Alphose Zingoni. Stress analysis of a storage vessel in the form of a complete triaxial ellipsoid: hydrostatic effects. *International Journal of Pressure Vessels and Piping*, 62(3), 1995. doi: 10.1016/0308-0161(94)00020-J.

[35] R. A. Clark and E. Reissner. On stresses and deformations of ellipsoidal shells subject to internal pressure. *Journal of the Mechanics and Physics of Solids*, 6 (1), 1957. doi: 10.1016/0022-5096(57)90048-0.

[36] W. T. Koiter. A spherical shell under point loads at its poles. In D. Drucker, editor, *Progress in Applied Mechanics (The Prager Anniversary Volume)*. Macmillan, New York, 1963.

[37] Robert Zoelly. *Ueber ein Knickungsproblem an der Kugelschale*. PhD thesis, ETH Zurich, 1915.

[38] Petr E. Tovstik and Andrei L. Smirnov. *Asymptotic Methods in the Buckling Theory of Elastic Shells*. World Scientific Publishing Co. Pte. Ltd., Singapore, 2001.

[39] Emmanuel Virot, Tobias Kreilos, Tobias M. Schneider, and Shmuel M. Rubinstein. Stability landscape of shell buckling. *Physical Review Letters*, 119, 2017. doi: 10.1103/PhysRevLett.119.224101.

[40] Joel Marthelot, Francisco López Jiménez, Anna Lee, John W. Hutchinson, and Pedro M. Reis. Buckling of a Pressurized Hemispherical Shell Subjected to a Probing Force. *Journal of Applied Mechanics*, 84(12), October 2017. doi: 10.1115/1.4038063.

[41] Arefeh Abbasi, Dong Yan, and Pedro M. Reis. Probing the buckling of pressurized spherical shells. *Journal of the Mechanics and Physics of Solids*, 155:104545, October 2021. doi: 10.1016/j.jmps.2021.104545.

[42] S. N. Krivoshapko. Research on general and axisymmetric ellipsoidal shells used as domes, pressure vessels, and tanks. *Applied Mechanics Reviews*, 60:336–355, 2007. doi: 10.1115/1.2806278.

[43] Adrian M. Whatmore and Robert H. Reed. Determination of turgor pressure in Bacillus subtilis: A possible role for K+ in turgor regulation. *Microbiology,*, 136 (12):2521–2526, 1990. doi: 10.1099/00221287-136-12-2521.

[44] Jayson Paulose and David R. Nelson. Buckling pathways in spherical shells with soft spots. *Soft Matter*, 9:8227–8245, 2013. doi: 10.1039/c3sm50719j.

[45] Pierre-Gilles De Gennes, Françoise Brochard-Wyart, and David Quéré. *Capillarity and wetting phenomena: drops, bubbles, pearls, waves*. Springer Science & Business Media, 2013.

[46] Michael Gomez, Derek E. Moulton, and Dominic Vella. The shallow shell approach to Pogorelov's problem and the breakdown of 'mirror buckling'. *Proceedings of the Royal Society A: Mathematical, Physical and Engineering Sciences*, 472(2187):20150732, March 2016. doi: 10.1098/rspa.2015.0732.

[47] Lorenz Baumgarten and Jan Kierfeld. Shallow shell theory of the buckling energy barrier: From the Pogorelov state to softening and imperfection sensitivity close to the buckling pressure. *Physical Review E*, 99(2):022803, February 2019. doi: 10.1103/PhysRevE.99.022803.

[48] Guo-Xuan Xu, Pei-Yu Chen, Xiaoning Jiang, and Chih-Chung Huang. Visualization of human skeletal muscle mechanical anisotropy by using dual-direction shear wave imaging. *IEEE Transactions on Biomedical Engineering*, 69(9):2745–2754, Sep. 2022. ISSN 1558-2531. doi: 10.1109/TBME.2022.3152896.

[49] Voichita Bucur. Wood structural anisotropy estimated by acoustic invariants. *IAWA Journal*, 9(1):67 – 74, 1988. doi: https://doi.org/10.1163/22941932-90000471.

[50] S. G. Lekhnitskii. *Theory of Elasticity of an Anisotropic Body*. Mir Publishers, Moscow, USSR, 2nd ed. edition, 1981.

[51] Charles W Wolgemuth, Yuki F Inclan, Julie Quan, Sulav Mukherjee, George Oster, and M A R Koehl. How to make a spiral bacterium. *Physical Biology*, 2 (3):189, Sep. 2005. doi: 10.1088/1478-3975/2/3/006.

[52] Alemdar Bayraktar, Serap Bayraktar, and Emin Hökelekli. Strengthening techniques for masonry domes: A review. *International Journal of Space Structures*, 38(1):30–39, 2023. doi: 10.1177/09560599221126652.

[53] Kenneth P. Buchert. *Buckling of doubly curved orthotropic shells*. University of Missouri, Engineering Experiment Station, 1965.

[54] Gautam Munglani, Falk K. Wittel, Roman Vetter, Filippo Bianchi, and Hans J. Herrmann. Collapse of orthotropic spherical shells. *Physical Review Letters*, 123:58002, 2019. ISSN 0031-9007. doi: 10.1103/PhysRevLett.123.058002.

[55] S.d Guest and S Pellegrino. Analytical models for bistable cylindrical shells. *Proceedings of the Royal Society A: Mathematical, Physical and Engineering Sciences*, 462(2067):839–854, 2006. doi: 10.1098/rspa.2005.1598.

[56] K. A. Seffen. Morphing bistable orthotropic elliptical shallow shells. *Proceedings of the Royal Society A: Mathematical, Physical and Engineering Sciences*, 463(2077), 2007. doi: 10.1098/rspa.2006.1750.

[57] S Vidoli and C Maurini. Tristability of thin orthotropic shells with uniform initial curvature. *Proceedings of the Royal Society A: Mathematical, Physical and Engineering Sciences*, 464(2099):2949–2966, 2008. doi: 10.1098/rspa.2008.0094. URL `https://royalsocietypublishing.org/doi/abs/10.1098/rspa.2008.0094`.

[58] Herbert Becker. General instability of stiffened cylinders. Technical report, New York University, 1958.

[59] Y. Xia, M. I. Friswell, and E. I. Saavedra Flores. Equivalent models of corrugated panels. *International Journal of Solids and Structures*, 49(13): 1453–1462, 2012. ISSN 0020-7683. doi: 10.1016/j.ijsolstr.2012.02.023.

[60] Sven van Teeffelen, Siyuan Wang, Leon Furchtgott, Kerwyn Casey Huang, Ned S Wingreen, Joshua W Shaevitz, and Zemer Gitai. The bacterial actin MreB rotates, and rotation depends on cell-wall assembly. *Proceedings of the National Academy of Sciences of the United States of America*, 108(38):15822–7, 2011. ISSN 1091-6490. doi: 10.1073/pnas.1108999108.

[61] Ethan C Garner, Remi Bernard, Wenqin Wang, Xiaowei Zhuang, David Z Rudner, and Tim Mitchison. Coupled, circumferential motions of the cell wall synthesis machinery and MreB filaments in B. subtilis. *Science (New York, N.Y.)*, 333(6039):222–5, 2011. ISSN 1095-9203. doi: 10.1126/science.1203285.

[62] Julia Domínguez-Escobar, Arnaud Chastanet, Alvaro H Crevenna, Vincent Fromion, Roland Wedlich-Söldner, and Rut Carballido-López. Processive movement of MreB-associated cell wall biosynthetic complexes in bacteria. *Science (New York, N.Y.)*, 333(6039):225–8, 2011. ISSN 1095-9203. doi: 10.1126/science.1203466.

[63] Siyuan Wang, Leon Furchtgott, Kerwyn Casey Huang, and Joshua W. Shaevitz. Helical insertion of peptidoglycan produces chiral ordering of the bacterial cell wall. *Proceedings of the National Academy of Sciences*, 109(10):E595–E604, 2012. doi: 10.1073/pnas.1117132109.

[64] Leslie E. Penzes. Free Vibrations of Thin Orthotropic Oblate Spheroidal Shells. *The Journal of the Acoustical Society of America*, 45(2):500–505, 1969. ISSN 0001-4966. doi: 10.1121/1.1911401.

[65] L. E. Penzes and H. Kraus. Free vibration of an inflated oblate spheroidal shell. *Journal of Sound and Vibration*, 27(4):559–572, 1973. ISSN 0022-460X. doi: 10.1016/S0022-460X(73)80362-1.

[66] P. C. Dumir, M. L. Gandhi, and Y. Nath. Axisymmetric static and dynamic buckling of orthotropic shallow spherical caps with flexible supports. *Acta Mechanica*, 52(1), 1984. doi: 10.1007/BF01175967.

[67] Md. Wahhaj Uddin. Buckling of general spherical shells under external pressure. *International Journal of Mechanical Sciences*, 29(7):469–481, 1987. ISSN 0020-7403. doi: 10.1016/0020-7403(87)90009-9.

[68] A. A. Semenov. Strength and stability of geometrically nonlinear orthotropic shell structures. *Thin-Walled Structures*, 106:428–436, 2016. ISSN 0263-8231. doi: 10.1016/j.tws.2016.05.018.

[69] Herbert Becker. Pressure stability of orthotropic prolate spheroids. *Journal of Ship Research*, 12(03):163–164, 09 1968. ISSN 0022-4502. doi: 10.5957/jsr.1968.12.3.163. URL `https://doi.org/10.5957/jsr.1968.12.3.163`.

[70] S. Timoshenko and S. Woinowsky-Krieger. *Theory of Plates and Shells*. McGraw-Hill Book Company, 1959.

[71] V. Panc. *Theories of Elastic Plates*. Noordhoff International, The Netherlands, 1975.

[72] Dominic Vella, Amin Ajdari, Ashkan Vaziri, and Arezki Boudaoud. Indentation of Ellipsoidal and Cylindrical Elastic Shells. *Physical Review Letters*, 109 (14gain):144302, 2012. ISSN 0031-9007. doi: 10.1103/PhysRevLett.109.144302.

[73] B. M. Lempriere. Poisson's ratio in orthotropic materials. *AIAA Journal*, 6 (11):2226–2227, 1968. doi: 10.2514/3.4974.

[74] M. T. Huber. The theory of crosswise reinforced ferroconcrete slabs and its applications to various important constructional problems involving rectangular slabs. *Bauingenieur*, 4:354, 1923.

[75] Shun Cheng and F. B. He. Theory of orthotropic and composite cylindrical shells, accurate and simple fourth-order governing equations. *J. Appl. Mech.*, 51:736–744, 1984. doi: 10.1115/1.3167718.

[76] Maurizio Paschero and Michael W. Hyer. Axial buckling of an orthotropic circular cylinder: Application to orthogrid concept. *International Journal of Solids and Structures*, 46(10):2151–2171, 2009. ISSN 0020-7683. doi: https://doi.org/10.1016/j.ijsolstr.2008.08.033. Special Issue in Honor of Professor Liviu Librescu.

[77] Jayson Paulose and David R. Nelson. Buckling pathways in spherical shells with soft spots. *Soft Matter*, 9:8227–8245, 2013. doi: 10.1039/c3sm50719j.

[78] M. P. Nemeth. Nondimensional parameters and equations for buckling of anisotropic shallow shells. *Journal of Applied Mechanics*, 61(3), 1994. doi: 10.1115/1.2901511.

[79] C. Y. Wang, C. Q. Ru, and A. Mioduchowski. Orthotropic elastic shell model for buckling of microtubules. *Phys. Rev. E*, 74:052901, Nov 2006. doi: 10.1103/PhysRevE.74.052901. URL `https://link.aps.org/doi/10.1103/PhysRevE.74.052901`.

[80] Manfredo P. do Carmo. *Differential Geometry of Curves and Surfaces*. Prentice-Hall, Inc., Englewood Cliffs, New Jersey, 1st ed. edition, 1976.

[81] Sujit S. Datta, Shin-Hyun Kim, Jayson Paulose, Alireza Abbaspourrad, David R. Nelson, and David A. Weitz. Delayed Buckling and Guided Folding of Inhomogeneous Capsules. *Physical Review Letters*, 109(13):134302, 2012. ISSN 0031-9007. doi: 10.1103/PhysRevLett.109.134302.

[82] C. R. Steele and R. F. Hartung. Symmetric Loading of Orthotropic Shells of Revolution. *Journal of Applied Mechanics*, 32(2):337–345, 06 1965.

[83] Eric Reissner. Symmetric bending of shallow shells of revolution. *Journal of Mathematics and Mechanics*, 7(2), 1958.

[84] Petr E. Tovstik and Andrei L. Smirnov. *Asymptotic Methods in the Buckling Theory of Elastic Shells*. World Scientific Publishing Co. Pte. Ltd., Singapore, 2001.

[85] T. Schneider and A. Schmidt. Dimensional crossover scaling in the layered xy-model and ^{4}He films. *Journal of the Physical Society of Japan*, 61(7), 1992. doi: 10.1143/JPSJ.61.2169.

[86] Aditi Chakrabarti, Thomas C. T. Michaels, Sifan Yin, Eric Sun, and L. Mahadevan. The cusp of an apple. *Nature Physics*, 17(10):1125–1129, 2021. ISSN 1745-2481. doi: 10.1038/s41567-021-01335-8.

[87] Carl M. Bender and Steven A. Orszag. *Advanced mathematical methods for scientists and engineers I: Asymptotic methods and perturbation theory*, volume 1. Springer Science & Business Media, 1999.

[88] Robert Piessens. The hankel transform. In Alexander D. Poularikas, editor, *The Transforms and Applications Handbook: Second Edition*. CRC Press LLC, Boca Raton, Florida, 2nd ed. edition, 2000.

[89] I. S. Gradshteyn and I. M. Ryzhik. *Table of Integrals, Series, and Products*. Academic Press, San Diego, California, 5th ed. edition, 1994.

[90] Yijing Li and Jernej Barbič. Stable orthotropic materials. In Vladlen Koltun and Eftychios Sifakis, editors, *Eurographics/ ACM SIGGRAPH Symposium on Computer Animation*. The Eurographics Association, 2014. doi: 10.2312/sca.20141121.

[91] N. L. Svensson. The bursting pressure of cylindrical and spherical vessels. *Journal of Applied Mechanics*, 25(1), 2021. doi: 10.1115/1.4011694.

[92] Roman Vetter, Norbert Stoop, Thomas Jenni, Falk K. Wittel, and Hans J. Herrmann. Subdivision Shell Elements with Anisotropic Growth. *International Journal for Numerical Methods in Engineering*, 95:791–810, 2013. doi: 10.1002/nme.4536.

[93] Gautam Munglani, Roman Vetter, Falk K. Wittel, and Hans J. Herrmann. Orthotropic rotation-free thin shell elements. *Computational Mechanics*, 56: 785–793, 2015. doi: 10.1007/s00466-015-1202-x.

[94] Roman Vetter. *Growth, Interaction and Packing of Thin Objects*. PhD thesis, ETH Zürich, 2015.

[95] Fehmi Cirak, Michael Ortiz, and Peter Schröder. Subdivision surfaces: a new paradigm for thin-shell finite-element analysis. *International Journal for Numerical Methods in Engineering*, 47:2039–2072, 2000. doi: 10.1002/(SICI)1097-0207(20000430)47:12⟨2039::AID-NME872⟩3.0.CO;2-1.